Politecnico di Milano

SCHOOL OF INDUSTRIAL AND INFORMATION ENGINEERING
Master of Science – Aeronautical Engineering

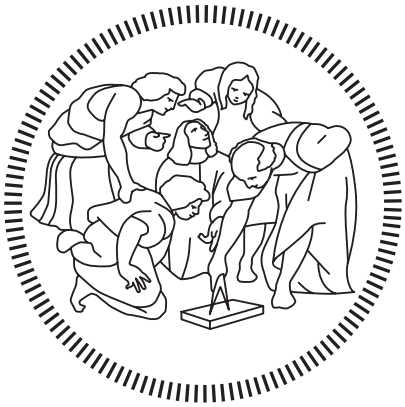

DNS study of turbulent drag reduction via DBD plasma actuators

Supervisor
Prof. Maurizio Quadrio

Candidate
Alessio Malli – 919077

Academic Year 2019 – 2020

Acknowledgements

Questo lavoro di tesi magistrale conclude un percorso di studi durato cinque anni, ricco di gioie e di momenti difficili che mi hanno aiutato a crescere, ma sopratutto di tanti legami personali che mi hanno accompagnato lungo la strada e che ancora mi accompagneranno nel futuro.

In primis, un grazie speciale a Professor Maurizio Quadrio che, nonostante gli impedimenti del momento, mi ha sempre trasmesso fiducia nella buona riuscita del lavoro di tesi. Lui stesso mi ha permesso di capire che a volte è davvero importante sbatterci la testa da soli e che riuscire ad uscire da soli dalle difficoltà ci restituisce nuova consapevolezza, un sentito ringraziamento anche per l'aiuto nella disperata ricerca delle ore di calcolo e per l'opportunita di collaborare con professori di culture diverse dalla nostra.

Ai miei genitori, per il supporto e la fiducia incondizionata, per avermi permesso di prendere le scelte migliori senza mai condizionarle, per il sostegno economico e per l'affetto dimostrato e non sempre ripagato. A mia sorella Sofia, che mi ha sostenuto nel nutrimento con i suoi numerosi esperimenti culinari, che non ho sempre apprezzato a dovere. A Tigro, che mi ha tenuto compagnia durante lo studio e che mi ha sempre ricordato che il riposo e lo svago sono attività tanto importanti quanto lo è il lavoro. A mia nonna, per i pranzi di tutta la settimana e a mio nonno, che ci è sempre stato.

Ad Elisabetta, che mi ha amato e sostenuto, mi ha dato affetto e compagnia quando più ne ho avuto bisogno, che è stata anche compagna di studio e di merende, che mi ha fatto scoprire tante cose belle nel mondo, che mi ha fatto crescere e ha sempre creduto in me.

A Luca, un fratello maggiore che spero farà parte del resto della mia vita insieme a Federica. A Beppe, Lumaca, Dave e Marco, i miei compagni di viaggio del Bst Team, per i consigli tecnici sui problemi più difficili, le parole di conforto e i progetti universitari, che non sarebbero stati ugualmente divertenti e di successo senza la partecipazioni di tutti. Agli altri amici di università: Ame, Edo, Vito, Pippo e Fabio, che mi hanno fatto ridere prima di tanti esami o lezioni. Agli amici di liceo Telo, Marco, Simo, Giulia, Virgi, Lotti, Colo e Gege, che ormai da dieci anni sono parte attiva della mia vita, e ai miei compagni di calcio e di tennis.

Abstract

This work studies by direct numerical simulations (DNS) the skin-friction drag reduction obtained in a turbulent channel flow by steady spanwise forcing realized via standing waves. While the effectiveness of the forcing intended as a boundary condition for the DNS solver has been already proved by several past studies, the aim of the present work is to focus on the (detrimental) effects introduced by the unavoidable presence of a number of discrete Dielectric Barrier Discharge plasma actuators. Hence the DR technique is gradually modified to better describe the field of body forces realistically produced by suitable actuators. The spanwise-discrete nature of the actuators is modeled at increasing level of complexity: discrete spanwise velocity boundary conditions, the Suzen-Huang model for the body force and electro-hydro-dynamics plasma simulations. The effects of discretization are addressed by performing about ten DNS simulations for each of the three cases, where the actuator spacing is varied. The results indicate that drag reduction can still be achieved after spanwise discretization is accounted for.

Keywords: turbulent drag reduction, plasma actuator, spanwise forcing, DNS.

Sommario

Questo lavoro studia, tramite simulazioni numeriche dirette (DNS), la riduzione di resistenza di attrito viscoso ottenuta in un flusso di canale turbolento per mezzo di un forzamento trasversale costante e realizzato mediante onde stazionarie. Mentre l'efficacia del forzamento, inteso come condizioni al contorno per il solutore DNS, è stata già verificata da diversi studi precedenti, lo scopo di questo studio è di concentrarsi sugli effetti (negativi) introdotti dall'inevitabile presenza di un numero discreto di attuatori al plasma con scarica a barriera di dielettrico. Di conseguenza, la tecnica di DR è progressivamente modificata per descrivere meglio il campo di forze di volume realisticamente prodotte dagli appositi attuatori. La natura discreta, in direzione trasversale, degli attuatori è modellata ad un livello di complessità crescente: condizioni al contorno discrete di velocità trasversale, modello di Suzen-Huang per le forze di volume e simulazioni elettro-idro-dinamiche del plasma. Gli effetti della discretizzazione sono analizzati eseguendo circa dieci simulazioni DNS per ognuno dei tre casi, facendo variare la distanza tra gli attuatori. I risultati indicano che è comunque possibile ottenere riduzione di attrito dopo che è stata introdotta la discrezione trasversale.

Parole chiave: riduzione di attrito turbolento, attuatori al plasma, forzamento trasversale, DNS.

Contents

1. Introduction

Due to the increasing pressure for finding environmentally sustainable solutions and because of the oil crisis in the latest part of the last century, many studies investigated a great variety of flow control strategies to achieve turbulent drag reduction. The purpose of turbulent drag reduction techniques is to reduce the skin-friction component of drag, that is responsible of $\approx 55\%$ of the total drag on a nowadays civil aircraft, leading to a potential 15% off the total [33]. Flow control techniques aim to control the turbulence production in the region close to the wall (or to a solid surface in general), where most of the turbulent mechanisms take place, above all the wall cycle [31] [13]. This precise phenomenon can be recognized by some recurrent pattern, such as ejections of low-speed fluids toward the center of the channel or sweeps of high-speed fluid to the near-wall region by the action of the quasi-streamwise vortexes [32]. Since these kind of processes are mostly concentrated in the $y^+ < 100$ region, turbulent DR techniques, as the one considered in the present work, usually are placed in this precise area.

The goal of this study is to investigate the future applicability of one of the most interesting drag reduction strategy in the real world. The present technique, i.e. the stationary spanwise velocity, can be included in the larger family of the streamwise travelling waves (StTW) by considering a null oscillation frequency, in the big class of active flow control. Active flow control request external energy to work, as they generally need MEMS actuators or moving walls to work, but are able to obtain better performances with respect to passive techniques. The StTW strategy was intensively studied in the past years due to its effectiveness; it basically consist of imposing a predetermined sinusoidal streamwise velocity boundary condition on the wall. StTW tuned with the optimal parameters (amplitude, oscillation frequency and streamwise wavenumber) reported a positive reduction on the skin friction coefficient above 50% for large amplitude StTW and a peak of 31% in the net power saving at $Re_\tau = 200$ when an optimal amplitude is chosen as a trade-off between the power spent and the DR performance achieved [11].

Unfortunately, the direct imposition of the sinusoidal boundary condition on a solid wall is not feasible in any real application. This latter problem can be addressed by the introduction of a body forces field that mimic the boundary condition on the wall; the body forces should include only the streamwise component in order not to cause secondary effects on the flow that could be detrimental for DR. The body forces field is produced by specific plasma actuators that are not able to move in time to follow the StTW: the oscillation frequency must be null and the technique fall back in the stationary spanwise velocity strategy. Imposing the null oscillation frequency is not a big issue, the stationary spanwise velocity is able to produce a 45% drag reduction against

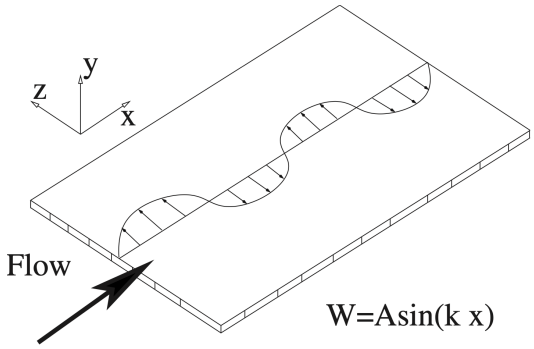

Figure 1.1: Sketch of the stationary spanwise velocity boundary condition. [38]

the 48% of the StTW at the same amplitude [28].

The body force field used to mimic the stationary spanwise velocity is produced by several Dielectric Barrier Discharge (DBD) plasma actuators. This kind of actuator has been investigated in both aeronautical and automotive field [17] thanks to their light weight, flexibility and simplicity. Regarding the aeronautical field, the use of DBD plasma actuators is investigated in [23]. The body forces field is obtained according to different analytical models (Suzen-Huang05 [35], Suzen-Huang07 and Shyy02 [34]) and then inserted in a plane channel flow to model several pairs of aligned plasma actuators placed at different distances. The parametric study pointed out that is possible to achieve 33% DR when the actuators are scaled to the perfect dimension and amplitude, then placed at the best distance. Since the previously cited study addressed the spanwise oscillations, there is no study at the moment that addresses the same specific problem of the present work.

The main focus of the present study is to find the best discretization parameters related to DBD plasma actuators that are able to mimic the previously cited drag reduction technique by the introduction of the forcing according to three different manners. Indeed, plasma actuators can not produce a continuous and purely spanwise body force field. Both models and experiments show that actuators can induce a velocity field only to some extent (about three time the spanwise dimension of the actuator), but they also produce a spurious wall-normal component of about the same order of magnitude of the main spanwise force along with a negligible streamwise component. The main concern is to have a discontinuous induced velocity field that could reduce the drag reduction because of undesirable mechanisms introduced by the discretization, such as vertical ejections of low speed fluid of vice versa.

The project involves to replicate the discretization introduced by the actuators with three different forcing of increasing complexity and reliability. As a first step the spanwise forcing is directly imposed as velocity boundary condition on the wall and the discretization is roughly modelled by the abrupt interruption of the velocity boundary condition above the actuators. The second choice is to use the Suzen-Huang05 model; since the model provide a 2D field of spanwise and wall-normal body forces, the streamwise dimension is obtained by the

modulation of the present field according to the sinusoid. The third sets of simulations are performed by introducing the body forces distribution computed by Professor Hiroyuki Nishida from TUAT University of Tokyo using an Electro-Hydro-Dynamics (EHD) code; the code provide a 3D field produced by a small part of the complete actuator. The present work is thought to be a continuation of the European DRAGY project that was never brought to completion in due time because of the missing computational work. An early PIV experiment from Professor Benard, that was part of this same project, addresses the differences between the 2D body force field using Suzen-Huang model and the PIV measurements of a straight plasma actuator on the same 2D plane [5].

The whole study is conducted by performing Direct Numerical Simulations (DNS) to investigate the different discretization parameters across three different forcing models. The code used is a pseudo-spectral one and it was developed by Professor Quadrio and Professor Luchini in `CPL` compiled language.

2. Turbulence and Flow Control

2.1 Turbulence

Many definitions of Turbulence coexist, each one was given by many of the greatest scientists and physicists from each scientific age, each one is partially correct and partially erroneous at the same time. Some counterexamples always emerge to show the weaknesses of one theory, others come to confirm it.

Turbulence is the last great unresolved problem of classical physics.

Turbulent flows are the rule in the real world and the laminar regime is the exception: the vast majority of engineering applications must deal with turbulent flows, natural flows are often in the turbulent regime to exploit the better mixing properties, large scale phenomena in atmosphere are turbulent, many flows inside human bodies are no exception. Turbulence is everywhere and so, a great effort spent in the last decades to have a better insight in the topic. Researches are still critical because of:

- the complexity of the basic concepts
- the practical difficulties in the experiments
- the high demand in terms of computational costs in numerical simulations

The present work aims to study a particular topic in the main research field in Turbulence, that aims to reduce the drag force component in a turbulent flow. The mechanisms and the structures that the flow develops in such regime are not yet fully understood; most of the phenomena that result to be relevant for the present topic happen in the proximity of a solid wall (or a solid surface in general) and many researches address this region of the flow. Despite the great amount of studies in this branch, many complex mechanism are still unclear and of huge interest because of the great variety of application that they involve.

The main feature of turbulence is the presence of structures of different lengthscale interacting with each other. From a physical point of view, the interaction between different lengthscale is reflected on the vortex dynamics; mathematically, it is reflected on the presence of the non-linear advection term in the equations.

Turbulence can be described by a set of PDEs (Incompressible[1] Navier-Stokes equations) that are not guaranteed to have a closed-form solution and

[1] Mach number related to turbulent fluctuations is usually very small, indeed turbulent fluctuations are more than a order of magnitude smaller than characteristic velocity of the flow.

lead us to introduce turbulence models in the struggle to keep up with computational costs. In the developing of the turbulence models some fundamentals problems arise, first of all: RANS equations are not closed and so one introduce some parameters that need to be tuned experimentally and are not universal at all. One basically ends up with a work that is not completely reliable that requires a lot of effort to adjust the parameters (RANS and LES) or with very reliable results that required an huge amount of resources and time.

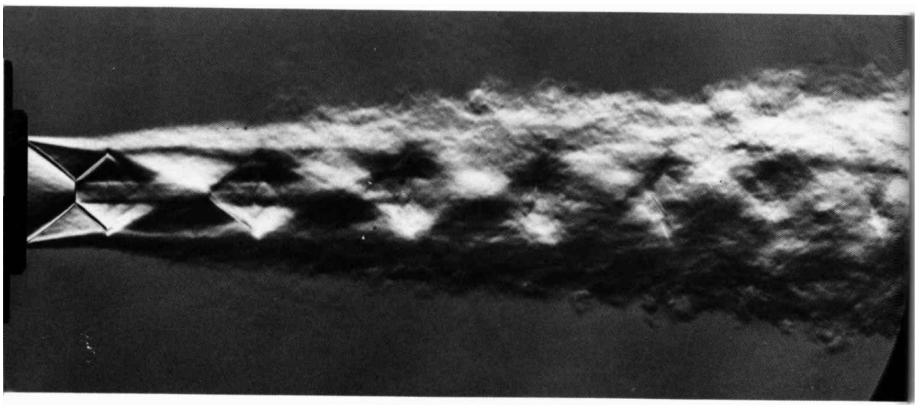

Figure 2.1: Slightly over-expanded supersonic jet becoming turbulent at $M = 1.8$. Diamond shaped pattern is recognizable also after transition. [37]

The only numerical simulations that can deal with this kind of problem are direct numerical simulations (DNS). The DNS approach does not include any turbulence model and faithfully resolve equations in a direct manner. But, dealing with DNS is difficult in term of computational costs: nowadays it is possible to deal only with the simplest geometries one can think of. Increasing the Reynolds number leads to a smaller characteristic length, the size of computational cell must be in the order of that characteristic length[2] of the problem. Hence, the computational cost of the DNS scales with Re raised to the 3rd power ($\eta \sim Re^{-\frac{3}{4}}$; 3D problem with time $\sim Re^{-\frac{3}{4}\cdot 3} Re^{-\frac{3}{4}} \approx Re^{-3}$); simulations at high Re number are still prohibitively expensive also for supercomputers[3] available nowadays.

Here is why it is not possible to simulate complex geometries and DNS are confined to remain academic research tool in the next future, as they are in the present work.

[2]This length η, named after A.N.Kolmogorov [16], represents the typical length scale of the smallest scales of motion. It can be retrieved by a dimensional analysis on the energy cascade concept by Richardson. [30]

[3]To have an idea of the dimension of the problem, here it is a small but effective example: in [18], a plane channel flow simulation at $Re_\tau = 5200$ (corresponding to $Re_b \approx 1.25 \cdot 10^5$) is performed. The LM5200 simulation is carried out on supercomputer Mira; resulting in a 20 million core hours for each flowthrough and a duration for the entire LM5200 DNS simulation of about nine months [19].

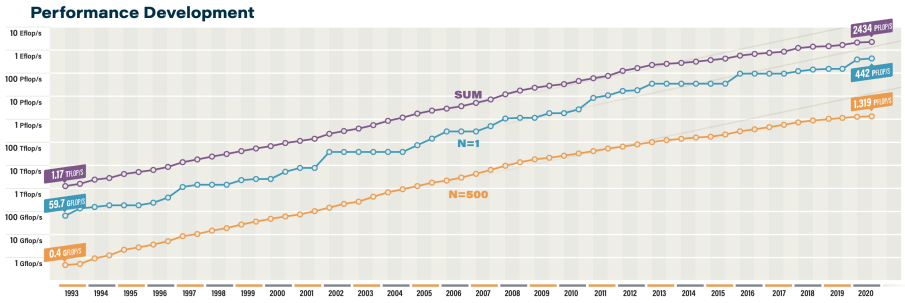

Figure 2.2: Top 500 supercomputers present in the world at November 2020. Prediction by Moore's Law. Data from [1].

2.1.1 Basic concepts in Turbulence

First of all, turbulence is a property of the flow and not of the fluid; it can be useful in some applications to use turbulent viscosity as a property of the fluid but, from a conceptual point of view, this is intrinsically erroneous.

Osborn Reynolds in 1883 made the first attempt to define turbulence and to distinguish between the turbulent regime and the laminar regime. In [29], Reynolds's idea was to identify some properties of the flow that favour the creation of eddies. Eddies are not strictly related with turbulence, but O.Reynolds successfully identified the non-dimensional parameter, later identified as the Reynolds number, that distinguishes the two regimes:

$$Re = \frac{UL}{\nu} \tag{2.1}$$

where U is the characteristic velocity[4] of the flow, L is the characteristic length and ν is the cinematic viscosity of the fluid.

Below a certain value of the Reynolds number the flow is laminar, it shows a predictable behaviour and, for certain simplified geometries, the analytical solution is known. Increasing Re, the flow start to develop some features that are typical of turbulent regime: the flow is not yet completely turbulent and it is in transition to the turbulent regime. The transition from laminar to turbulent has many analogies with the transition from a deterministic system to a chaotic system; one example can be the logistic map based on parameter r: if r is greater than a certain value r_c the system becomes chaotic, but for some $r > r_c$ the system is deterministic again. Taylor-Couette flow shows a similar behaviour: at a certain Re the flow becomes fully turbulent and really chaotic, but increasing Re one can find some intervals in which the flow shows a different kind of turbulence, characterized by ordered vortexes.

Two different approach can be used to identify the particular nature of the instability that brings the flow to the turbulent regime:

- modal stability: address long-term behavior of the perturbations and it is based on the $v - \eta$ formulation.

[4] U and L can be defined in various ways according to the specific problem or context.

- non-modal stability: address short-term behavior of the perturbations and it is based on the analysis of the variation of kinetic energy associated to an initial perturbation.

Modal analysis can be very precise in situations that does not develop a short-term instability; at the same time it is erroneous in situations that develop a short-term instability that drive the flow to a different condition before the long-term instability is developed.

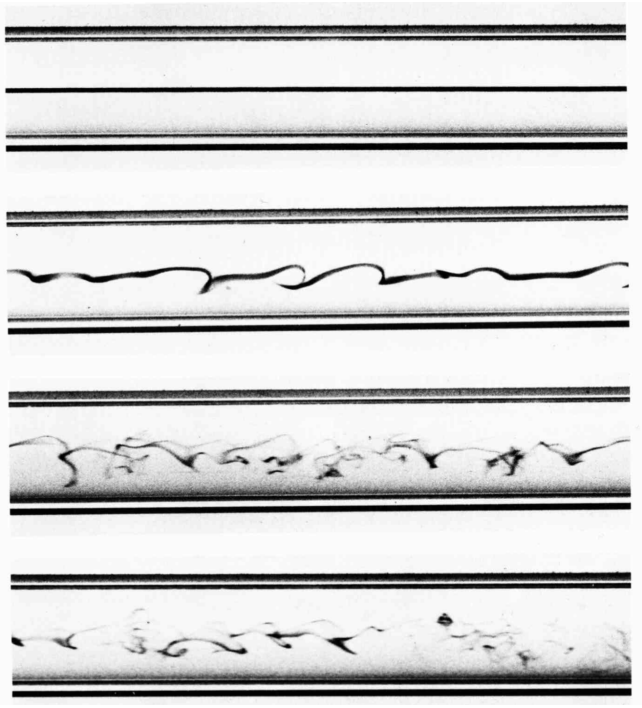

Figure 2.3: Repetition of Osborn Reynolds's experiment with dye, 1883. Laminar flow allows the colored water to flow undisturbed for the whole length of the glass tube. Transition is displayed in the second photograph. Last two figure show fully turbulent flows. [37]

From a certain value of Re, that usually is not easy to define precisely[5], the flow is fully turbulent. In this chaotic background caused by the turbulent regime, the flow is not reproducible in a deterministic manner, but it is reproducible from a statistical point of view.

[5]Flows can show an intermittent behaviour in some intervals of Re number.

2.1.2 Plane channel flow

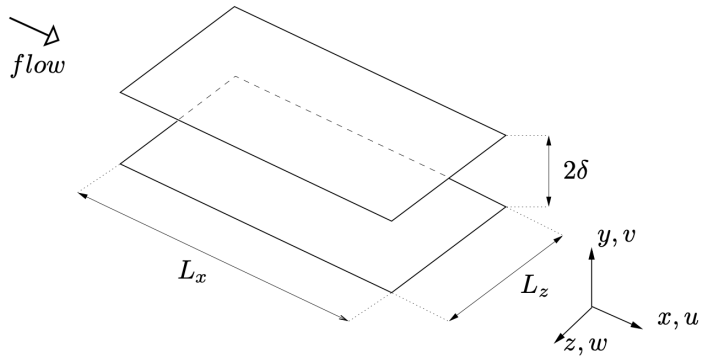

Figure 2.4: Schematic geometry of a plane channel flow. [26]

Since the current work aim to analyze the plane channel flow, probably the simplest among all wall bounded flows, it is important to specify the previous quantities to this specific problem. A rectangular duct of height $h = 2\delta$ is considered, the duct is bounded by two parallel semi-infinite smooth wall and the flow is driven by a pressure gradient mainly in the longitudinal direction x.

The flow is considered as fully developed; no initial transient or boundary effect at the exit are taken in consideration, hence the flow statistics are independent of x. The extent of the channel in spanwise direction z is infinite (or at least $b >> \delta$) in order to make the flow statistically independent of z. The flow considered is the fully developed channel flow, statistically stationary and statistically one-dimensional, with velocity statistics depending only on y. The flow is statistically symmetrical about the mid plane, located at $y = \delta$.

It is usually convenient to divide the velocity field in a velocity vector (u, v, w) and the fluctuations (u', v', w') according to the Reynolds decomposition[6]. Because of no pressure gradient in z direction, $w = 0$.

At first, two possible Re numbers are immediately defined, one based on the bulk velocity U_b:

$$U_b = \frac{1}{\delta}\int_0^\delta \overline{u} dy \tag{2.3}$$

and the other based on the velocity at the centerline, namely U_c, that is calculated as the velocity at $y = \delta$ for a laminar flow that produces the same flow rate as the turbulent one. Reynolds numbers are:

$$Re_b = \frac{U_b \delta}{\nu} \qquad Re_c = \frac{U_c \delta}{\nu} \tag{2.4}$$

[6]When a bar is placed over a symbol, the expected value is intended. In experiments and simulations the expected value is substituted with his best approximation available:

$$\bar{\cdot} = \frac{1}{T_{exp}}\int_0^{T_{exp}} \cdot dt \tag{2.2}$$

If one recalls incompressible Navier-Stokes equations, the mean continuity equation with Reynolds decomposition and the mean momentum equation in y-direction lead to:

$$\frac{d\overline{v}}{dy} = 0 \qquad -\frac{d}{dy}\overline{v'^2} - \frac{1}{\rho}\frac{\partial}{\partial y}\overline{p} = 0 \tag{2.5}$$

Integration of moment equation:

$$\overline{v'^2} + \frac{\overline{p}}{\rho} = \frac{p_w(x)}{\rho} \tag{2.6}$$

Derivation with respect to x and imposition of no-penetration boundary condition show that pressure gradient is uniform across the flow:

$$\frac{\partial}{\partial x}\overline{p} = \frac{d}{dx}p_w \tag{2.7}$$

Finally, using mean x-momentum equation:

$$\frac{d}{dy}\tau(y) = \frac{d}{dx}p_w = constant \tag{2.8}$$

with $\tau(y)$ defined as:

$$\tau(y) \equiv \nu\rho\left(\frac{d}{dy}\overline{u}\right) - \rho\overline{u'v'} \tag{2.9}$$

At the wall, boundary conditions states that velocity are null, the second term of $\tau(y)$ vanishes:

$$\tau_w = \rho\nu\left(\frac{d}{dy}\overline{u}\right)\Big|_w \tag{2.10}$$

Being $\tau(y)$ an odd function linear in y:

$$\tau(y) = \tau_w\left(1 - \frac{y}{\delta}\right) \tag{2.11}$$

Total shear stress $\tau(y)$ are the sum of viscous stress $\nu\rho\left(\frac{d}{dy}\overline{u}\right)$ and Reynolds stress $-\rho\overline{u'v'}$, while Reynolds stresses are null at the wall because of boundary condition: in this very close to the wall region the viscous stress dominates.

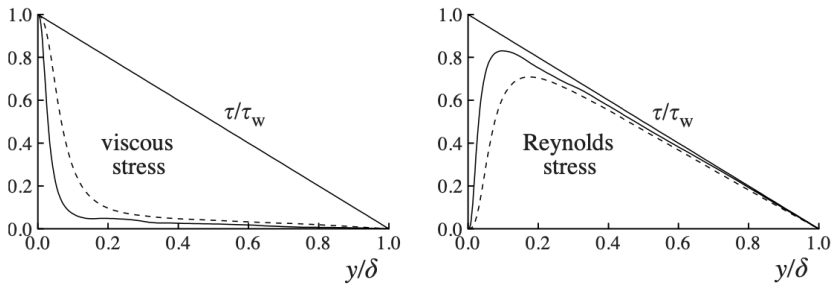

Figure 2.5: Profiles of the viscous shear stress, and the Reynolds shear stress in turbulent channel flow. DNS data of Kim et al. (1987): dashed line, $Re = 5,600$; solid line, $Re = 13,750$. [24]

Since this region is dominated by viscosity, τ_w and ν are two important parameters, along with ρ, to determine what happen in this region. An inner scaling that define a velocity scale, a length scale and a time scale can be defined as follow:

$$u_\tau = \sqrt{\frac{\tau_w}{\rho}} \qquad \delta_\nu = \frac{\nu}{u_\tau} \qquad t_\nu = \frac{\delta_\nu}{u_\tau} \tag{2.12}$$

The inner scaling leads to the definition of a new set of non-dimensional coordinates in the wall-normal direction of fundamental importance in turbulence. This new set of coordinates (namely, wall units) is recognizable by the + superscript and is simply defined as:

$$y^+ = \frac{y}{\delta_\nu} \tag{2.13}$$

Near-wall region is usually described in + units and divided in multiple layers and sublayers. The region that includes $0 < y^+ < 50$ is defined as the inner layer or viscous wall region; instead, $y^+ > 50$ defines the outer layer. In the inner layer, molecular viscosity directly affect shear stress $\tau(y)$ but Reynolds stresses are not negligible in general; region $0 < y^+ < 5$ define the viscous sublayer, here Reynolds stresses are negligible because of the proximity of the wall. In the viscous sublayer the mean velocity profile is linear thanks to no-slip boundary conditions:

$$\overline{u^+} = y^+ + O(y^{+4}) \tag{2.14}$$

where $u^+ = \overline{u}/u_\tau$.

Region $5 < y^+ < 30$ is called the buffer sublayer because it is the transition region between the viscosity-dominated and the turbulence-dominated parts of the flow. The viscous length scale is used to define the friction Reynolds number, namely Re_τ:

$$Re_\tau = \frac{u_\tau \delta}{\nu} = \frac{\delta}{\delta_\nu} \tag{2.15}$$

If Re_τ increases, the dimensions of the inner layer and all the related sublayers diminish because of $\delta_\nu/\delta \sim Re_\tau^{-1}$.

It is finally possible to derive the law of the wall; for $y << \delta$, u^+ depends solely on y^+ and can be described by a universal function. For big values of y^+, viscosity has a very little effect and the universal function described previously become constant:

$$\frac{d\overline{u^+}}{dy^+} = \frac{1}{y^+}\Phi(y^+) = \frac{1}{y^+\kappa} \tag{2.16}$$

with κ being the Von Kàrmàn constant[7].

The logarithmic law of the wall is valid in the log-layer ($y^+ > 30$ and $y < 0.1\delta$) but holds till $y \approx 0.3\delta$:

$$\overline{u^+} = \frac{1}{\kappa}\ln(y^+) + B \tag{2.17}$$

where $B \approx 5.2$. An exhaustive summary table about the layers and sublayers is in [24], pag. 275.

[7] κ has not a precise value, but it is usually kept constant at $\kappa = 0.41$.

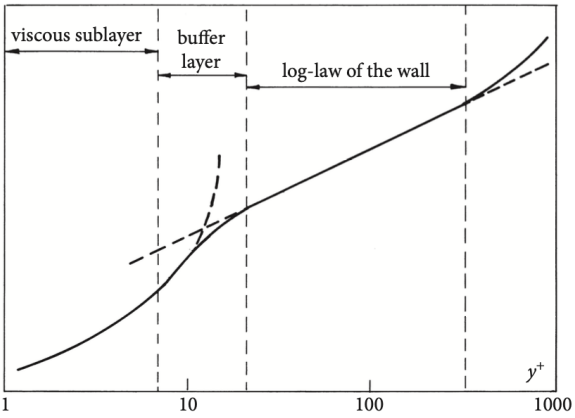

Figure 2.6: A plot of $\overline{u}^+$ versus y^+ showing the log-law of the wall. [8]

2.1.3 Friction coefficient

The log-law can be used to calculate the value of the skin-friction coefficient C_f. C_f can be defined in different way according to the velocity used in the definition:

$$c_f = \frac{\tau_w}{\frac{1}{2}\rho U_c^2} = 2\left(\frac{u_\tau}{U_c}\right)^2 \qquad C_f = \frac{\tau_w}{\frac{1}{2}\rho U_b^2} = 2\left(\frac{u_\tau}{U_b}\right)^2 \tag{2.18}$$

Using the log-law for the whole channel, one obtains a good approximation for the value of the bulk velocity. The viscous region, where log-law is not valid, is very small compared to the height of the channel if Re is high enough; in the central part of the channel $y > 0.3\delta$ the log-law is not valid either way, but the difference is so small that one can extend the log-law in this region. Using the previous approximation:

$$\frac{U_c - U_b}{u_\tau} = \frac{1}{\delta}\int_0^\delta \frac{U_c - \overline{u}}{u_\tau} dy \approx \int_0^\delta -\frac{1}{\kappa}\ln\left(\frac{y}{\delta}\right) dy = \frac{1}{\kappa} \approx 2.4 \tag{2.19}$$

The log-law in the inner layer and in the outer layer is respectively:

$$\frac{\overline{u}}{u_\tau} = \overline{u^+} = \frac{1}{\kappa}\ln\left(\frac{y}{\delta_\nu}\right) + B \qquad \frac{U_c - \overline{u}}{u_\tau} = -\frac{1}{\kappa}\ln\left(\frac{y}{\delta}\right) + B_1 \tag{2.20}$$

Combine the two last equation to make y-dependence vanish:

$$\frac{U_c}{u_\tau} = \frac{1}{\kappa}\ln\left(\frac{\delta}{\delta_\nu}\right) + B + B_1 = \frac{1}{\kappa}\ln\left[Re_c\left(\frac{U_c}{u_\tau}\right)^{-1}\right] + B + B_1 \tag{2.21}$$

Using this relation, in equation 2.18, allow to find the skin-friction coefficient c_f only imposing Re_c[8] for a plane channel flow. As reported in [24], a useful relation to evaluate the trend between Re_b and lengthscale ratio $\frac{\delta}{\delta_\nu} = Re_\tau$ is:

$$Re_\tau \approx 0.09 Re_b^{0.88} \tag{2.22}$$

[8] Using similar procedure and equation 2.19, it is possible to find a relation between Re_b and C_f.

2.1.4 Reynolds stresses

Reynolds stresses play a major role in the determination of the value of C_f. Averaging NS equations with Reynolds decomposition lead to the comparison of non-linear terms referred as (apparent) Reynolds stresses.

$$\frac{\partial \overline{u_j}}{\partial t} + \overline{u_i}\frac{\partial \overline{u_j}}{\partial x_i} = \nu \frac{\partial^2 \overline{u_j}}{\partial {x_i}^2} - \frac{\partial \overline{u_j' u_i'}}{\partial x_i} - \frac{1}{\rho}\frac{\partial \overline{p}}{\partial x_j} \tag{2.23}$$

with Reynolds stresses being:

$$\tau_{ij}^R = -\rho \overline{u_i' u_j'} \tag{2.24}$$

This "new" term couple the mean flow with turbulence. Turbulent flows are characterized by a greater momentum diffusion with respect to laminar flows; a physical and intuitive possible explanation of Reynolds stresses is that they work as convection in small scales and from a mean-flow point of view they appear as diffusion. Davidson, in [8], define Reynolds stresses as something that act like stresses but represent the mean momentum fluxes induced by the turbulent fluctuations. It is possible to write an equations for Reynolds stresses by manipulation[9] of the averaged equations, and this equation can be found on [8] for example; the resulting equation is complex and it is not closed because of a triple-correlation term: $\overline{u_i' u_j' u_k'}$.

Reynolds stresses arose from the averaging process, that only consists of a manipulation: they can not create or destroy mechanical energy of the fluid. Anyway, τ_{ij}^R play an important role in Turbulent Kinetic Energy (TKE) equation and Mean-flow Kinetic Energy(KE) equation. As they are limited in the creation and destruction of mechanical energy, Reynolds stresses will appear in the first equation as a source term (P) and as a loss term ($-P$) in the second one; τ_{ij}^R transfer energy from the mean flow to fluctuation velocity field. Looking at the source term in the TKE:

$$P = -\overline{u_i' u_j'}\frac{\partial \overline{u_i}}{\partial x_j} \tag{2.25}$$

one can recognize that production of TKE is achieved only when the rate of strain is not negligible ($\overline{s_{ij}} = \frac{\partial \overline{u_i}}{\partial x_j} \neq 0$); turbulence stay alive only in presence of a rate of strain or it decays. This transfer of energy from mean-flow KE to TKE is the reason because a turbulent pipe flow needs more energy to be driven.

If one performs a Taylor expansion near the wall for the mean square fluctuation velocity in order to understand Reynolds stresses near the wall, the result obtained by imposing no-slip boundary conditions and continuity is:

$$\overline{u'^2} \sim {y^+}^2 \tag{2.26a}$$

$$\overline{v'^2} \sim {y^+}^4 \tag{2.26b}$$

$$\overline{w'^2} \sim {y^+}^2 \tag{2.26c}$$

$$\overline{u'v'} \sim {y^+}^3 \tag{2.26d}$$

[9] Write equation for u_i and subtract equation for $\overline{u_i}$. The obtained equation for u_i' is multiplied by u_j' to obtain equation for $u_i' u_j'$. Average in time the resulting equation to obtain equation for $\overline{u_i' u_j'}$.

This relations are important to the scope of the present work; indeed, they are related to the trend of the terms in TKE equation in the proximity of the wall. The near-wall region is probably the most important region of study because is the region where the turbulent activity gives the biggest contribution.

2.1.5 Coherent structures and wall cycle

The idea behind coherent structures (CS) is that the flow usually shows some patterns that are recurrent in the flow and that are significantly larger than the small turbulent scales. Coherent structures, as reported in [10], are non-stationary systems that are not a direct consequence of the particular geometry of a region and have a life-span typically at least the average passage time of a structure; their appearance is quasi-periodic (typically stochastically intermittent). Coherent structures show different shapes in relation to the Re number and to the specific region where they are, the behaviour and presence of CS with the Reynolds number is not "linear".

As reported in [32], the generation and evolution of coherent structures is not fully understood, but the dominant role of streamwise vortices near the wall in turbulence production and drag is widely accepted. Although the outer layer also contains energetic (larger) structures, recent numerical experiments confirm that the essential inner-layer dynamics (namely $y+ < 60$) can operate autonomously.

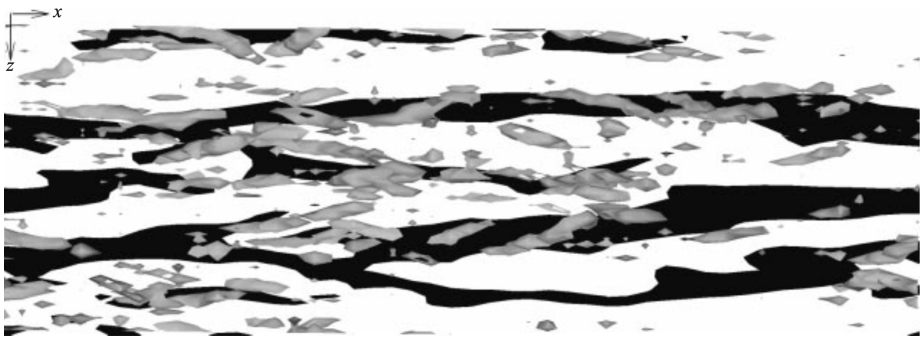

Figure 2.7: Top view of the near-wall region covering $(x^+, z^+) = (1400, 450)$ in the streamwise and spanwise directions. Lifted low-speed streaks (black) denote $u' < 0$ at $y^+ = 20$ and streamwise vortices (grey-shaded) are indicated by the $\lambda 2$ vortex definition in the region $0 < y^+ < 60$. [32]

In figure 2.7, streamwise vortices and elongated 'streaks' of relatively lower-speed and less-stirred fluid are shown; the so called bursting.

It is possible to find several CS present in a turbulent flow, here it is a list that is not exhaustive:

- sweep, high-speed fluid ($u' > 0$) towards the wall of the channel ($v' < 0$)
- ejections, low-speed fluid ($u' < 0$) towards the center of the channel ($v' > 0$)

- quasi-streamwise vortices (QSV), their axes is aligned with the streamwise direction; they play a major role in the wall cycle that will be explained later in this chapter
- low-speed streaks (LSS), elongated structures (in the order of $1000y^+$) in the viscous sublayer (for y^+10) that have a negative fluctuation velocity ($u' < 0$) because are slower than mean-flow
- superstructures, these are the last discovery in the field of CS, they consist of continuous structures of length in the order of the height of the channel or more.

In general, CS interact each other and strongly influence the production and the balance of TKE; the so called wall cycle is maybe the most important among this interactions and explain the mechanism of TKE production in the wall-region; the the inhibition of the wall cycle, as a great source of TKE production, is one of the main strategy used for drag reduction purposes. The wall-cycle is characterized by sweeps to the wall and ejections from the wall, this events are generated by a self-sustained mechanism that is well explained in [31] and summarized here.

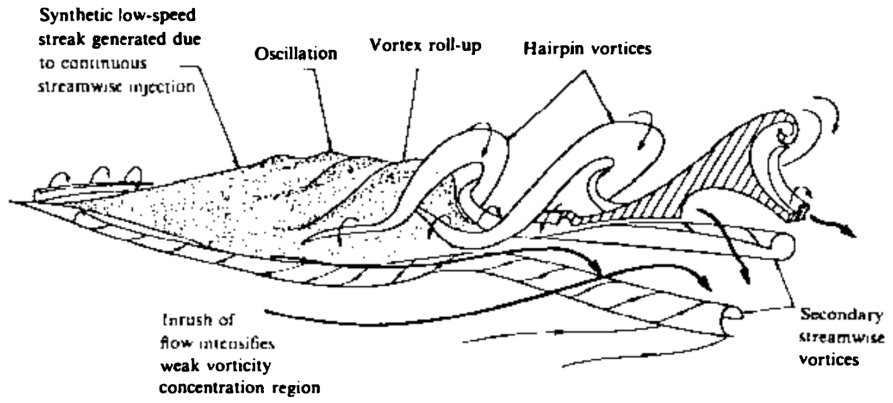

Figure 2.8: Schematic of breakup of a synthetic low-speed streak generating hairpin vortices. Secondary streamwise vortical structures are generated owing to inrush of fluid. [31]

QSV are vortexes aligned with the streamwise direction that rotate in opposite direction one w.r.t. to the other; the opposite rotation generate some streaks of high-speed and some streaks of low-speed (LSS). This last mechanism is the responsible of the ejections and sweeps events. LSS in the proximity of the wall shows a transient growth due to non-normality of NS system (non-modal analysis should explain the phenomenon), they create a train of QSV.

The precise mechanism that bring to the creation of QSV is not completely clear, but some in literature [32] believe that small perturbations in the spanwise direction are enough to generate new vortexes and sustain the wall cycle. It is important to understand that wall cycle is not directly influenced by the superstructures described before, the two phenomena take place in different region of the channel and are characterized by a different lenghtscale.

2.2 Flow control for turbulent DR

Flow control techniques in turbulent flows can be used for various purposes, but drag reduction is the main goal of flow control. Drag force can be broken down in two main contributions:

- Pressure drag
- Skin friction drag, due to viscosity

and turbulent flow control address the latter of the two contributions.

The current work aims to discuss about an open-loop active flow control; the focus on this kind of techniques is due to the fact that closed-loop flow control techniques are generally too complex and too expensive. On the contrary, passive strategies are simpler from a conceptual point of view and some (uncommon) examples are already present in real applications, but they are generally expensive to make with respect to the power savings that provide.

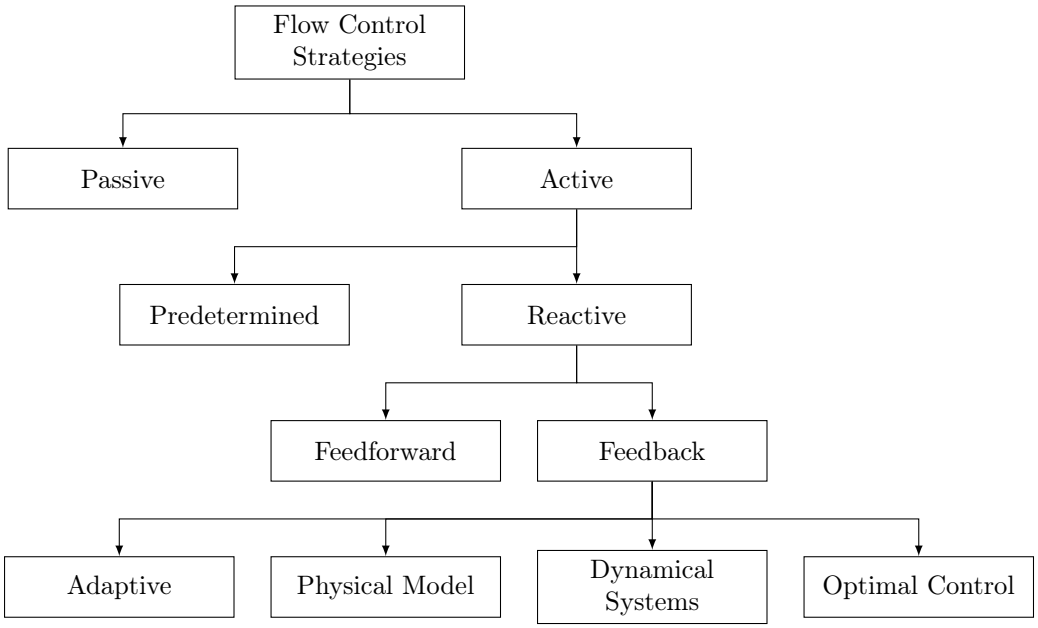

Figure 2.9: Classification of the different DR techniques.

This chapter will briefly explain the basic concept of flow control and will list some flow control techniques to understand how they work and how they interact with flow structures, with a major focus on the streamwise travelling waves.

2.2.1 Passive flow control

Passive flow control techniques are predetermined strategies that do not request external energy to work. In the following list will be summarized the most relevant passive strategies:

- **Polymer additives**: This strategy is frequently used in chemical engineering and in the oil&gas industry because of the sensible pressure drop in long (hundreds of kilometers) pipes. It is well known that the addition of a small amount of long-chain polymers to the turbulent flow of the Newtonian solvent can result in a drag reduction. The strain rate causes the molecules to expand, the increased effective viscosity damps the small eddies, but does not affect the viscosity deep in the viscous sublayer, where the molecules are not expanded. The local increase of viscosity in the buffer layer locally increase the viscous length scale, so the buffer layer result to be more thick than before. Since the layer remains turbulent, there is no stringent requirement for surface smoothness, as there is for many of the other techniques.

- **Riblets**: Since the idea of riblets comes from nature (the shark scales tend to be very similar to riblets), they are classified as a bio-mimetic material; riblets are very small grooves (about $10^{-5}m$ or $20\delta_\nu$) applied on the wall and aligned with the streamwise direction (Luchini in [20] presented also an analysis of cross-flow riblets). They can provide up to 10% reduction of the drag force and are not complex from a conceptual point of view. Riblets interact with the wall cycle in a positive manner; they stabilize QSV vortexes because the tip of the riblets meets the QSV vortex subtracting energy, the QSV vortexes are no longer able to sustain the wall cycle by inducing LSS.

- **Compliant coatings**: Compliant coatings are also derived from nature, the idea comes from the dolphin skin, that allow them to exceed the expected velocity they could reach. Compliant coatings are elastic surfaces that may deform under the effect of viscous forces; the coatings are able to deform in a favourable manner to delay transition to turbulent regime caused by Tollmien-Schlichting instabilities. In general, viscous force produced by an air flow is not enough to deform any coating, so they are mainly used in applications that involve liquids and not gasses.

2.2.2 Active flow control

Active techniques request external power to work, they generally achieve a larger reduction in the skin friction component of the drag force with respect to passive techniques, but they are generally more complex and expensive. They can be classified by the control strategy they use:

- **Predetermined**: output is determined a priori

- **Reactive**: output is determined by a control law. They can be divided in:

  - Feed-forward: The main control strategy of this kind is the opposite $v-$velocity at the wall, the control is presented in [6]. The researchers placed some sensors in the whole channel to detect velocity in the wall-normal direction v_d at a certain altitude ($y_d^+ = [5, 10, 20, 26]$), called detection plane; suction/blowing actuators produce $-v_d$ at the wall. This choice is probably intended to prevent sweeps and

ejections to happen, a negative fluctuation of wall-normal velocity from a sweep is opposed by a positive v at the wall and vice versa.

– Feed-back: these kind of strategies differ from the open-loop ones because of the measured quantities coincide with the output in this case. Sensors are usually placed on the wall to measure shear stress and pressure, zero mass flux suction/blowing actuators are also placed on the wall.

Both feed-forward and feed-back strategies, usually share a common problem: sensor and actuators involved in a real-life situation are incredibly numerous and need to work at extremely high frequency[10]. In this case implementation would be extremely complex and far too expensive also using piezo-electric actuators.

2.2.3 Streamwise travelling waves

The streamwise travelling waves are a predetermined drag reduction technique firstly described by Quadrio et al. in 2009 in [28] as a further development of both the spanwise oscillating wall [27] and the stationary spanwise forcing [38]. The spanwise oscillating wall consist of an unsteady boundary condition on wall that obey the law:

$$w_w(t) = A \sin(\omega t) \tag{2.27}$$

the previous equation does not show any dependence on the space coordinates and the phase angle can be disregarded because not relevant; the oscillation period can be related to oscillation frequency according to the relation $T = \omega/(2\pi)$. On the other hand, the stationary spanwise forcing is the counterpart of the previous forcing, the dependence on time is lost but the spatial one is recovered introducing the streamwise wavelength λ_x:

$$w_w(x) = A \sin(\kappa_x x) \tag{2.28}$$

with $\lambda_x = \kappa_x/(2\pi)$. If one introduces a convective velocity should ends up with a relation between the optimal wavenumber κ_x and the optimal oscillation period T. One should think to use a similar idea to Taylor's frozen turbulence, where the convective velocity is the mean streamwise velocity $\overline{u}$.

Turbulence still maintains a strongly convective character[11], evident from the elongated shape of the auto-correlation contours, even at the wall where the local mean velocity is zero, reported in [25]. It is useful to determine the convective velocity in the proximity of the wall ($y^+ < 10$) because of the great difference from the value of the mean velocity; this value is defined as: $\mathcal{U}$. For $y^+ > 15$ the convective velocity is approximated equal to $\overline{u}$, in the near-wall layer it is approximately constant and $\mathcal{U}_w^+ \approx 10$. Finally, the relation between the optimal wavelength and the optimal oscillation frequency reads:

$$\kappa_{x,opt} = \frac{\omega_{opt}}{\mathcal{U}_w} \tag{2.29}$$

[10] It can be estimated that a common civil aircraft would need $10^6 elements/m^2$ that work at $f = 10^4 Hz$.

[11] It is important to distinguish between the characteristic size of a turbulent structure and the characteristic space travelled by the structure to identify a correct lengthscale and convective velocity. The Taylor's frozen turbulence is valid near the center of the channel, where the convective velocity is similar to the mean streamwise velocity.

The extension of the present cases to the streamwise travelling waves is the direct consequence of imposing both $\kappa_x \neq 0$ and $\omega \neq 0$. The space-time law that governs the spanwise velocity boundary condition on the wall is:

$$w_w(x,t) = A\sin\left(\kappa_x x - \omega t\right) \tag{2.30}$$

The previous law stands for an oscillating wave moving in the streamwise direction, the phase speed of the wave is:

$$c = \frac{\omega}{\kappa_x} \tag{2.31}$$

2.2.4 Measure of drag reduction and power saving

In section 2.1.3 were defined c_f and C_f, that are also reported here:

$$c_f = \frac{\tau_w}{\frac{1}{2}\rho U_c^2} = 2\left(\frac{u_\tau}{U_c}\right)^2 \qquad C_f = \frac{\tau_w}{\frac{1}{2}\rho U_b^2} = 2\left(\frac{u_\tau}{U_b}\right)^2 \tag{2.32}$$

It is possible to define a mean friction coefficient for the two walls:

$$C_f = \frac{C_{f,top} + C_{f,bot}}{2} \tag{2.33}$$

where $C_{f,top}$ and $C_{f,bot}$ are the values of C_f on the top wall and bottom wall.

Kasagi et al. in [14] defined a simple relation for C_f in turbulent channel flow at constant flow rate, exploiting the first laminar contribution and the second contribution due to Reynolds stress:

$$C_f = \frac{12}{Re_b} + 24\int_0^1 (1-y)\left(-\overline{u'v'}\right)dy \tag{2.34}$$

A similar consideration can be done for constant pressure channel flow, the turbulent regime affect the bulk velocity with a negative contribution:

$$U_b = \frac{Re_\tau}{3} - \frac{Re_\tau}{2}\int_0^1 (1-y)\left(-\overline{u'v'}\right)dy \tag{2.35}$$

Broadly speaking, the power required only to drive the flow across the channel by an ideal pump is:

$$P = \overline{Q\frac{\partial p}{\partial x}} \tag{2.36}$$

where Q is the volume flow rate and $\partial p/\partial x$ is the pressure gradient in streamwise direction. According to [27], the power savings can be expressed as:

$$\begin{aligned} P_{sav} = U_b\frac{L_xL_z}{t_f-t_i}\int_{t_i}^{t_f}\frac{1}{L_xL_z}\int_0^{L_x}\int_0^{L_z}\rho\nu\left[\left(\left.\frac{du}{dy}\right|_{w,0}^{l} - \left.\frac{du}{dy}\right|_{w}^{l}\right) + \left(\left.\frac{du}{dy}\right|_{w,0}^{u} - \left.\frac{du}{dy}\right|_{w}^{u}\right)\right]dxdzdt = \\ = U_b\frac{L_xL_z}{t_f-t_i}\int_{t_i}^{t_f}\left[\left(\tau_{x,0}^{l}-\tau_x^{l}\right) + \left(\tau_{x,0}^{u}-\tau_x^{u}\right)\right]dt \end{aligned} \tag{2.37}$$

where L_x and L_z are the dimension of the channel in streamwise and spanwise direction, t_f and t_i are final and initial time of the simulation, τ_x are wall shear

stress averaged in $x-$ and $y-$direction, the superscript u or l denotes the upper and lower wall, the subscript 0 stands for the uncontrolled case. Hence, the parameter to assess the power saving after the implementation of DR strategy is:

$$R = \frac{P_0 - P}{P_0} = \frac{P_{sav}}{P_0} \tag{2.38}$$

where P_0 is the power required by the channel flow before the implementation of the control. It is worth noticing that constant pressure gradient simulations obtain a grater Q when DR is achieved and C_f decreases. Instead, in case of constant flow rate simulations the drag reduction can be quantified as:

$$R = \frac{C_{f,0} - C_f}{C_{f,0}} \tag{2.39}$$

thanks to the fact that U_b is constant in this case.

For an active control strategy, one must account for the power required by the control system to work, namely P_{req}. The streamwise travelling waves are no exception and they require an external power source in order to move the walls and impose the desired boundary condition; the wall is moved against the viscous stress at wall. The analitic formula can be found in [27].

The balance considering P_{req} now tells the net energy saving S:

$$S = \frac{P_0 - (P + P_{req})}{P_0} \tag{2.40}$$

and finally the gain G defined as:

$$G = \frac{P_0 - P}{P_{req}} \tag{2.41}$$

The previous relations are written for ideal actuators of efficiency equal to 1; obviously, in order to obtain a net energy saving, $(S > 0)$, G need to be larger than 1. The actuator efficiency should be grater then $1/G$ to obtain a net energy saving.

2.2.5 State of the art

Some works in the past years addressed the topic of streamwise travelling waves of spanwise velocity and the related cases of $\kappa_x = 0$ or $\omega = 0$.

2.2.5.1 Stationary spanwise forcing

The reference work for the stationary spanwise forcing is [38] by Viotti et al. the main purpose is to investigate the effectiveness of the technique with respect to the spanwise oscillating wall. The research exploited the so called temporal Stokes layer (TSL) and spatial Stokes layer (SSL), the former is obtained when the wall oscillates ($\kappa_x = 0$) and is analytically defined in the laminar regime by the superposition of the laminar solution of the Poiseuille flow and the Stokes second problem in the spanwise direction. The analytical solution of w is:

$$w(t, y) = C\ \mathcal{R}\left[e^{i\omega t} e^{-y\delta_t}\right] \tag{2.42}$$

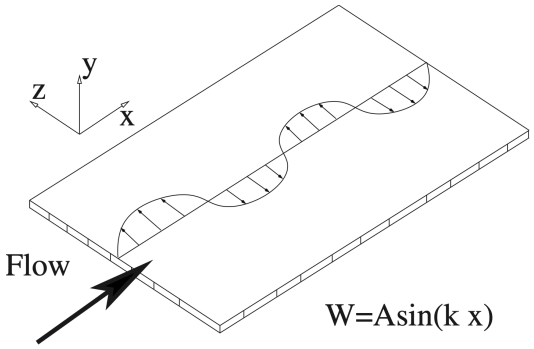

Figure 2.10: Sketch of the wall stationary spanwise forcing. [38]

where C is a dimensional constant and $\delta_t = \left(\frac{\nu}{\omega}\right)^{\frac{1}{2}}$ is the thickness of the TSL. A similar, but more complex, procedure[12] can be done to obtain the function of w in the SSL ($\omega = 0$) under the hypothesis of small thickness, with Ai being the Airy function:

$$w(x,y) = C\ \mathcal{R}\left[e^{i\kappa_x t} Ai\left(-\frac{iy}{\delta_x} e^{-i4/3\pi}\right)\right] \tag{2.43}$$

and the SSL thickness $\delta_x = \left(\frac{\nu}{u_{y,0}\kappa}\right)^{\frac{1}{3}}$, $u_{y,0}$ is the gradient of the velocity profile at the wall.

The DR computed here (SSL) has a maximum for $\lambda_x^+ = 900 - 1250$ and monotonically increase with the values of A but it tends to an asymptotic behaviour. The net power saving peak is not obtained using the same parameters that achieve the maximum drag reduction, because P_{req} increase approximately linearly with A. Anyway, the DR in the SSL case is greater than the one computed in the TSL case, with peak values that are 30% grater.

The flow control has a direct influence on the turbulent structures present in the flow; using the controversial but necessary λ_2 criterion[13] is possible to identify turbulent vortical structures. The presence of vortical structures in the near-wall region is drastically decreased as shown in figure 2.11, the statistical description of the controlled flow confirm the trend.

Indeed, the presence of the SSL (and similarly of the TSL) manifest itself through the thickening of the viscous sublayer. The thickening of the viscous sublayer causes the logarithmic region to shift upward: this effect is strongly related to drag reduction, as shown in many other articles related to passive techniques, as previously described in section 2.2.1 and in Lumley research [22].

Finally, another statistical indicator that can be used to assess DR is root mean square (rms) value of the fluctuations of the streamwise velocity component, the turbulence intensity. A reduction in the profile of ${u'}^+_{rms}$ stands for a

[12] Described in appendix of [38].

[13] The criterion is explained in [12] and is quite complex, if the second eigenvalue of the $S^2 + \Omega^2$ matrix is below a threshold, the region is identified as a vortex core. S and Ω are the symmetric and anti-symmetric part of $\nabla\mathbf{u}$.

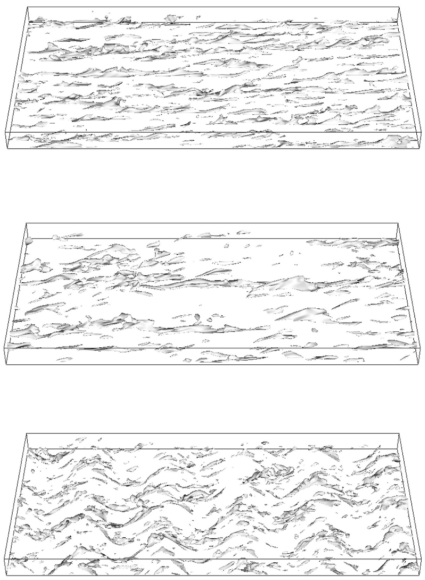

Figure 2.11: Snapshots of instantaneous flow fields for the reference flow (top), a case with DR (middle, $\kappa_x = 1.66$ and $\omega = 0.16$) and a case with DI (bottom, $\kappa_x = 1.66$ and $\omega = 0.88$). Isosurfaces for the quantity $q = sgn(u)\sqrt{u^2 + w^2}$ at the value $q^+ = -4$. The value $q^+ = -4$ is computed with the actual friction velocity of the drag-modified flow. The flow is from left to right and only the bottom half of the channel is shown. For both cases $A = 0.5$ and $Re = 4760$. [28]

reduction of the skin-friction drag, the rms value of u is defined as:

$$u'_{rms} = \sqrt{\overline{u'u'}} \tag{2.44}$$

and then scaled with u_τ to obtain the + variable.

2.2.5.2 Streamwise travelling waves

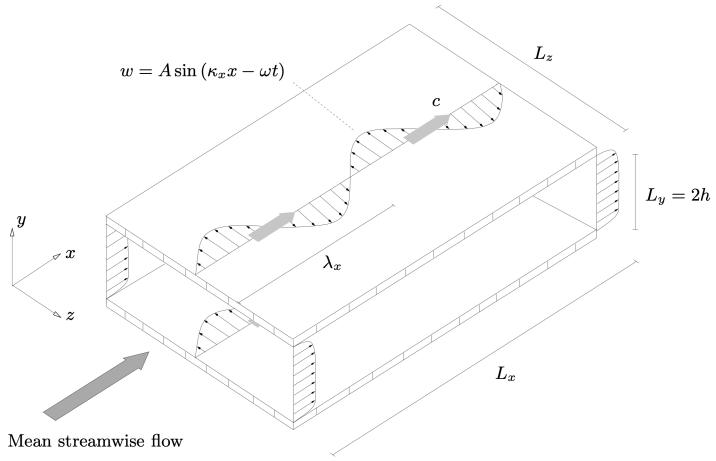

Figure 2.12: Schematic of the system for turbulent channel flow with wall travelling waves. λ_x is the streamwise wavelength and c is the phase speed of the waves (travelling forward in this sketch). [28]

Streamwise travelling waves (StTW) were firstly introduced by Quadrio et al. in [28] in 2009; the behaviour of the StTW revealed to be a bit different from the TSL ans SSL previously described and investigated by Viotti et al. in [38]. The main target of the research is to investigate drag reduction R in the $\omega - k_x$ plane and find regions of positive net power saving S; additional simulations at $Re = 2175$ and $Re = 10500$ have been performed to explore sensitivity to Reynolds number.

The results reported in figure 2.13 show only positive values of κ_x since the problem is symmetric because of the formula 2.30; the first quadrant contains the waves travelling with the flow ($c > 0$), instead the second quadrant is for backward-travelling waves ($c < 0$). Furthermore, as previously stated in equation 2.29, the values on the κ_x axis and the ω axis can be related by using the convective velocity with value[14] $\mathcal{U} = 0.5$.

The results show that the maximum DR achieved is 48%; quite close to 45% obtained by the SSL and significantly higher than the 34% of the TSL. It is clearly defined a drag increase conical region, starting from the origin, with boundary at $c = 0.35$ and $c = 0.6$, with the crest of DI for $c = 0.5$. The DR region includes the whole place except for the small DI region, but the most significant values are obtained in the first quadrant with the peaks of $47 - 48\%$ that form a crest that crosses the κ_x axis at $\kappa_x = \kappa_{x,opt}$ (with $DR = 45\%$).

[14]The value is normalized by U_p

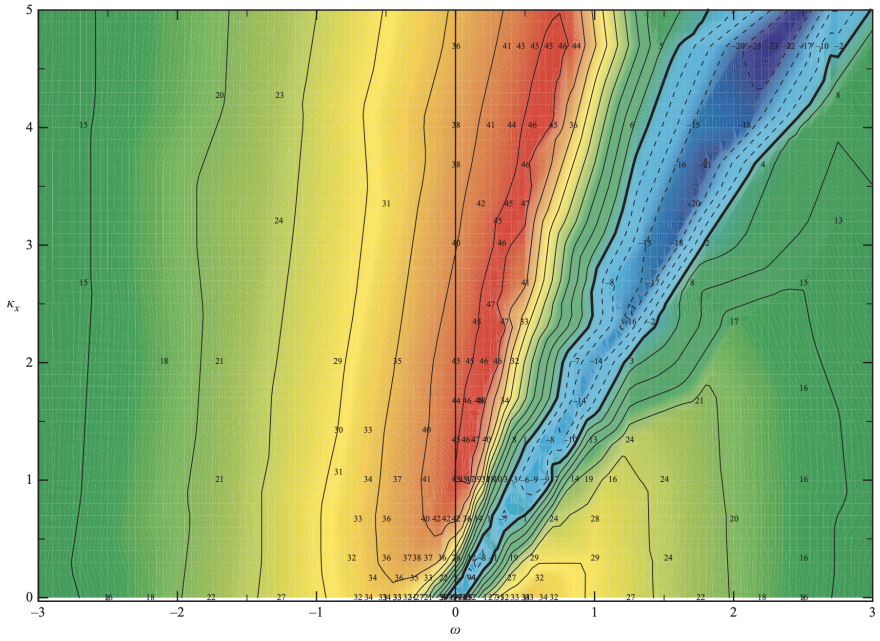

Figure 2.13: Map of friction DR(%) in the $\omega - k_x$ plane for $A = 0.5$ and $Re = 4760$. Contours are spaced by 5% intervals, loci of zero DR are indicated by thick lines and negative values are represented by dashed lines. The numbers indicate percentage DR at measured points. [28]

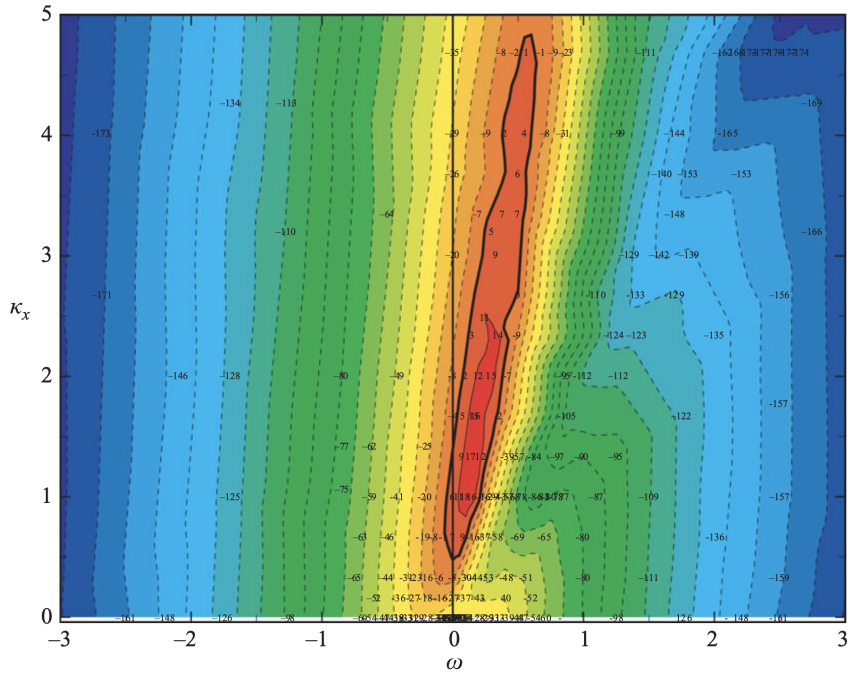

Figure 2.14: Map of net power saving $S(\%)$ in the $\omega - k_x$ plane for $A = 0.5$ and $Re = 4760$. Contours are spaced by 10% intervals. Locus of zero $S(\%)$ is indicated by thick curve, solid lines denote positive balance and negative values are represented by dashed lines. The numbers indicate $S(\%)$ at measured points. [28]

The value of $A = 0.5U_p$ is chosen as the best trade-off between the DR achieved and the power expense to generate the forcing; indeed, the DR achieved monotonically increase with A but it reach an asymptote while the power required increases linearly.

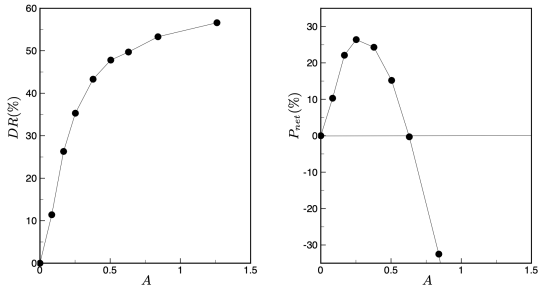

Figure 2.15: Percentage drag reduction (left) and net power saving (right) as functions of forcing amplitude A. The forcing conditions are $\omega = 0.16$, $\kappa_x = 1.66$, which produce the maximum drag reduction at $A = 0.5$ and $Re = 4760$. [28]

2.3 About the present work: Plasma Actuators

The current work aims to quantify the performance degradation of wall stationary spanwise forcing, described in 2.2.5.1, when it comes to apply the technique in a real situation. Indeed, it is difficult to impose the moving wall boundary condition on an airplane wing, inside an oil pipe or in a duct; it is necessary to find alternative solutions that are economically sustainable and of practical use. The solution proposed in this work is to use dielectric barrier discharge (DBD) plasma actuators that produce spanwise body forces to replicate the effect of the SSL DR technique proposed by Viotti et al. in [38]. Lately, plasma actuators are of great interest in the aeronautical field, they are currently used as flow control devices to delay separation and augment lift on a wing.

Several actuators are positioned parallel, 2.16, to each other along the streamwise direction; it is important to understand that the best solution would be to have a continuous forcing with no interruption in the spanwise direction, but this is not the case because of the technology used to produce the forcing and the distance between each actuator.

2.3.1 DBD Plasma actuators

Plasma actuators are electrical devices that generate a wall bounded jet without the use of any moving parts. The standard plasma actuator consists of a single encapsulated (ground) electrode. As reported in [9], the system consists of two electrodes offset in the chordwise (spanwise in the current study) direction and separated by a dielectric layer, typically Kapton, glass, quartz or ceramics. The encapsulated electrode is connected to the earth and the exposed electrode is attached to a high voltage supply.

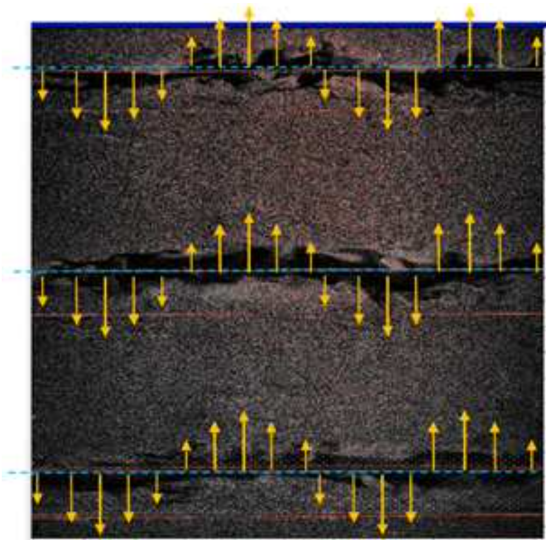

Figure 2.16: Top view of the plasma actuators disposed parallel to each other. Picture from Benard et al.

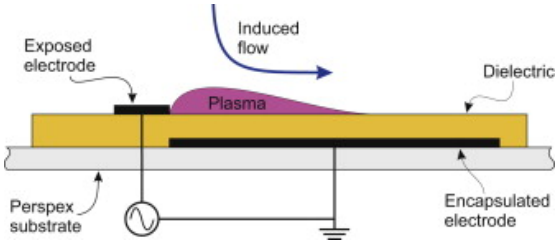

Figure 2.17: Standard SDBD actuator configuration. [9]

Since the system typically requires voltages in the kV range and applied with an a.c. frequency in the kHz range, the actuators presented here require voltages between 12 and 20 kV applied at 1000 Hz. When activated, a purplish glow plasma is visible, originating at the exposed electrode and spreading out across the dielectric surface that is above the encapsulated electrode as shown in figure 2.17. The plasma is ionised air consisting of ions and electrons with the bulk plasma exhibiting electrical neutrality. The remarkable aspect of this arrangement is the ability to produce a steady jet that flows away from the exposed electrode across the encapsulated electrode without the need for any moving parts. The plasma actuator is lightweight, easy to repair, flexible and able to follow the curvature of the surface it is applied to; therefore, it is possible to precisely modulate the encapsulated electrode as a sine.

The induced flow can be changed in intensity by changing the supply voltage or frequency, actuators can be easily switched off with no remaining influence on the flow; the entire system is all-electric and fits in well with the current ethos of aircraft manufacturers to produce all electric aircrafts.

2.3.2 Experiments to assess the body force distribution

The experimental campaign used for the work is performed by experimental laboratories at Poitiers University by N. Benard. The study conducted aims to determine the electro-hydro-dynamic (EHD) body forces (in space and in time) produced by a DBD plasma actuator. As reported in [5], by inversion of the Navier-Stokes equations, the spatial distribution of the mean EHD force is evaluated based on the mean velocity field, for different supply voltages and frequencies.

A particle image velocimetry (PIV) system determines the velocity field; once $\mathbf{u}$ is known, it is possible to determine the diffusion and the non-linear terms in the iNSEs, here obtained by finite difference method with second order spatial schemes. The sum of the remaining terms, i.e. the pressure gradient (with negative sign) and the body forces vector, is easily obtained. The pressure gradient results to be negligible with respect to the body forces obtained in the experiments, the $\mathbf{b}$ vector is finally obtained.

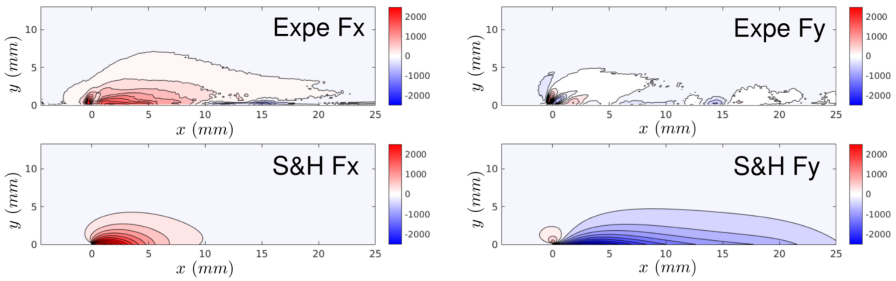

Figure 2.18: Spatial distribution of the wall-parallel (left) and wall-normal (right) components of the forcing term from the experimental data (top), from the Suzen-Huang model (bottom). Force in $\mathrm{N\,m^{-3}}$. [5]

The experiment compared the body forces distribution obtained by the Suzen-Huang model and by the PIV experiments, Fig. 2.18. The horizontal component has both positive (red on the figure) and negative (blue on the figure) values; despite the positive forcing, if averaged, is clearly prevailing on the negative one, the wall region is probably going to suffer some ejections events due to the clash of two opposite induced flows. In addition, the vertical component of $\mathbf{b}$ is of the same order of magnitude of the spanwise one, probably causing vertical events of localized speed, known as sweep ($v' < 0$) and ejections ($v' < 0$), that are responsible of drag increase. Indeed, if the vertical component of the velocity near the wall is increased, the Reynolds stresses term $-\overline{u'v'}$, present in equation 2.34 for C_f, could rise. This last problem should be limited by introducing a trade off between the amplitude of the forcing that guarantees the maximum DR and the amplitude that limits the vertical forcing, as it will be addressed in the preliminary study of Chapter 4, or better by developing an enhanced actuator with a decreased vertical component. Furthermore, the experiment pointed out some differences between the phenomenological model and the experimental model, because the Suzen-Huang model (and neither the others) is not able to predict the thickness of the wall-jet close to the actuator.

Finally, the pressure gradients, that was assumed to be very small w.r.t. the

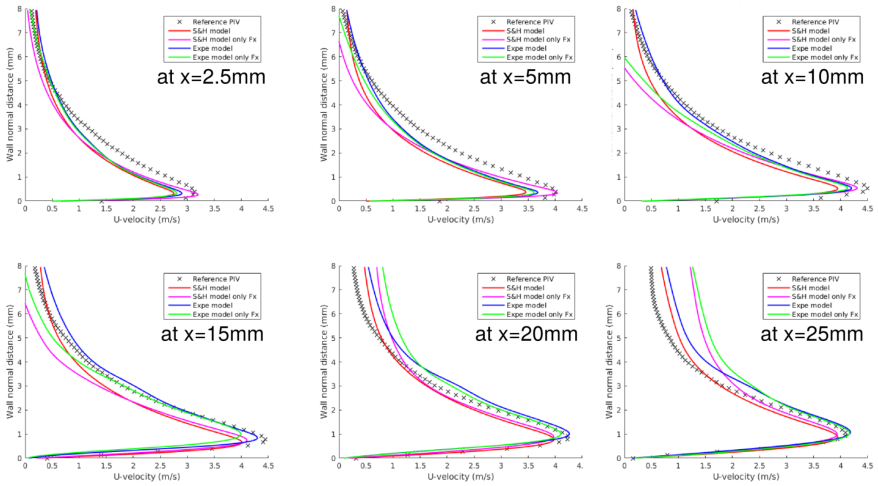

Figure 2.19: Vertical profiles of the dimensional time-averaged streamwise velocity component at 6 different streamwise locations from $x = 2.5\,\text{mm}$ to$x = 25\,\text{mm}$. [5]

components of the model in the experimental reverse Navier-Stokes approach are found to be of the same order as the component of the volume force in the region close to the actuator, showing some unclear phenomena [5].

The spanwise velocity induced by two of the tested plasma actuators is displayed in Fig. 2.19, the velocity w is here shown in dimensional values. In the DNS simulations, the variables are scaled in viscous units to be sure to address the same problem; Benard et al. report a viscous velocity $u_\tau = 0.4\,\text{m}\,\text{s}^{-1}$, so the induced velocity w is therefore scaled on this reported u_τ.

2.3.3 Drag reduction via DBD plasma actuators

Choi et al. in [7] suggested the possibility to use plasma actuators to create alternating spanwise wall jets in the near-wall, in order to reduce the turbulent activity (i.e. sweep and ejections) in the viscous sublayer and buffer layer.

[23] investigated the possibility to achieve skin-friction drag reduction by streamwise-aligned plasma actuators to simulate the oscillating wall proposed by [27]. The present work modelled the 2D body forces distribution produced by the actuators according to three different models: Suzen-Huang05 [35], Suzen-Huang07 and Shyy02 [34]. The actuators are then extended in the streamwise direction in a constant manner, as they are streamwise-aligned. The distribution chosen for the drag reduction investigation was the Suzen-Huang05, as this model better stick with the experimental results in [4]. The idea is to mimic the transverse wall oscillations by using streamwise-aligned pairs of plasma actuators.

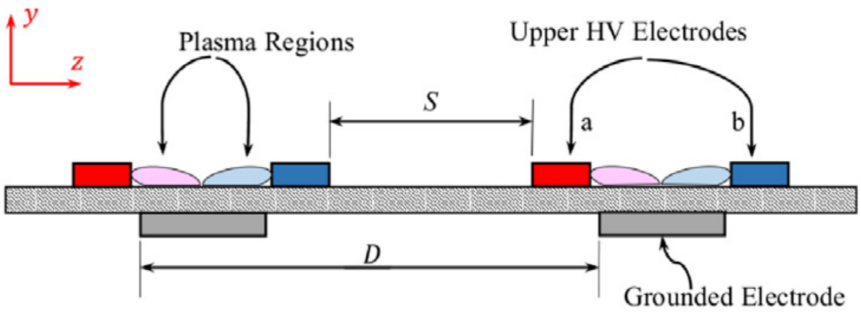

Figure 2.20: Sketch of the cross section of the plasma actuators arrangement, D is δz^+ in the present work. [23]

The actuators are downsized in the numerical simulation to obtain a precise value for $\Delta_H^+ = 10, 20, 40$ (the wall-normal altitude from the wall where the force strength drops to lower than 5% of the maximum) and a maximum induced velocity in viscous units equal to $w^+ = 9.5$ when $\Delta_H^+ = 20$. The third parameter introduced in the work is the oscillation frequency, that consist of the inverse of the on/off period of the red or blue exposed electrode in Fig. 2.20, and that is equal to $T^+ = 16, 100, \infty$. $T^+ = \infty$ is the only value that can achieve positive drag reduction as it is the only that shift upwards the log-layer, left in Fig. 2.21.

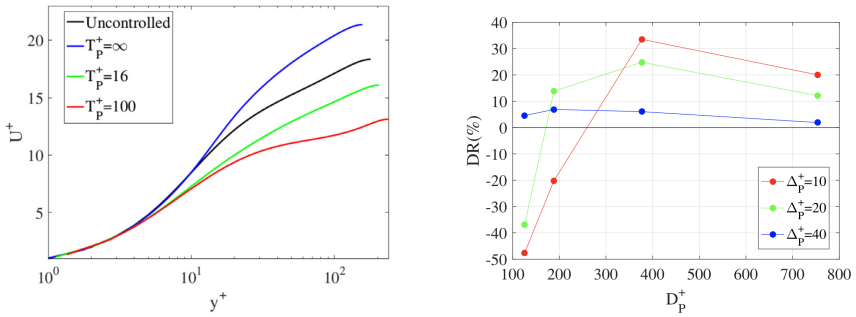

Figure 2.21: Time averaged streamwise velocity profiles (left) obtained for $\delta z^{=}378$, $\Delta_H^+ = 20$ and $T^+ = 16, 100, \infty$. Drag reduction for different spanwise spacing (δz^+) and force height (Δ_H^+) on the right, $T^+ = \infty$. [23]

Right figure clarify that the distance between two pairs of actuators and their scaling with respect to the channel can make a huge difference in obtaining a positive drag reduction or a very bad drag increase. In particular, for $\Delta_H^+ = 10$ one can achieve the best performance, but he gets the most risky scenario; as Δ_H^+ increase as the DR trend become gentler and gentler.

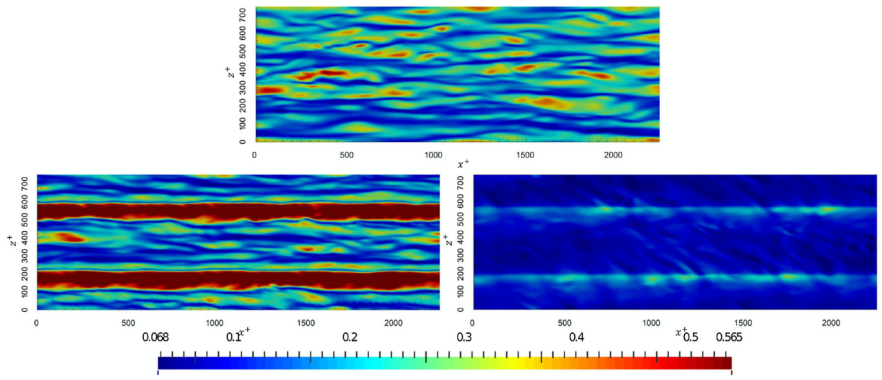

Figure 2.22: Instantaneous streamwise velocity contour in $x-z$ plane at $y^+ = 5$ that shows the streaks of four cases. The colour bar scale is normalized by mean streamwise velocity, and its limits are the maximum and minimum values of the uncontrolled flow. The top frame corresponds to the uncontrolled case, the bottom left frame to the simulation with $R = -75\%$ ($\delta z^{=}376$, $\Delta_H^+ = 10$ and $T^+ = 100$) and the bottom right frame to the simulation with $R = 33\%$ ($\delta z^{=}376$, $\Delta_H^+ = 10$ and $T^+ = \infty$). [23]

Looking at the coherent structures, two possible scenarios can arise: either very intense high-speed streaks are intensified as seen in the bottom left frame of Fig. 2.22 or high-speed events are destroyed as seen in the bottom right frame of Fig. 2.22. In the first situation, the strength of the more intense streaks is amplified and two massive streaks located above the actuators appear, while the rest of the flow is left approximately untouched. In the second case, the high-speed events are decreased in intensity and the skin-friction drag is reduced. These two last mechanisms are of fundamental importance for the present work, as they will constantly appear in Chapter 4.

3. DNS of a plane channel flow

The DNS code used in the current study is developed by Quadrio and Luchini in `CPL` language. The code exploits the simplicity of the current geometry in order to maximize the efficiency and for the parallelization in the wall-normal direction. More information about the code are available in [26].

3.1 iNSEs: Incompressible Navier-Stokes Equations

The model problem of the plane channel flow in this context is usually described by incompressible Navier-Stokes equations (iNSEs); Cartesian coordinates are chosen because of the geometry.

$$\begin{cases} \nabla \cdot \mathbf{u} = 0 & \text{(3.1a)} \\ \dfrac{\partial \mathbf{u}}{\partial t} + (\mathbf{u} \cdot \nabla)\,\mathbf{u} = -\dfrac{\nabla P}{\rho} + \nu \nabla^2 \mathbf{u} & \text{(3.1b)} \end{cases}$$

The equation can be non-dimensionalized by some non-dimensional variables:

$$\tilde{\mathbf{u}} = \frac{\mathbf{u}}{U} \qquad \tilde{t} = \frac{t}{T} \qquad \tilde{\mathbf{x}} = \frac{\mathbf{x}}{L} \tag{3.2}$$

where U, T and L are dimensional quantities characteristic of the problem. The non-dimensional treatment of the equations leads to the comparison of the Reynolds number on the l.h.s.:

$$\begin{cases} \dfrac{\partial \tilde{u}}{\partial \tilde{x}} + \dfrac{\partial \tilde{v}}{\partial \tilde{y}} + \dfrac{\partial \tilde{w}}{\partial \tilde{z}} = 0 & \text{(3.3a)} \\ \dfrac{\partial \tilde{u}}{\partial \tilde{t}} + \tilde{u}\dfrac{\partial \tilde{u}}{\partial \tilde{x}} + \tilde{v}\dfrac{\partial \tilde{u}}{\partial \tilde{y}} + \tilde{w}\dfrac{\partial \tilde{u}}{\partial \tilde{z}} + \dfrac{\partial \tilde{P}}{\partial \tilde{x}} = \dfrac{1}{Re}\nabla^2 \tilde{u} & \text{(3.3b)} \\ \dfrac{\partial \tilde{v}}{\partial \tilde{t}} + \tilde{u}\dfrac{\partial \tilde{v}}{\partial \tilde{x}} + \tilde{v}\dfrac{\partial \tilde{v}}{\partial \tilde{y}} + \tilde{w}\dfrac{\partial \tilde{u}}{\partial \tilde{v}} + \dfrac{\partial \tilde{P}}{\partial \tilde{y}} = \dfrac{1}{Re}\nabla^2 \tilde{v} & \text{(3.3c)} \\ \dfrac{\partial \tilde{w}}{\partial \tilde{t}} + \tilde{u}\dfrac{\partial \tilde{w}}{\partial \tilde{x}} + \tilde{v}\dfrac{\partial \tilde{w}}{\partial \tilde{y}} + \tilde{w}\dfrac{\partial \tilde{w}}{\partial \tilde{z}} + \dfrac{\partial \tilde{P}}{\partial \tilde{z}} = \dfrac{1}{Re}\nabla^2 \tilde{w} & \text{(3.3d)} \end{cases}$$

In the current setup, energy equation decouples and four unknown variable are present: the three component of $\tilde{\mathbf{u}}$ and $\tilde{P}$. Pressure can be thought as a Lagrangian multiplier that enforce incompressibility, so the $\tilde{P}$ variable can be eliminated from the setup by the projection of the present system on a

divergence-free manifold; instead, mass conservation equation (3.3a) is the non-evolutive equation that represent a cinematic constraint, satisfied everywhere at any time in the domain.

Pressure can be recovered later thanks to the Poisson equation using $\tilde{\mathbf{u}}$, obtained by the divergence of the momentum equation (3.1b) and enforcing the continuity (3.1a). The tilde over variables to denote non-dimensional ones is dropped from now on:

$$\nabla^2 \mathbf{P} = -\nabla \cdot (\mathbf{u} \cdot \nabla \mathbf{u}) \tag{3.4}$$

The problem, to be closed, requires initial and boundary conditions; the latter must impose the periodicity of the solution and the no-slip and no-penetration conditions on the walls:

$$\begin{cases} \mathbf{u}(x,y,z,0) = \mathbf{u_0}(x,y,z) & \text{initial condition} \quad (3.5a) \\ \mathbf{u}(x,y,z,t) = 0 \ for \ y = y_{top}, y_{bot} & \text{no-slip/penetration condition} \quad (3.5b) \\ \mathbf{u}(x,y,L_z,t) = \mathbf{u}(x,y,0,t) & \text{spanwise cyclic wall} \quad (3.5c) \\ \mathbf{u}(L_x,y,z,t) = \mathbf{u}(0,y,z,t) & \text{streamwise cyclic wall} \quad (3.5d) \end{cases}$$

3.2 $v - \eta$ Formulation of the iNSEs

The system of equations obtained is composed by the three evolutive momentum equations and by the non-evolutive continuity equations. In order to obtain only evolutive equations it is possible to project the iNSEs on a divergence free manifold, this process eliminate P from the unknown variables and lead to a new system that automatically satisfies the continuity equations. The new equations are not dependent on the primitive variable $\mathbf{u}$ and P, but depends on the wall-normal component of the velocity, v, and the wall-normal component of the vorticity, η. This change of variables comes with a cost; the differential equation for v is a fourth order PDE and the boundary condition are sometimes difficult to be written in the $v - \eta$ formulation.

η is defined, according to the definition of vorticity, as:

$$\eta = \frac{\partial u}{\partial z} - \frac{\partial w}{\partial x} \tag{3.6}$$

The equation for the wall-normal component of the vorticity is easily obtained by taking the $y-$component of the curl ($\nabla\times$) of the wall-normal momentum equation:

$$\frac{\partial \eta}{\partial t} = h_\eta + \frac{1}{Re}\nabla^2 \eta \tag{3.7}$$

$$h_\eta = \frac{\partial}{\partial x}\left(u\frac{\partial w}{\partial x} + v\frac{\partial w}{\partial y} + w\frac{\partial w}{\partial z}\right) - \frac{\partial}{\partial z}\left(u\frac{\partial u}{\partial x} + v\frac{\partial u}{\partial y} + w\frac{\partial u}{\partial z}\right) \tag{3.8}$$

The equation for the wall-normal velocity v is a fourth order PDE and is obtained by taking the laplacian of the $y-$component of the momentum equation and substituting in it the Poisson equation for pressure:

$$\frac{\partial \nabla^2 v}{\partial t} = h_v + \frac{1}{Re}\nabla^2\nabla^2 v \tag{3.9}$$

$$h_v = \frac{\partial}{\partial y}\left[\frac{\partial}{\partial x}\left(u\frac{\partial u}{\partial x} + v\frac{\partial u}{\partial y} + w\frac{\partial u}{\partial z}\right) + \frac{\partial}{\partial z}\left(u\frac{\partial w}{\partial x} + v\frac{\partial w}{\partial y} + w\frac{\partial w}{\partial z}\right)\right] - \\ - \left(\frac{\partial^2}{\partial x^2} + \frac{\partial^2}{\partial z^2}\right)\left(u\frac{\partial v}{\partial x} + v\frac{\partial v}{\partial y} + w\frac{\partial v}{\partial z}\right) \quad (3.10)$$

The solution of the two previous equations, 3.7 and 3.9, allow to obtain the values of the two unknown variables v and η, but the target of the simulation is to recover the primitive variables u, v, w and later P by the Poisson equation. The continuity equation and the definition of η are used to find the value of u and w by this system:

$$\begin{cases} \dfrac{\partial u}{\partial x} + \dfrac{\partial w}{\partial z} = -\dfrac{\partial v}{\partial y} & (3.11a) \\ \dfrac{\partial u}{\partial z} - \dfrac{\partial w}{\partial x} = \eta & (3.11b) \end{cases}$$

3.2.1 Setup of the Plane Channel Flow

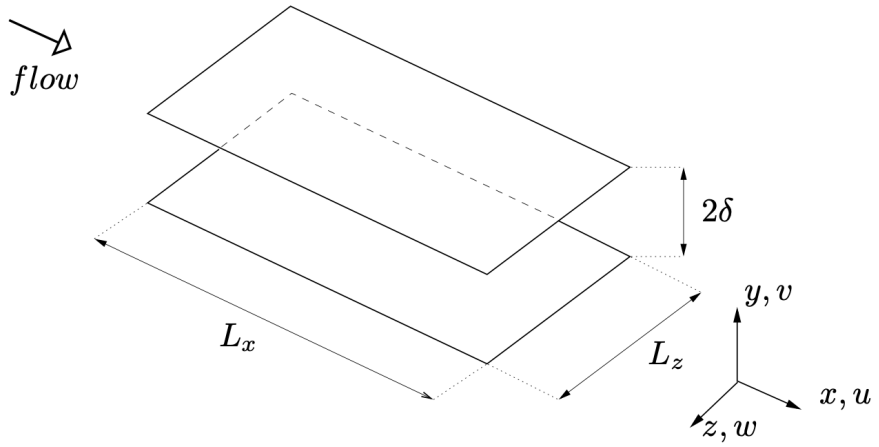

Figure 3.1: Schematic geometry of a plane channel flow. [26]

In the following calculation is simulated a channel flow of semi-height δ equal to unity, the length in the wall-normal direction is therefore two times δ , namely $L_y = 2\delta = 2$.

In the spanwise direction, the zero pressure gradient is set to zero in order to let the flow move freely around a zero mean value; instead, in the streamwise direction, it's usually imposed the mean flow-rate as two times the bulk velocity multiplied by δ. Since the bulk velocity is chosen as reference velocity of the flow, it is set to unity, the mean flow-rate is set equal to two; the centerline velocity comes straightforward from laminar Poiseuille calculations and is $U_c = 3/2U_b = 3/2$.

The Reynolds number Re_b, based on the bulk velocity, is the most natural choice and it results to be the inverse of the kinematic viscosity ν:

$$Re_b = \frac{U_b \delta}{\nu} = \frac{1}{\nu} \quad (3.12)$$

3.2.2 Boundary conditions

As specified in section 3.1, the $v-\eta$ formulation lead to more complex boundary condition; in the present case of a plane channel flow, boundary conditions are well known and understood, but this is not true for in many other cases.

The boundary conditions essentially consist of a no-slip condition on u, w and a no-penetration condition on v, they are written in primitive variables for the flow in question as:

$$\mathbf{u}(x,(0,2),z,t)=0 \tag{3.13}$$

If one translate this condition to the derived variables v and η, he ends up with six scalar equations[1] with the same meaning, but written in a different form:

$$\begin{cases} v(x,(0,2),z,t)=0 & \text{no-penetration condition} \quad (3.14a)\\ \left(\dfrac{\partial v}{\partial y}\Big|_{y=0,2}\right)=0 & \text{no-slip condition 1} \quad (3.14b)\\ \eta(x,(0,2),z,t)=0 & \text{no-slip condition 2} \quad (3.14c) \end{cases}$$

By some basic algebra is possible to demonstrate that the two no-slip condition impose constant and null u and w on the wall if one translates back the b.c. back in the primitive variables.

Either way, the present work use a slightly different setup from this basic one. Since it is inefficient to simulate a complete channel flow with the forcing imposed by the DR technique reflected on both the top and the bottom wall, the simulation deal with only half of the channel. The bottom wall remains in place, while the semi-height of the channel is the new boundary; the new set of boundary condition written in the $v-\eta$ form is:

$$\begin{cases} v(x,0,z,t)=0 & \text{no-penetration condition} \quad (3.15a)\\ \left(\dfrac{\partial v}{\partial y}\Big|_{y=0}\right)=0 & \text{no-slip condition 1} \quad (3.15b)\\ \eta(x,0,z,t)=0 & \text{no-slip condition 2} \quad (3.15c)\\ v(x,1,z,t)=0 & \text{symmetry condition 1} \quad (3.15d)\\ \left(\dfrac{\partial^2 v}{\partial y^2}\Big|_{y=1}\right)=0 & \text{symmetry condition 2} \quad (3.15e)\\ \left(\dfrac{\partial \eta}{\partial y}\Big|_{y=1}\right)=0 & \text{symmetry condition 3} \quad (3.15f) \end{cases}$$

3.3 $v-\eta$ in the Numerical Framework

The iNSEs equation expressed in $v-\eta$ variables are now ready to be discretized, since it is clear that DNS requires enormous computational effort, it is of fundamental importance to maximize computational efficiency without loss of reliability. Streamwise and spanwise directions are homogeneous directions, so it is

[1] It is important to notice that the primitive set of equations was composed by three momentum equations of the second-order, so it was necessary to have 2 b.c. for every equation. The $v-\eta$ formulation is written as two different equations, a fourth order and a second order equations, so it request 6 b.c..

convenient to discretize the variables along this directions using Fourier expansions, wall-normal direction is not treated in the same manner because boundary condition are not periodical and it is useful to use a structured non-uniform grid. Since the problem deals with evolutive equations, time discretization is also necessary to the code.

3.3.1 Fourier Transform

Variables $v(x,y,z,t)$ and $\eta(x,y,z,t)$ are developed in x and z directions using Fourier series expansion; this choice is strictly related to the cyclic boundary conditions, using Fourier series are automatically satisfied, and because x and z are homogeneous directions. The truncated Fourier series expansions lead to:

$$v(x,y,z,t) = \sum_{h=-N_x/2}^{N_x/2} \sum_{l=-N_z/2}^{N_z/2} \hat{v}_{\alpha,\beta}(y,t) e^{i\alpha_0 hx} e^{i\beta_0 hz} \tag{3.16a}$$

$$\eta(x,y,z,t) = \sum_{h=-N_x/2}^{N_x/2} \sum_{l=-N_z/2}^{N_z/2} \hat{\eta}_{\alpha,\beta}(y,t) e^{i\alpha_0 hx} e^{i\beta_0 hz} \tag{3.16b}$$

where α_0 and β_0 are the fundamentals wavenumbers and are defined as $\alpha_0 = \frac{2\pi}{L_x}$ and $\beta_0 = \frac{2\pi}{L_z}$, N_x and N_z are the number of wavenumber present in the truncated Fourier series.

It is needed to introduce some notation for the following procedures; $k^2 = \alpha^2 + \beta^2$ is the square modulus of the 2D vector of the wavenumbers, while the notation $D_n(\cdot)$ is the n-th order derivative along wall-normal direction. The Fourier expansions allow to substitute derivatives in homogeneous directions with algebraic multiplication by an algebraic coefficient, the convective terms are defined as:

$$\widehat{HU} = j\alpha\hat{u}\hat{u} + D_1(\hat{u}\hat{v}) + j\beta\hat{u}\hat{w} \tag{3.17a}$$

$$\widehat{HV} = j\alpha\hat{u}\hat{v} + D_1(\hat{v}\hat{v}) + j\beta\hat{v}\hat{w} \tag{3.17b}$$

$$\widehat{HW} = j\alpha\hat{u}\hat{w} + D_1(\hat{w}\hat{v}) + j\beta\hat{w}\hat{w} \tag{3.17c}$$

Wall-normal vorticity equation 3.7 reads:

$$\frac{\partial\hat{\eta}}{\partial t} = \frac{1}{Re}\left[D_2\left(\hat{\eta} - k^2\eta\right)\right] + j\beta\widehat{HU} - j\alpha\widehat{HW} \tag{3.18}$$

Wall-normal velocity equation 3.9 becomes:

$$\frac{\partial}{\partial t}\left[D_2(\hat{v}) - k^2\hat{v}\right] = \frac{1}{Re}\left[D_4(\hat{v}) - 2k^2 D_2(\hat{v}) + k^4\hat{v}\right] - k^2\widehat{HV} - D_1\left(j\alpha\widehat{HU} + j\beta\widehat{HW}\right) \tag{3.19}$$

Equations 3.18 and 3.19 are decoupled if the nonlinear convective terms are known, it is therefore logical to treat these terms in an explicit manner in the time discretization procedure; this comes at a cost, the method will be conditionally stable and must be respectful towards a CFL condition. This means that nonlinear terms are computed in advance and then inserted in the known vector, anyway this procedure requires to know u and w for each couple of wavenumbers α, β, by solving a 2x2 algebraic system. This latter is singular when $k^2 = 0$; a space plane-average operator is used to recover value of u and w when $k^2 = 0$.

3.3.2 Evaluation of the Nonlinear Convective Terms

Evolutive equations for v and η contains multiplications between terms that in the code are discretized via Fourier series. The operation of multiplication come at very small cost in the physical domain, but the problem arises when the same operation is performed in the Fourier domain: the multiplication in Fourier domain has a cost of N^2 floating point operations.

As a consequence, the quantities of interest are inverse transformed (IFT) in the physical domain at $NlogN$ cost, the 6 multiplication to obtain uu, uv, uw, vv, vw and ww are performed and then transformed back into wavenumber space using a Fast Fourier Transform (FFT) library[2] at $NlogN$ cost.

In the present case the 3/2 zero padding is used for de-aliasing. According to the rule, it is necessary to expand the number of collocation points before the first IFT procedure is done, so that the aliased contributions fall in the 1/2 part "in excess", the multiplication is performed and the new quantities are transformed back in Fourier domain and truncated to the original size.

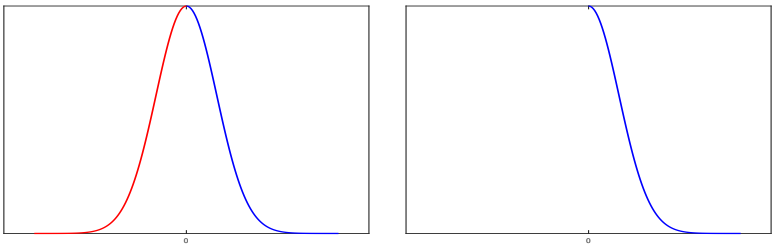

Figure 3.2: Respectively the value storage in the non-Hermitian and Hermitian direction.

3.3.3 Time and space discretization

Equations for v (3.19) and η (3.18) are evolutive equations, so they need to be numerically integrated in time; the time advancement use a semi-implicit scheme since some of the terms must be treated as explicit. The viscous part is treated with an implicit scheme (second order Crank-Nicholson) to relieve the constraint on Δt, that will be limited only by the explicit part. The explicit part, i.e. the nonlinear terms, use a third-order Runge-Kutta that provides higher precision. Anyway, both the explicit and the implicit methods can be changed without affecting the structure of the code, thanks to different modules that can swap each other.

[2]The FFT library coded in `CPL` perform in-place Fourier transform and take advantage of the Hermitian symmetry in case the physical quantities are real. The Hermitian symmetry allow to use half of the original matrix in one direction to save memory and computational cost; if the starting complex matrix in physical domain is a $N \times N \times N$ containing only real values, the stored complex matrix in Fourier domain is $N/2 \times N \times N$.

$$\begin{aligned}\frac{\lambda}{\Delta t}\hat{\eta}_{hl}^{n+1} - \frac{1}{Re}\left[D_2\left(\hat{\eta}_{hl}^{n+1}\right) - k^2\hat{\eta}_{hl}^{n+1}\right] = \\ = \frac{\lambda}{\Delta t}\hat{\eta}_{hl}^{n} - \frac{1}{Re}\left[D_2\left(\hat{\eta}_{hl}^{n}\right) - k^2\hat{\eta}_{hl}^{n}\right] + \\ + \theta\left(i\beta_0 l\widehat{HU}_{hl} - i\alpha_0 h\widehat{HW}_{hl}\right)^n + \xi\theta\left(i\beta_0 l\widehat{HU}_{hl} - i\alpha_0 h\widehat{HW}_{hl}\right)^{n-1}\end{aligned} \tag{3.20}$$

$$\begin{aligned}\frac{\lambda}{\Delta t}\left(D_2\left(\hat{v}_{hl}^{n+1}\right) - k^2\hat{v}_{hl}^{n+1}\right) - \frac{1}{Re}\left[D_4\left(\hat{v}_{hl}^{n+1}\right) - 2k^2 D_2\left(\hat{v}_{hl}^{n+1}\right) + k^4\hat{\eta}_{hl}^{n+1}\right] = \\ = \frac{\lambda}{\Delta t}\left(D_2\left(\hat{v}_{hl}^{n}\right) - k^2\hat{v}_{hl}^{n}\right) - \frac{1}{Re}\left[D_4\left(\hat{v}_{hl}^{n}\right) - 2k^2 D_2\left(\hat{v}_{hl}^{n}\right) + k^4\hat{\eta}_{hl}^{n}\right] + \\ + \theta\left(-k^2\widehat{HV}_{hl} - D_1\left(i\alpha_0 h\widehat{HU}_{hl} + i\beta_0 l\widehat{HW}_{hl}\right)\right)^n + \\ + \xi\left(-k^2\widehat{HV}_{hl} - D_1\left(i\alpha_0 h\widehat{HU}_{hl} + i\beta_0 l\widehat{HW}_{hl}\right)\right)^{n-1}\end{aligned} \tag{3.21}$$

where the three coefficients λ, θ and ξ define the chosen time-advancement scheme.

As first step, the RHSs (right hand sides) of the explicit terms are assembled; this step requires also wall-normal derivatives, obtained by compact schemes, that request to use RHSs values from the previous time step. Next, for each pair of α, β, the code solves a set of two ODEs, for which the RHS is now known. In the $\alpha-\beta-y$ space the first step of this procedure proceeds per wall-parallel planes, while the second one proceeds per wall-normal lines.

About the spatial discretization, the equations require the discretization of the first, second and fourth wall-normal derivatives D_1, D_2 and D_4, here obtained by finite-differences compact schemes. According to [21], the computational molecule is composed of five arbitrarily spaced (with smooth stretching) grid points on a mesh of n_y+1 points y_j, with $0 \leq j \leq n_y$. $d_n^j(i)$, $i=-2,...,2$ are the five coefficients discretizing the exact operator D_n over five adjacent grid points centered at y_j; they must be computed for the whole $y-$range but only once in the entire computation.

Boundary condition in equation 3.14 are translated in the discretized code as following for the complete channel:

$$\begin{cases} d_0^j\hat{v}_{hl} = 0 & \text{no-penetration condition} \quad (3.22a) \\ d_1^j\hat{v}_{hl} = 0 & \text{no-slip condition 1} \quad (3.22b) \\ d_0^j\hat{\eta}_{hl} = 0 & \text{no-slip condition 2} \quad (3.22c) \end{cases}$$

where j is equal to zero for the bottom wall and equal to n_y for the top wall.

If one decides to simulate half channel, the discretized boundary conditions on the top boundary become:

$$\begin{cases} d_0^j\hat{v}_{hl} = 0 & \text{symmetry condition 1} \quad (3.23a) \\ d_2^j\hat{v}_{hl} = 0 & \text{symmetry condition 2} \quad (3.23b) \\ d_1^j\hat{\eta}_{hl} = 0 & \text{symmetry condition 3} \quad (3.23c) \end{cases}$$

where j is equal to n_y, since these conditions are applied on the top boundary only.

In the numerical simulations, the time step Δt is not free to be chosen, indeed the time integration scheme, as presented above, is only conditionally stable. At each time step, Δt is computed following the CFL condition:

$$\Delta t = \frac{\max\limits_{\Omega}(CFL)}{\max\limits_{\Omega}\left(\frac{u}{\Delta x}\right) + \max\limits_{\Omega}\left(\frac{v}{\Delta y}\right) + \max\limits_{\Omega}\left(\frac{w}{\Delta z}\right)} \tag{3.24}$$

in the whole computational domain Ω.

3.3.4 Body forces

The code is integrated with some interpolation `.cpl` scripts that allows to include body forces, here indicated as $\mathbf{b}$. The interpolators can deal with basically any `.dat`, `.txt` or similar extension files that contain the measurements of the three force components and the respective location. Further details are present in appendix A.

Data from real experiments or dimensional simulations need to be non-dimensionalized in order to stick with the nature of code; for example, coordinates that represent the location should be referred to the unitary semi-height of the channel δ. Once that initial data are adjusted, the dedicated 3D linear interpolator provides to adapt the initial array size to the one that will be used in the current DNS simulation.

Once the array size of $\mathbf{b}$ is compatible with the discretized $v-\eta$ equations, body force vector is transformed plane by plane in Fourier domain along streamwise and spanwise directions following the same procedure present in 3.3.2, then stored exploiting the Hermitian symmetry.

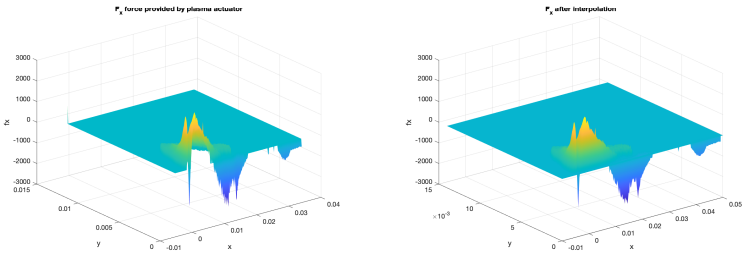

Figure 3.3: Respectively the original input data on a specific plane $z-y$ provided by experiments. Before the interpolation (left) and after (right). Original data does not start from $y = 0$ for experimental reasons.

In principle, the body force term should be multiplied by a non-dimensional coefficient, that contains a Froude-like number, to be inserted in the non-dimensional equations. The present non-dimensional coefficient, after some basic algebra, result to be:

$$\frac{1}{\tilde{Fr}^2} \tag{3.25}$$

where $\tilde{Fr}$ is the Froude-like number based on a characteristic acceleration and not on the gravity acceleration like the original Fr. It is therefore defines as:

$$\tilde{Fr} = \frac{u}{\sqrt{aL}} \tag{3.26}$$

with u, a and L as, respectively, the reference velocity, acceleration and length.

3.4 Validation of the DNS code

For the sake of efficiency, the simulations are performed on a semi-channel: L_y span from zero to unity, L_x and L_z are unchanged. Indeed, the presence of body forces on the bottom wall would have resulted in the introduction of the same mirrored force on the top wall if considering an entire channel, with no practical advantage and an increase in computational costs.

The setup of the simulations is chosen to stick with the most reproduced simulation in DNS history, the MKM180 DNS at $Re_\tau = 180$ described in [15] by Kim et al. Two different validation simulations are run, based on two different choice of the Reynolds number:

- $Re_\tau = 180$ and unit **meanpx**, the **meanp** forcing is related to the non-dimensional factor in pressure gradient.
- $Re_b = 2800$ and unit **meanflowx**, the **meanflow** is used as forcing, over **meanp**, because of the choice to use a Reynolds number based on the bulk velocity U_b; it is a natural consequence to impose the flow rate as the unitary reference velocity U_b multiplied by the unitary height of the semi-channel.

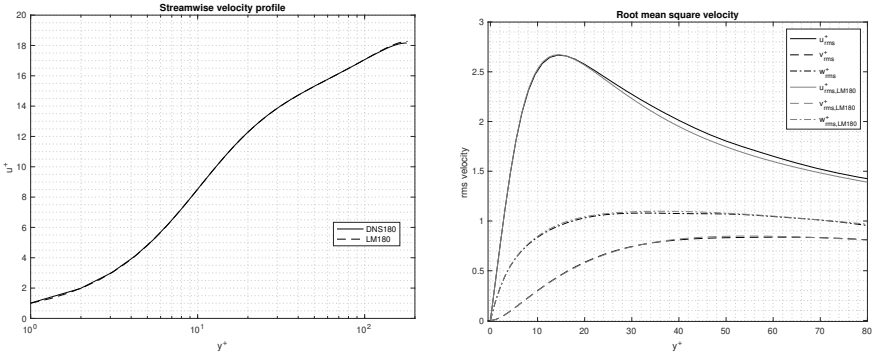

Figure 3.4: Respectively, the mean velocity $\overline{u^+}$ and r.m.s. velocity profiles comparison between validation simulation (DNS180) and MKM180 simulation. [15]

A computational box of dimensions $L_x = 4\pi$, $L_z = 2\pi$ in the streamwise and spanwise direction respectively, has been used to perform the simulation; the velocity is initialized as a laminar flow with same flow rate and CFL condition is set to always stay below unity during the whole simulation. The grid is discretized with $64 \times 60 \times 64$ ($N_x \times N_y \times N_z$); the spatial discretization in wall

unit result to be $\Delta x^+ = 34$, $\Delta z^+ = 17$, while, in the wall normal direction the first grid point from the wall is placed at $\Delta y^+ = 0.96$ up to $\Delta y^+ = 6$ at the centerline.

Fig. 3.4 shows a good agreement between the statistics of the first DNS180, based on $Re_\tau = 180$, and the reference calculation. The resolution of the current simulations is way smaller with respect to MKM180 for obvious reasons; DNS180 runs on a laptop machine equipped with an Intel i7-4510U processor and the time available for the validation simulation is limited.

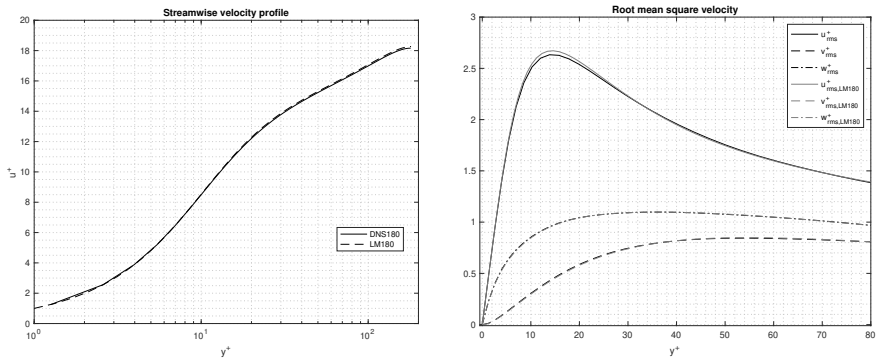

Figure 3.5: Respectively, the mean velocity $\overline{u^+}$ and r.m.s. velocity profiles comparison between validation simulation (DNS180) and MKM180 simulation. [15]

Same arguments repeat for the second DNS180 simulation, based on $Re_b = 2800$, in Fig. 3.5.

3.5 Setup of the core study

While the validation and preliminary simulations run on a lighter setup, as it described in the respective sections, to save time and to detect possible criticality in a faster manner, the core part of the study exploits a more heavy and precise setup. The whole package of simulations simulate a plane semi-channel flow driven by a positive unit pressure gradient `CPG` along the streamwise direction: **meanpx**= 1. Using `CPG` allows to directly impose Re_τ as an input parameter, so $Re_\tau = 200$ for all the simulations. The viscous Reynolds number, $Re_\tau = 200$, is a trade-off between the computational time and the desire to push the Reynolds number as high as possible, with the aim of stick as close as possible with a value typical of a real world application. For the sake of saving a considerable amount of resources, the choice of $Re_\tau = 180$ was also taken in consideration. Considering the risk of relaminarization in case good DR performances, that is far from a possible real-world application, were achieved by some kind of forcing, $Re_\tau = 180$ is left out.

A computational box of dimensions $L_x = 4\pi$, $L_z = 4\pi$ in the streamwise and spanwise directions respectively has been used for the core part of the study, the spanwise length has been double in order to provide the enough spacing in cases with $N_{act} = 1$ and $N_{act} = 2$, since no leads were available from previous studies. According to [11], the streamwise length is surely bigger than

the minimal domain to be capable of sustaining the near-wall turbulent cycle. $L_x = 4\pi$, at $Re_\tau = 200$, is also big enough to prevent the error due to large structures that are responsible to deviate the velocity profile to the correct one; this problem becomes more serious for an increasing Reynolds number. The wall-normal height is set to unit because of the semi-channel setup, thanks to the modified boundary condition on the top boundary.

The discretization parameters are chosen in order to comply with the presence of multiple actuators along the spanwise direction; so, $N_x \times N_y \times N_z$ are respectively[3] set equal to $85 \times 150 \times 170$. The choice of $N_z = 170$ is the best possible taking in consideration the lack of computational resources in this specific period; since the simulation with the highest number of actuators is $N_{act} = 50$, an higher value of N_z should provide a more precise discretization. Wall-normal coordinates can't be equally spaced. The near-wall region requires more points in $y-$direction because the cell size must be comparable with the characteristic viscous length δ_ν. A stretching function is required:

$$y_i = y_{min} + \frac{1}{2}\left(y_{max} - y_{min}\right)\frac{\tanh\left(a\left(\frac{2i}{n_y} - 1\right)\right)}{\tanh\left(a\right)} + \frac{1}{2}\left(y_{max} - y_{min}\right) \qquad (3.27)$$

where a is a parameter larger than one ($a \approx 1.4 - 1.6$) that modify the spacing. In the present setup, $y-$coordinates span from 0 to 1, or $y^+ = 0 - 200$, and the vertical parameter is chosen as $\alpha = 1.6$ in order to better discretize the body forces distribution located very close to the bottom wall.

The resulting discretization leads to $\Delta x^+ \approx 30$, $\Delta z^+ \approx 15$ and $\Delta y^+ \approx 0.35-2.5$; if the anti-aliasing nodes are taken in consideration, Δx^+ and Δz^+ are reduced by a factor $\frac{3}{2}$. The time-step advance is obtained by the CFL condition, that is computed at each time-step according to Eq.3.24, and bounded to stay equal or lower than unit in the whole domain.

The initial condition on the velocity is imposed equal to a fully developed uncontrolled turbulent flow[4]; after the introduction of the forcing (either the spanwise velocity on the wall or the body forces), an initial transient leads the flow to a reduced or increased friction drag, depending on the sign and the value of $R[\%]$. The statistical analysis completely discards this transitory to prevent the results to be affected by side effects; the usage of a larger time to compute statistics provides a smaller uncertainty related to the value of $R[\%]$ and the other quantities.

3.5.1 Computational resources

Since no computational resources from CINECA were available in due time, the DNS simulations have been performed on both a rented remote machine (Virtual Private Server or VPS) located in Germany and on three laptops.

The VPS used in the current work is basically equipped with $8 + 6 = 14$ virtual cores, $16 + 32 = 48$ GB of RAM and enough storage space. Two out of

[3]Since streamwise and spanwise directions are Fourier transformed, it is convenient to chose the dimension of the wavenumber vector as the product of a power of two and a single factor of three, taking in consideration the 3/2 zero padding rule. In this case, $x-$direction: $(85 + 1) \cdot \frac{3}{2} = 129$.

[4]This first simulation is initialized with the Poiseuille solution of a laminar flow to satisfy initial condition constraints.

three laptops are equipped with Intel i5 CPUs and the last features an old-gen Intel i7 CPU, each one with 2 physical cores; all the previously cited machines run on Debian 10 Linux OS. The remote machine is controlled via `SSH` protocol to remotely trigger commands on terminal and the `scp` command is used to exchange files between local and remote machines.

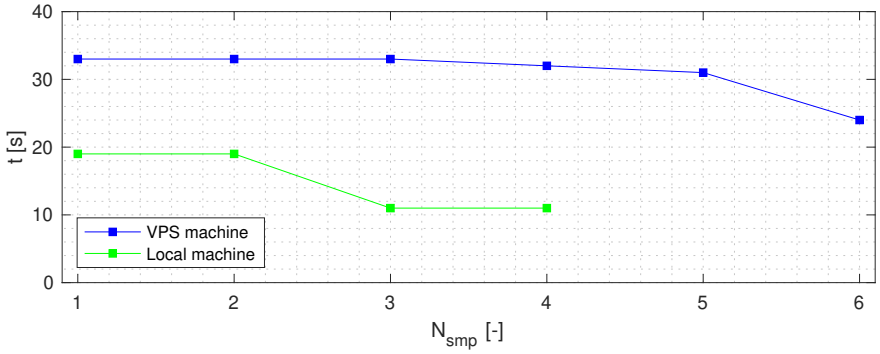

Figure 3.6: Time required to complete a single time-step vs. the number of simultaneous processes. The VPS does not show any relevant benefit in parallelization because each different core is localized on a random node of a huge server. The local machines feature only two physical cores, that are four logical cores thanks to hyper-threading; since it works on Linux OS, only physical cores are relevant for the present work.

Each simulation runs on a single core and takes about 50.000 time steps[5] to obtain about five viscous time units to compute averages after the initial transient. Since the architecture of the VPS is not known and the calculations does not show any relevant benefit from parallel computing, each simulation run on a single virtual core for about a month. A small part of the simulations, the one with positive DR or severe DI, required an extra time for the computations and are run on the local machines, in order to speed up the process.

[5]Each simulation is initialized from a fully developed turbulent channel flow at $Re_\tau = 200$. The number of time steps specified does not consider the first simulation with no forcing.

4. DNS simulations

This chapter describes the structure of the work and it present the corresponding results for each different case considered. The simulations are performed using the DNS code described at high level in chapter 3; low-level details and a bit of the coding effort spent for the present work are explained in the appendix A.

4.1 Structure of the work

The whole work is preceded by a preliminary study to determine the optimal amplitude A^+ of the induced velocity in the actual framework.

Once A^+ is decided, the DNS study stick to the following scheme:

1. **DNS simulations with idealized wall velocity boundary conditions**

   The spanwise forcing is directly imposed as velocity boundary condition on the wall, body forces are set to zero. This first step deal with a continuous case (1.a), used to compute the reference DR achievable with the chosen parameters, and with a discontinuous case (1.b) that aims to identify the effect of discretization with this firs rough model.

2. **DNS simulations with modelled body forces**

   The spanwise forcing is now introduced by modelled body forces; the model chosen in the current study is the well known Suzen-Huang model for DBD plasma actuators [35]. As the first step, this second step includes two different subset (2.a and 2.b) to identify the optimal discretization parameters.

3. **DNS with computed distribution of body forces**

   The spanwise forcing is computed by Professor Hiroyuki Nishida from TUAT University of Tokyo; body forces are numerically obtained by a 3D solver and the amplitude is then rescaled to match the induced velocity condition. As the previous steps, this second step includes two different subset (3.a and 3.b).

Table 4.1: Overview of the simulations in the present work.

Case	Type	$N_{simulations}$	Re_τ	$L_x \times L_y \times L_z$	$N_x \times N_y \times N_z$
0.Preliminary Study	CPG	10	200	$4\pi\delta \times \delta \times 2\pi\delta$	$48 \times 60 \times 48$
1. Wall B.C.	CPG	7	200	$4\pi\delta \times \delta \times 4\pi\delta$	$85 \times 150 \times 170$
2. Suzen-Huang B.F.	CPG	8	200	$4\pi\delta \times \delta \times 4\pi\delta$	$85 \times 150 \times 170$
3. Computed B.F.	CPG	8	200	$4\pi\delta \times \delta \times 4\pi\delta$	$85 \times 150 \times 170$

4.2 Preliminary study

This preliminary study aims to build a dataset that will be useful to determine the optimal induced speed w^+ for the core part of the study.

The preliminary experiments performed by Benard et al. from a series of parallel actuators, as previously shown in figure 2.16, lead to a velocity field that is not constant ad continuous in the spanwise direction. Figure 4.1 shows an uneven induced field in the spanwise direction obtained with no streamwise flow; the body forces produced by the actuators are able to reach a negative and positive velocity of about $4.5\,\mathrm{m\,s^{-1}}$ when the sine reaches his maximum value.

In order to avoid, in this first instance, the problems due to discretization and because of the uncertainties present in this first set of experiments, the results here proposed are obtained by a set of DNS simulations performed with body forces that are ideal in a certain sense. Body forces vector $\mathbf{b}$ is averaged in the spanwise direction so it result to be constant along z, along the wall-normal direction the forcing is not manipulated in any sense and along the streamwise direction is modulated as sinusoid:

$$\mathbf{b}(x, y, z) = \mathbf{b}(x, y) = \tilde{\mathbf{b}}(y) \sin(\kappa_x x) \tag{4.1}$$

The idea is to have a continuous and constant forcing in the $z-$direction to replicate a uniform forcing produced by ideal actuators. The wavenumber is set to $\kappa_x = 2$; this choice comes from figure 2.13 and from the fact that the DR function $R(\lambda_x)$ is quite flat in viscous unit around $\lambda_x^+ = 1000$.

Table 4.2: Values of Re_τ, Re_b, number of actuators N_{act}, induced velocity w^+, drag reduction R and its uncertainty δR for simulation within the Preliminary study (case 0).

Re_τ	Re_b	w^+	$R[\%]$	$\delta R[\%]$
200	3171	2.1	5.2	0.98
200	3221	2.8	8.5	0.94
200	3265	3.5	10.5	0.93
200	3319	4.6	15.2	0.90
200	3345	5.0	15.8	0.90
200	3325	5.4	13.7	0.89
200	3280	6.0	14.1	0.89
200	3197	8.0	6.7	0.90
200	3047	9.3	-1.6	1.05
200	2921	11.1	-21.7	1.27

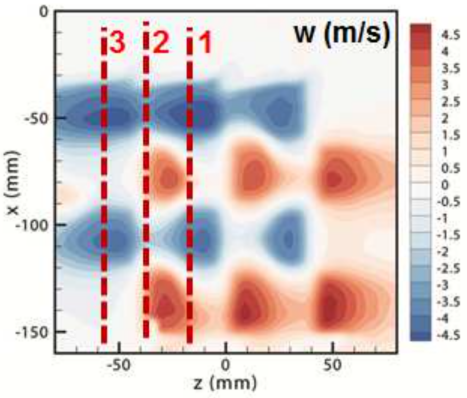

Figure 4.1: PIV measurements of the flow produced by the actuator for the actuator design with an inter-electrode gap of 5 mm. Picture from Professor Nicolas Benard.

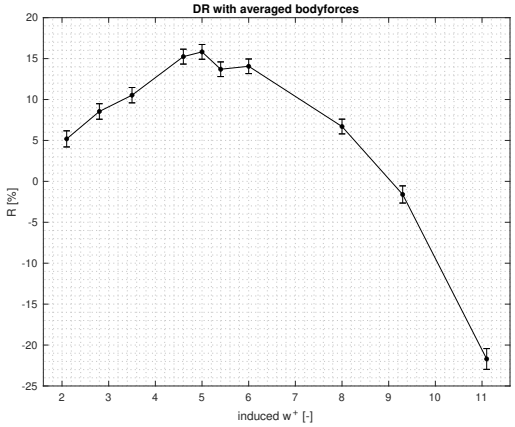

Figure 4.2: $R[\%]$ vs w^+. $Re_\tau = 200$, R peaks at 15.8 for $w^+ \approx 5$. Error bars at 95% Confidence level.

This preliminary study exploit a light setup to smoothly run on a laptop in a reasonable amount of time; $L_x = 4\pi$, $L_z = 2\pi$ in the streamwise and spanwise direction respectively. The grid is discretized with $48 \times 60 \times 48$ ($N_x \times N_y \times N_z$) elements. The non-dimensionalization is based on the viscous Reynolds number $Re_\tau = 200$. The results are summarized in table 4.2.

The value of w^+ is finally chosen from figure 4.2 and set to $A^+ = 4$, also taking into account the existence of similar studies [11] as a benchmark for the whole work. The choice of such a small amplitude has been done taking in consideration that it can be risky because of the reduction of the dynamics of the problem.

4.3 Case 1: DNS simulations with idealized wall velocity boundary conditions

The first step consist of reproducing the stationary spanwise forcing by the direct imposition of moving wall boundary conditions. This simple model of considering the effect of discretization carries some problems that can be solved only by using a more complex and effective model, as will be discussed in the case 2 and case 3.

The boundary conditions are imposed on the wall through stripes of spanwise velocity at $y = 0$ and modulated with a sine in the streamwise direction:

$$\begin{cases} u(x, y = 0, z) = 0 & \text{no-slip} \\ v(x, y = 0, z) = 0 & \text{no penetration} \\ w(x, y = 0, z) = f(z) \cdot A^{+} \sin \kappa_x x & \text{stationary spanwise moving wall} \end{cases}$$

(4.2a)

(4.2b)

(4.2c)

where $f(z)$ is a very simple function that turn `on` and `off` the boundary condition for certain spanwise regions of the wall. Function $f(z)$ depends on the number of actuators that the simulation tries to mimic and geometrical parameters such as the spanwise width of the velocity boundary condition, Δz_{on}, and the spanwise region where the condition is turned `off`, Δz_{off}. It is worth considering that the only wall-normal scale present in this setup is the one related to the viscous length, namely δ_ν. There is no vertical scale strictly related to the actuators, since the boundary condition is imposed in 2D at $y = 0$, so the two geometrical parameters, Δz_{on} and Δz_{off}, are chosen to be tied together by the following relation:

$$\Delta z_{on} = C \cdot \Delta z_{off} \tag{4.3}$$

with $C = 3$ from experimental data.

The choice of streamwise wavenumber, namely κ_x, should be related to experimental data from Poitiers University. Since experiments in Poitiers ran late for the present work, the choice of κ_x comes from the form of the function $R = R(\lambda_x)$. For stationary waves, this function is quite flat and reaches the maximum around $\lambda_x^+ \approx 1000$ [11]; the wavenumber is chosen to be $\kappa_x = 2$.

An example of the previously cited boundary condition is shown in Fig. 4.3.

Theoretically, every time the boundary condition is interrupted, an infinite velocity gradient $\frac{\partial w}{\partial z}$ generates on the discontinuity; in practice the gradient will be very high but not infinite for numerical reasons. For instance, if one hypothesizes to pass from an `off` region to an `on` region, the spanwise velocity derivative with respect to z is positive and very large in absolute value. Hence recalling the continuity equation, it is possible to determine that the sum of u derivative and y derivative in the respective directions is negative:

$$\frac{\partial}{\partial x} u + \frac{\partial}{\partial y} v \ll 0 \tag{4.4}$$

Considering the no-penetration boundary condition on v and the continuity, the wall-normal derivatives is forced to stay positive near the wall or close to

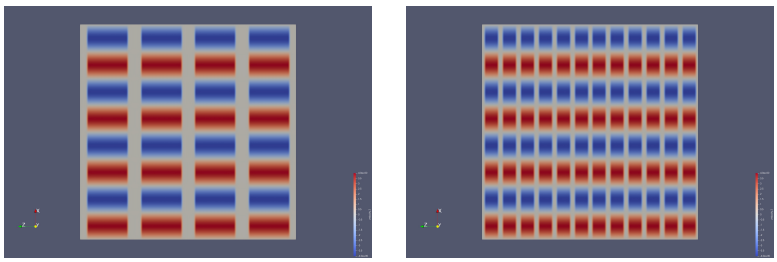

Figure 4.3: Two examples of the wall boundary conditions. Respectively the spanwise velocity boundary condition to mimic $N_{act} = 4$ and $N_{act} = 12$ number of actuators. $x - z$ plane at $y = 0$.

zero. As a consequence:

$$\frac{\partial}{\partial x} u \ll 0 \tag{4.5}$$

This mechanism is responsible to generate a slow speed region in the region close to the discontinuity. Figure 4.4, clears every doubt about this phenomenon.

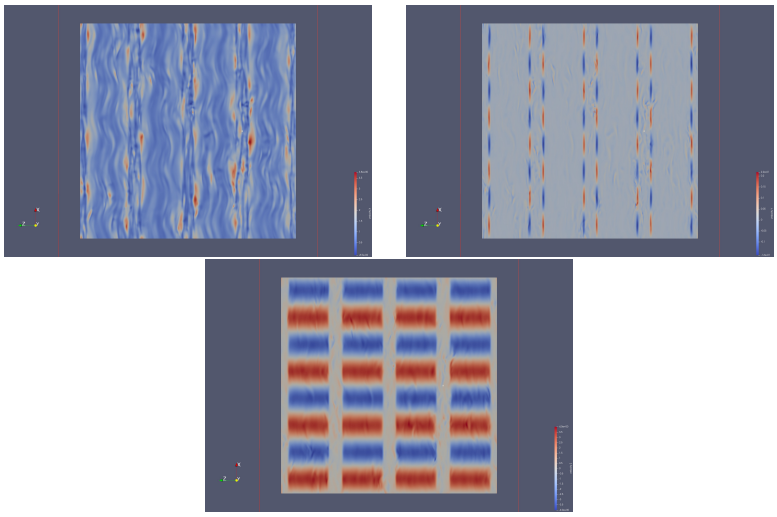

Figure 4.4: Respectively the three velocity components, (u, v, w), for $N_{act} = 4$ simulation at $Re_\tau = 200$. $x - z$ plane at $y = 0.005$, or $y^+ = 1$.

Passing from the `off` region to the `on` region, the flow develops a vertical ejection of fluid if the sine assume a positive value and so $\frac{\partial w}{\partial z} > 0$; if the sine assume a negative value, $\frac{\partial w}{\partial z} < 0$, the fluid produces a sweep. In the opposite case, the transition from `on` to `off`, the fluid show exactly the opposite behaviour, as expected.

The first figure, about the streamwise component x, also show some recognizable areas in the same location as the other two figures; four thick stripes with a quite even flow field and with no relevant irregularities are clearly separated by four thinner stripes characterized by a lower speed streaks and some isolated events of high streamwise velocity. Along the thinner stripes, where the

sinusoidal boundary condition is interrupted, the streamwise velocity also assume slightly negative values (deep blue) close to high-speed region (red). This phenomenon becomes more and more relevant with the number of actuators present in each simulation, like in Fig. 4.5.

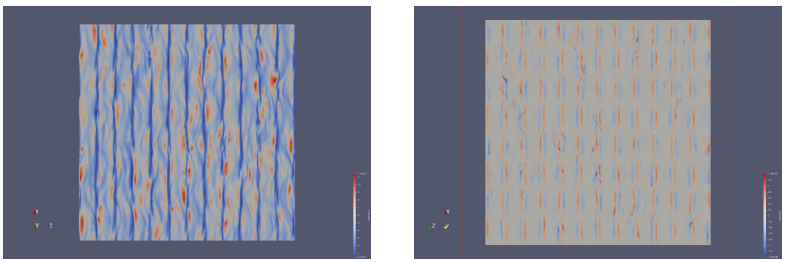

Figure 4.5: Streamwise instant velocity field, u, for $N_{act} = 12$ simulation at $Re_\tau = 200$. $x - z$ plane at $y = 0.025$, or $y^+ = 5$.

The consequences of the present mechanism are quite difficult to understand. The fast streamwise smooth regions, above the `on` areas, indicate a bad performance if one intend to achieve DR; indeed, they tends to lower the height of the viscous sublayer, causing the log-layer to shift downwards. In addition, these "fast" regions are flanked by the "slow" stripes, creating a shear that dissipate energy and possibly introduce additional instability in the flow.

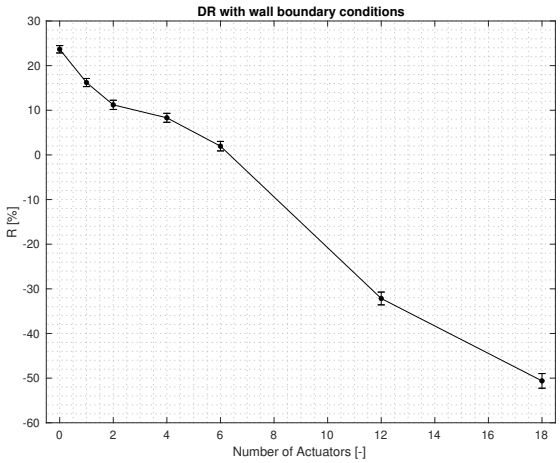

Figure 4.6: $R[\%]$ vs N_{act}. $Re_\tau = 200$, $N_{act} = 0$ stands for the continuous case with no interruptions. Error bars at 95% Confidence level.

The continuous case, $N_{act} = 0$, is used as a reference for the whole work and following cases; the results obtained in this case is in strong agreement with the one obtained in [11]. The results are summarized in table 4.3.

Figure 4.6 shows a very clear trend. According to the model used in this first case to approximate the discretization, a great number of actuators is deleterious for the main goal to obtain a positive DR. Using less and bigger actuators is closer to ideal condition of continuous boundary condition imposed on the wall;

Table 4.3: Values of Re_τ, Re_b, the number of actuators N_{act}, the drag reduction R, its uncertainty δR and ΔB for simulation with wall boundary conditions (case 1).

Re_τ	Re_b	N_{act}	$R[\%]$	$\delta R[\%]$	ΔB
200	3580	-	23.6	0.824	2.27
200	3436	1	16.2	0.911	1.45
200	3398	2	11.2	1.03	0.962
200	3283	4	8.3	0.999	0.696
200	3199	6	1.9	1.06	0.156
200	2765	12	-32.1	1.43	-2.04
200	2589	18	-50.6	1.64	-2.90

every time the boundary condition is interrupted, a new disturb like the one described in Fig. 4.4 is introduced.

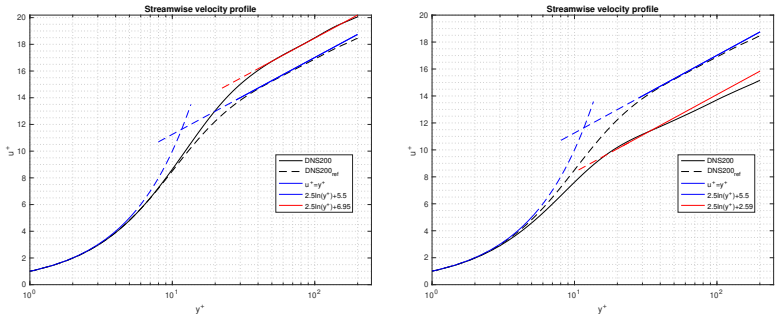

Figure 4.7: Mean velocity profile ($\overline{u^+}$ vs. y^+) comparison between the reference simulation with no forcing (DNS200_{ref}) and a positive DR simulation (left, $N_{act} = 1$, $R = 16.2\%$) or a negative DR simulation (right, $N_{act} = 18$, $R = -50.62\%$). $Re_\tau = 200$. Right figure does not display a perfect superposition of the red and the black solid lines probably because of uncertainty due to the high drag increase.

The shift of the logarithmic region of the mean velocity profile is strictly related to the performance of the DR technique. In analogy with other techniques that are applied on the wall, a vertical upwards shift means a good performance of the forcing applied; vice versa, a down shift is the consequence of drag increase. The velocity profile in the right figure of Fig. 4.7 does not fit with the well known $\frac{1}{k}\ln y^+ + B$.

As it is reported in [11], the vertical shift of the velocity profile can be quantified by recalling equations 2.20, reported here:

$$\overline{u^+} = \frac{1}{\kappa}\ln\left(\frac{y}{\delta_\nu}\right) + B \qquad U_c^+ - \overline{u^+} = -\frac{1}{\kappa}\ln\left(\frac{y}{\delta}\right) + B_1 \tag{4.6}$$

Inserting another simple relation from [24], to tie U_b and U_c, namely:

$$U_c^+ = U_b^+ - \frac{1}{\kappa} \tag{4.7}$$

where κ is the Von Kàrmàn constant, cited in previous chapters.

Assuming a smooth channel flow, as it is, the resulting equation that relate the friction coefficient to the the Re_τ and the two constant in the previous equations, B and B_1, reads:

$$\sqrt{\frac{2}{C_f}} = \frac{1}{\kappa} \ln Re_\tau + B + B_1 - \frac{1}{\kappa} \tag{4.8}$$

Finally, if κ and B_1 remain constant in both the controlled and uncontrolled simulations, a variation of the constant B directly affect the friction coefficient by a determinable amount. For a `CPG` simulation, where Re_τ is constant by definition [11]:

$$\Delta B = \sqrt{\frac{2}{C_{f,0}}} \left[(1 - R)^{-\frac{1}{2}} - 1 \right] \tag{4.9}$$

As it is expected for this fist group of simulations, when the induced velocity amplitude A^+ is kept constant along with the wavenumber κ_x, the only parameters that can influence C_f are contained in the function $f(z)$. The fraction of surface covered by the spanwise velocity b.c. and the effective number of interruptions introduced to mimic the presence of multiple actuators are the two main parameters that are responsible of producing a positive drag reduction or a drag increase.

This first case is important do understand the intrinsic problem of the model, it correctly predicts a positive correlation between the surface covered by the forcing and the DR performance, while it introduces undesired effects every time an actuator is added to the simulation. Since it is not possible to consider all the complex interactions typical of DBD plasma actuators in the few parameters used, it is clear that this model is far too simple for the scope of the work.

4.4 Case 2: DNS simulations with modelled body forces

4.4.1 Suzen-Huang model

The model proposed by Suzen et al. in [35] expresses the the electrohydrodynamic (EHD) force in term of the applied voltage V; A.2.1 describe how the solution of the model has been computed and other details. Under the hypothesis of neglectable magnetic forces, body forces are compute by:

$$\mathbf{b} = \rho_c \mathbf{E} \tag{4.10}$$

where ρ_c is net the charge density (SI unit is $\mathrm{C\,m^{-3}}$) and $\mathbf{E}$ is the electric field (SI unit is $\mathrm{V\,m^{-1}}$).

The electric field can be derived by a scalar potential thanks to the Maxwell's equation with constant and null magnetic field, that imply a non-rotational electric field:

$$\mathbf{E} = -\nabla \Phi \tag{4.11}$$

The scalar potential Φ is broken down into the sum of two different contribution, one due to the external electric field, ϕ , and the second due to the net charge density in the plasma, ψ.

The net charge density ρ_c and the scalar potential due to the external electric field ϕ are computed from the following sets of second order decoupled equations, that are derived from Gauss's law and some basic algebra, reported in [35]:

$$\begin{cases} \boldsymbol{\nabla} \cdot (\epsilon_r \nabla \rho_c) = \dfrac{\rho_c}{\lambda_d^2} & \text{2nd order eq.} \quad (4.12a) \\ \rho_c = 0 & \text{Dirichlet b.c. on outer bounds} \quad (4.12b) \\ \rho_c = 0 & \text{Dirichlet b.c. on exposed electrode} \quad (4.12c) \\ \rho_c = 1 & \text{Dirichlet b.c. on embedded electrode} \quad (4.12d) \end{cases}$$

where ϵ_r is the relative permittivity and λ_d is the Debye length.

$$\begin{cases} \boldsymbol{\nabla} \cdot (\epsilon_r \nabla \phi) = 0 & \text{2nd order eq.} \quad (4.13a) \\ \dfrac{\partial \phi}{\partial n} = 0 & \text{Neumann b.c. on outer bounds} \quad (4.13b) \\ \phi = 1 & \text{Dirichlet b.c. on exposed electrode} \quad (4.13c) \\ \phi = 0 & \text{Dirichlet b.c. on embedded electrode} \quad (4.13d) \end{cases}$$

Finally, equation 4.10 is rewritten in terms of non dimensional variables as:

$$\mathbf{b} = \rho_c \left(-\nabla \phi\right) = \rho_c^{max} f(t) \phi^{max} f(t) \left[\rho_c(\mathbf{x}) \left(-\nabla \phi(\mathbf{x})\right)\right] \quad (4.14)$$

A finite difference solver has been developed to solve equations 4.12 and 4.13 on a 2D domain. The domain lies in the $y - z$ plane, that contains both the exposed and the embedded electrodes. The two matrices that result from the numerical solution of the previous equations are used to numerically solve equation 4.14 by computing the numerical gradient of ϕ and multiplying the latter with ρ_c: b_x and b_y are now available.

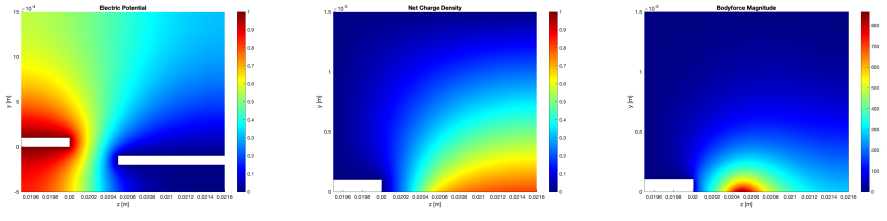

Figure 4.8: Electric potential ϕ, net charge density ρ_c and magnitude of the normalized body forces $\mathbf{b}$ computed on a 2D domain containing a single plasma actuator and $\lambda_d = 2.5\,\text{mm}$. $y - z$ plane. For comparison see [35] and [5].

The results obtained by Suzen-Huang model agree with results in [35]. If the EHD force is decomposed in the spanwise and wall-normal component, the $y-$component is roughly of the same magnitude of the $z-$component.

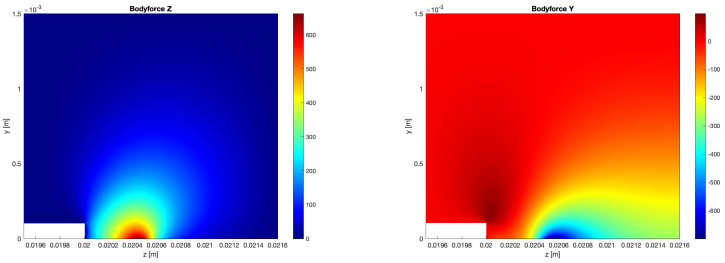

Figure 4.9: Respectively the spanwise and wall-normal component of the EHD forces computed by Suzen-Huang model. $y-z$ plane.

To have an idea of the respective amplitude of the two components, it is worth to look at the aggregate value on the spanwise direction and plot the trend in the wall-normal direction, shown in Fig. 4.10. The wall-normal forcing outperform the spanwise one in the region near the wall, while stay a little lower for the rest of the domain; this problem is going to badly affect DR performances.

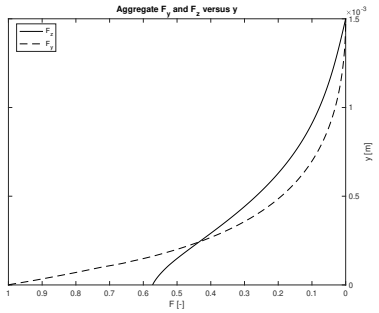

Figure 4.10: Aggregate values for F_z and F_y versus $y-$coordinate. Values are non-dimensionalized on the maximum absolute value of both F_z and F_y.

The integral values ratio is:

$$\frac{\int_\Omega b_y d\Omega}{\int_\Omega b_z d\Omega} = 0.9478 \tag{4.15}$$

where Ω is the 2D domain that contains an actuator.

In order to include the forcing in the code, it is spatially scaled in a proportional manner along the two dimensions. The main parameter used in the spatial scaling is the one related to the vertical scale; indeed, as it is reported in [23], it is convenient to define a vertical length in viscous units that identify the height of the forcing. This length is defined as the wall-normal altitude from the wall where the force strength drops to lower than 5% of the maximum and is called Δ_H^+. The amplitude of the force is scaled in order to obtain a specific value of the induced spanwise velocity in absence of the flow equal to $w^+ = 4-5$, the scaling factor is $K_{A2} = 0.8$.

4.4.2 Numerical Simulations and Results

Once the body forces are computed, as described in 4.4.1 and in A.2.1, vector $\mathbf{b}$ is included in the discretized equation using the pre-processing procedure described in A.2.2.

The vertical parameter is set to $\Delta_H^+ = 20$; the 2D body forces field related to a single actuator is scaled according to Δ_H^+ and K_{A2}. Then, the field is extended in the third dimension by multiplying the 2D actuator by a sinusoid in streamwise direction:

$$\mathbf{b_1}(x, y, z) = \mathbf{b_{2D}}(y, z) \sin(\kappa_x x) \tag{4.16}$$

where the streamwise wavenumber is $\kappa_x = 2$, $\mathbf{b_1}(x, y, z)$ is the single actuator in 3D and $\mathbf{b_{2D}}$ is the single 2D actuator from SH model that must be extended in the third dimension.

The single 3D actuator is now ready for "copy and paste" in the spanwise direction for N_{act} times; the distance between two actuators that follow each other is set to them to be equally spaced in the whole domain:

$$\mathbf{b}(x, y, z) = f(z) \cdot \mathbf{b_1}(x, y, z) \tag{4.17}$$

where $f(z)$ is a sort of Boolean function of $z-$coordinate that is in charge of placing the actuators in the right place. Regarding the first simulation with averaged body forces, function $f(z)$ average one single actuator in the spanwise direction and assign the average value for each streamwise coordinate in the whole $z-$direction. In Fig. 4.11 are some examples of the resulting fields.

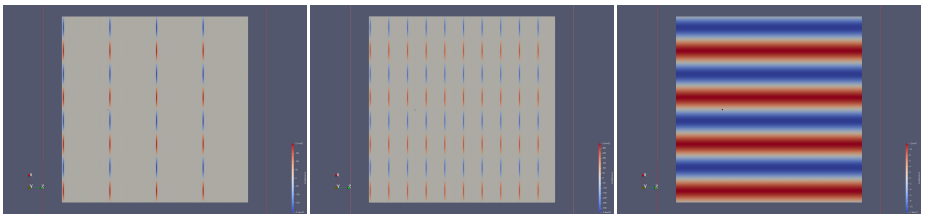

Figure 4.11: Respectively the spanwise body forces from the SH model for $N_{act} = 4$, $N_{act} = 10$ and $N_{act} = 0$ (averaged body forces). $x - z$ plane at $y = 0.025$, or $y^+ = 5$. Flow is directed like x, from bottom of the figures to the top.

Table 4.4: Values of Re_τ, Re_b, the number of actuators N_{act}, the drag reduction R, its uncertainty δR and ΔB for simulation with SH modelled body forces (case 2).

Re_τ	Re_b	N_{act}	R[%]	δR[%]	ΔB
200	3226	-	6.5	1.01	0.534
200	3495	- (x2.5)	15.8	0.911	1.41
200	3095	2	-3.8	1.11	-0.289
200	3018	4	-9.4	1.17	-0.696
200	2711	10	-36.8	1.46	-2.27
200	2255	20	-104	-	-
200	2517	35	-58.5	-	-
200	3356	50	13.0	0.945	1.12

After treating with the discretized wall boundary conditions of the first case, it is clear that the crucial points, now the body forces have been introduced, are:

- to investigate what happens in the small regions where the effect of the actuators fades but the flow is still affected by the forcing.
- to investigate how the interruptions due to discretization influence the whole flow.
- to understand the effect of these previous mechanisms on the DR performance.

Surprisingly, the answer to the first of these points is quite the same as the one depicted in the first case. Indeed, looking at Fig. 4.12, one can recognize a striking resemblance between the field produced by the body forces and by the direct imposition of the discretized boundary condition (e.g. Fig. 4.5).

Where the induced velocity is negligible, the streamwise velocity assume lower values. The "slow" areas are flanked by the "fast" streamwise regions located above the actuators; looking at the vertical component of the velocity, the same events of sweeps and ejections appear. As a result, the shown case with $N_{act} = 10$ presents a severe drag increase, as the "fast" regions lower the position of the log-layer and viscosity dissipates energy.

On the other hand is $N_{act} = 50$; the increased number of actuators produce a smoother induced velocity field (Fig. 4.13). The actuators are placed very close one to each other, the unoccupied space is about $\delta z^+ = 15$ for each actuator, where the single actuator is large $l_z^+ = 40$.

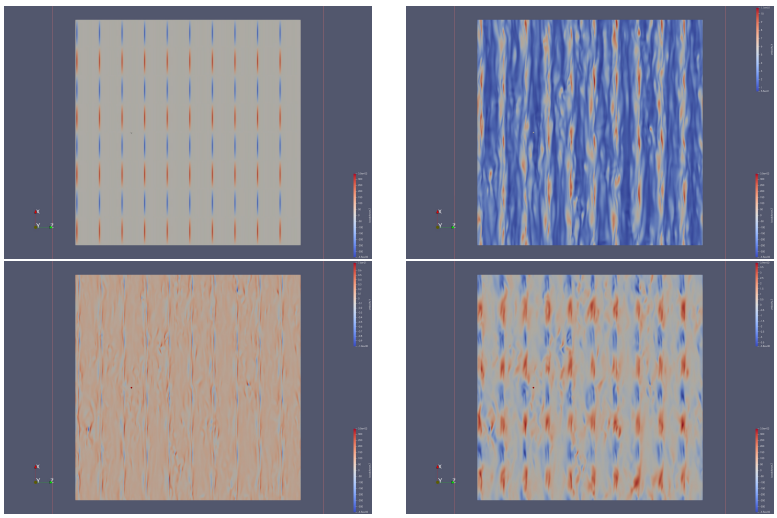

Figure 4.12: Respectively the spanwise body forces from the SH model and the three velocity components, (u, v, w), for $N_{act} = 10$ simulation at $Re_\tau = 200$. $x - z$ plane at $y = 0.025$, or $y^+ = 5$.

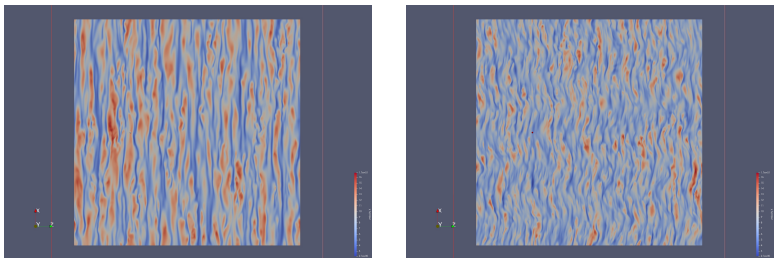

Figure 4.14: Respectively the streamwise instant velocity field, u, for no-forcing and for $N_{act} = 50$ simulations at $Re_\tau = 200$. $x-z$ plane at $y = 0.05$, or $y^+ = 10$. Same magnitude scale for both images.

The induced spanwise velocity is so smooth along $z-$direction that a completely different mechanism arises. The localized intense v events are no longer present in a such massive amount, streamwise velocity field is now uniform and it is not possible to recognize two distinct kind of regions, the flow looks smoother and the mean streamwise velocity profile pushes upwards the log-layer by thickening the viscous sublayer.

The $N_{act} = 50$ simulation is the only simulation of this second block that shows such behaviour. Fig. 4.15 shows that this particular case ($N_{act} = 50$) is the only simulation with discrete body forces that can produce a positive effect on DR; the trend explains that adding more and more actuators, without being able of creating a smooth spanwise velocity field, does not achieve any positive drag reduction.

$R[\%]$ vs. N_{act} follows a linear trend for $1 \leq N_{act} \leq 20$. The curve has a minimum for $N_{act} = 20$, where the slope pass from negative to positive. $N_{act} = 35$ has been chosen a posteriori, as an additional simulation, to confirm

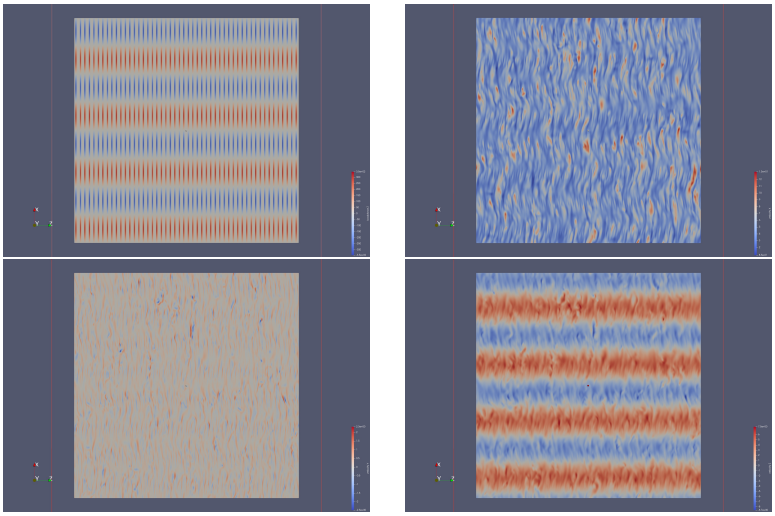

Figure 4.13: Respectively the spanwise body forces from the SH model and the three velocity components, (u, v, w), for $N_{act} = 50$ simulation at $Re_\tau = 200$. $x - z$ plane at $y = 0.025$, or $y^+ = 5$.

the trend and indeed it results to be a middle point between the the worst ($N_{act} = 20$) and the best case ($N_{act} = 50$).

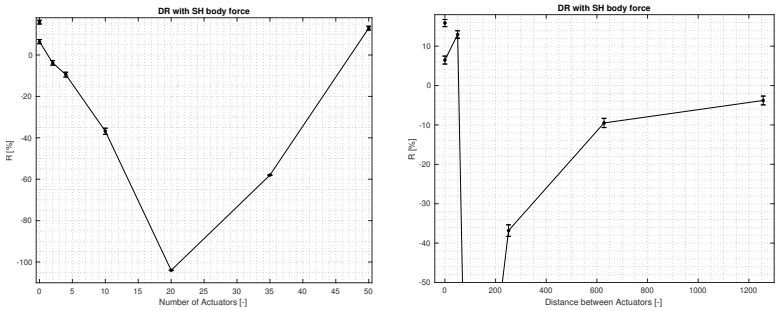

Figure 4.15: $R[\%]$ vs N_{act} and $R[\%]$ vs δ_z^+. $Re_\tau = 200$, $N_{act} = 0$ stands for the continuous case with no interruptions and the second point for $N_{act} = 0$ is with magnitude increased by 2.5. Right diagram is lower bounded at $R = -50$. Error bars at 95% Confidence level.

4.5 Case 3: DNS simulations with computed body forces

4.5.1 Body Forces from EHD numerical simulations

The third step consist of introducing the body forces computed by Professor Hiroyuki Nishida from TUAT University of Tokyo. The computed vector **b** does not come from a simplified model, as was done in the previous section

4.4, and obviously not from the direct imposition of the spanwise velocity, as in section 4.3.

The computations performed by Professor Nishida simulate the EHD forces produced by DBD plasma actuators, without the superposition of any flow-rate or pressure gradient. The 3D EHD simulations consider only a small portion of the hypothetical complete flow field, in order to keep the computational resources as reasonable as possible, and for a certain amount of time; the results are directly time-averaged over one AC cycle by Professor Nishida. The region considered is the one depicted by the dashed red rectangle in Fig. 4.16; the shape of the portion is chosen in order to have the smallest possible region that contains both a negative and a positive half of the half-moons (depicted in grey).

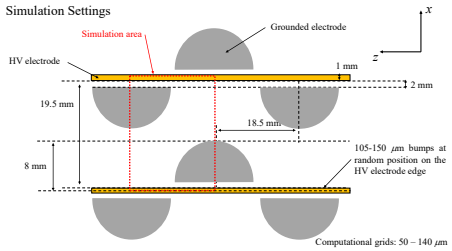

Figure 4.16: Settings for the EHD force simulations. The red dashed square defines the simulated region, grey half-moons represent the sinusoidal grounded electrode. Image courtesy of Professor Hiroyuki Nishida from TUAT University of Tokyo.

The results provided comprehend an actuator that works at three different frequencies:

- $f_{AC} = 25\,\mathrm{kHz}$
- $f_{AC} = 35\,\mathrm{kHz}$
- $f_{AC} = 50\,\mathrm{kHz}$

It is necessary to consider that the simulation of lower frequencies requires longer computational time, the case of $f_{AC} = 1\,\mathrm{kHz}$ adopted in the experiment by Poitiers University needs more than two months for simulating one AC cycle. As confirmed by looking at the data and by Professor Nishida, although the force amplitude increases with the frequency, the qualitative characteristics of the field are the same in all three frequencies. In any case, the body forces amplitude should be scaled adjusting it the to experimental results.

Increasing the averaging period of time would lead to a smoother force distribution at the cost of an increasing computational time or resources. Anyway, the field is smoothed later by the DNS preprocessing code in streamwise and spanwise direction, to reduce the oscillation due to the truncation in performing the Fourier transforms; further details about the implemented Gaussian smoothing in A.2.3.

The data structure of the provided force field is:

$$x\,[\mathrm{m}] \qquad y\,[\mathrm{m}] \qquad z\,[\mathrm{m}] \qquad F_x\left[\mathrm{N\,m^{-3}}\right] \qquad F_y\left[\mathrm{N\,m^{-3}}\right] \qquad F_z\left[\mathrm{N\,m^{-3}}\right] \tag{4.18}$$

and, the grid number is 370 in the $x-$direction, 50 in the $y-$direction and 410 in the $z-$direction. Each resulting `.dat` file that contains both the coordinates and the field is constituted by a $370 \cdot 50 \cdot 410 \times 6$ matrix and weights about 705 MB.

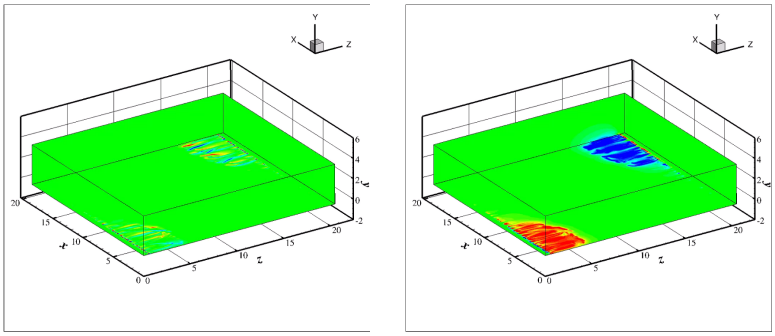

Figure 4.17: Time-averaged streamwise and spanwise body forces distribution for $V = 12\,\text{kVp}$ and $f_{AC} = 25\,\text{kHz}$. Image courtesy of Professor Hiroyuki Nishida from TUAT University of Tokyo.

As it is written in 4.18, the body forces obtained here are dimensional; the force distribution included in the code is spatially scaled in a proportional manner along the three dimensions. The main parameter used for the spatial scaling is the one related to the vertical dimension, namely $\Delta_H^+ = 20$ according to similar studies [23].

The amplitude of the force is scaled according to the spanwise velocity induced by the body forces in a simulation with no-flow. The original amplitude is multiplied by a constant $K_{A3} = 0.0036$, that is obtained only after Δ_H^+ has been chosen, to produce a spanwise velocity that is approximately $w^+ = 4 - 5$.

Fig. 4.18 shows that the actuators simulated in EHD simulations are clearly better with respect to actuators modelled by SH model; the aggregate forces are obtained by summing the values in spanwise and streamwise directions for each plane. The spanwise body force is greater then the other components in the whole domain, the integral values are respectively:

$$\frac{\int_\Omega b_x d\Omega}{\int_\Omega b_z d\Omega} = 0.0096 \qquad \frac{\int_\Omega b_y d\Omega}{\int_\Omega b_z d\Omega} = 0.2290 \tag{4.19}$$

where Ω is the domain that contains half of the positive or the negative half-moons.

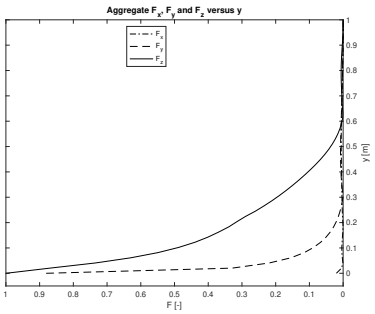

Figure 4.18: Aggregate values for F_x, F_y and F_z versus $y-$coordinate. Values are non-dimensionalized on the maximum absolute value of all F_x, F_y and F_z.

4.5.2 Numerical Simulations and Results

The EHD simulations provide only one positive and one negative of the half-moons. The simulations of this third case require to have these pieces of the field "glued" together and then mirrored along the streamwise direction to obtain the single complete actuator; the entire procedure is described in A.2.2.

As the vertical parameter is set $\Delta_H^+ = 20$, the scaling of the actuators is fixed to this value. Fortunately, this particular scaling perfectly matches with the original sinusoidal function imposed with $\kappa_x = 2$. Once the single actuator is extended for the full length of the channel, resulting in $\mathbf{b_1}(x, y, z)$, the complete body forces field is obtained by "copy and paste" along the spanwise direction for N_{act} times.

The same procedure in 4.4.2 is used to pass from $\mathbf{b_1}(x, y, z)$ to $\mathbf{b}(x, y, z)$:

$$\mathbf{b}(x, y, z) = f(z) \cdot \mathbf{b_1}(x, y, z) \tag{4.20}$$

Here are some examples of the resulting body forces fields, Fig. 4.19. For $N_{act} = 30$ (center) actuators are close one to each other with no overlap, while $N_{act} = 40$ (right) simulation present little overlap.

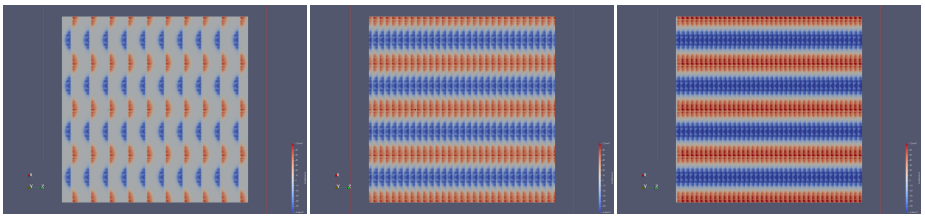

Figure 4.19: Respectively the spanwise body forces from the EHD simulations for $N_{act} = 10$, $N_{act} = 30$ and $N_{act} = 40$. $x - z$ plane at $y = 0.025$, or $y^+ = 5$. Flow is directed like x, from bottom of the figures to the top.

Simulations shown in this third case only confirm what was presented for the second case. If the number of actuators is not large enough (or better, the distance between two actuators is not small enough), a large drag increase occurs in the flow. Indeed, when the flow induced by one actuator is not able

Table 4.5: Values of Re_τ, Re_b, the number of actuators N_{act}, the drag reduction R, its uncertainty δR and ΔB for simulation with EHD computed body forces (case 3).

Re_τ	Re_b	N_{act}	$R[\%]$	$\delta R[\%]$	ΔB
200	3327	-	15.7	0.952	1.40
200	3027	1	-10.1	1.25	-0.736
200	2875	2	-21.5	1.32	-1.45
200	2562	4	-52.6	-	-
200	2062	10	-127	-	-
200	2713	20	-34.3	1.45	-2.16
200	3105	30	6.1	1.03	0.503
200	3191	40	6.5	1.01	0.535

to smoothly "connect" with the flow induced by the nearest one, the flow field shows some recognizable patterns:

- Averaged wall-normal velocity is close to zero everywhere, except on the actuators. Fig. 4.20 shows localized events of positive and negative vertical velocity (that resemble ejections and sweeps) caused by both the nonzero b_y and the instant interruption of the spanwise body forces.
- Streamwise velocity is characterized by "fast" and "slow" stripes of fluid, as described in the second case. The fast regions are placed above the actuators and flanked by the slow regions, that are located on the no body forces areas; obviously, their dimension strongly depends on N_{act}. The fast stripes are responsible of both diminishing the viscous sublayer thickness and creating a shear $\frac{\partial \overline{u}}{\partial z}$ that dissipate energy by viscosity. Shown in Fig. 4.21 and 4.22.

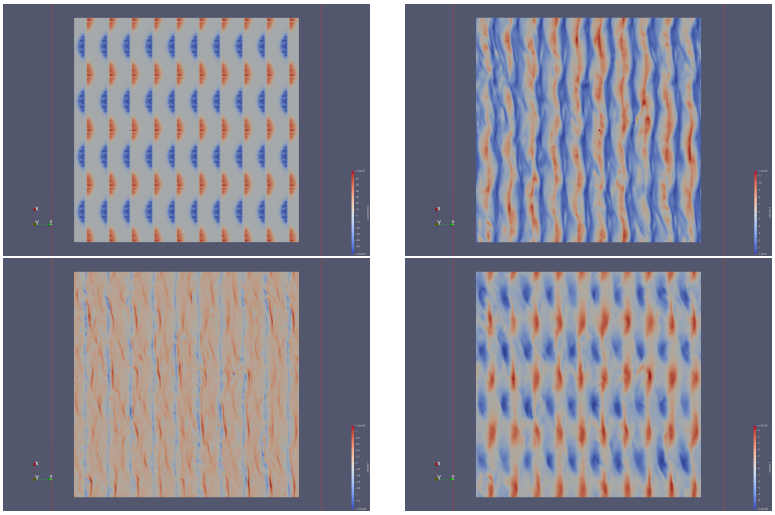

Figure 4.20: Respectively the spanwise body forces from the EHD simulations and the three velocity components, (u, v, w), for $N_{act} = 10$ simulation at $Re_\tau = 200$. $x - z$ plane at $y = 0.025$, or $y^+ = 5$.

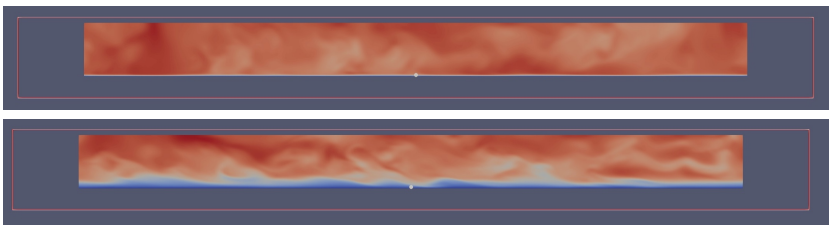

Figure 4.21: $x-y$ plane for $N_{act} = 4$. Top figure is taken in the $z-$coordinates corresponding to an actuator, bottom figure is taken as far as possible from the actuators.

Figure 4.22: $z-y$ plane for $N_{act} = 4$. Position of the actuators over the streamwise velocity field in transparency.

Meanwhile, if the number of actuators is large enough (the distance between two actuators is small enough), the current technique can produce a positive drag reduction. When the flow induced by the actuators is somehow continuous and as smooth as possible, the flow field behaviour is characterized by different events:

- Averaged wall-normal velocity is close to zero everywhere; some events of vertical speed are present but they are not localized in a precise location as it happens in DI cases; they randomly change with time advancement, Fig. 4.23. The less intense are these event and the best DR performance is achieved; the simulation with continuous body forces outperforms the discrete simulations $N_{act} = 30$ and $N_{act} = 40$ by obtaining less frequent and less intense vertical velocity events.
- Streamwise velocity field shows no recognizable patterns; the flow field shows some events typical of turbulent flows, but much less distinct and intense. The flow looks kind of uniform with respect to the DI simulations, the fluctuations around the mean streamwise velocity are definitely of a lower order of magnitude, there are no more two different regions. Lastly, the mean streamwise velocity profile exhibits a thicker viscous sublayer, resulting in an upwards shift of the log-layer, as it is explained in the previous sections. The shear is no longer present in such a massive amount.

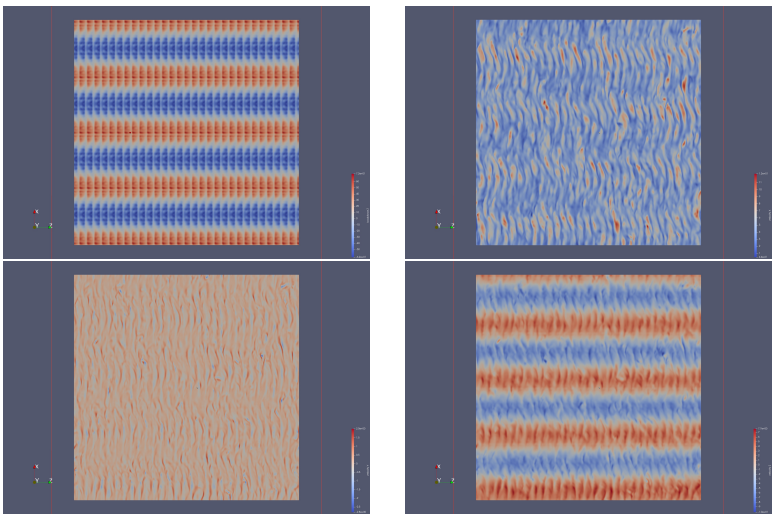

Figure 4.23: Respectively the spanwise body forces from the EHD simulations and the three velocity components, (u, v, w), for $N_{act} = 30$ simulation at $Re_\tau = 200$. $x - z$ plane at $y = 0.025$, or $y^+ = 5$.

The trend of this third case of the study is explained in Fig. 4.24; the pattern is quite similar to the second case. The worst DR performance is obtained in the continuous case $N_{act} = 10$; $R[\%]$ vs. N_{act} follows a linear trend for $1 \leq N_{act} \leq 10$, then the slope change sign to reach positive values of DR for $N_{act} = 30$ and $N_{act} = 40$. The $N_{act} = 30$ report an effective distance between two actuators of about about $\delta z^+ \approx 5$ for each actuator, while the $N_{act} = 40$ has no δz^+ because of a little overlap.

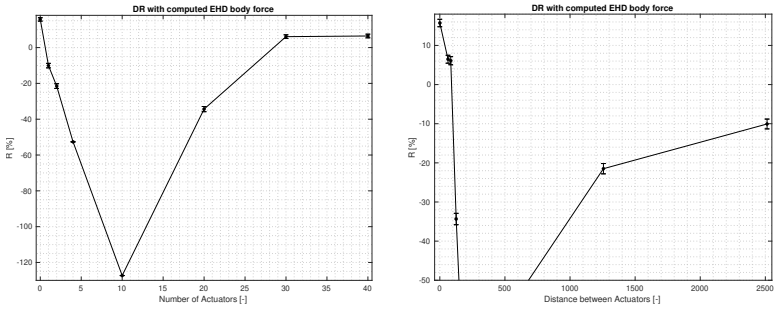

Figure 4.24: $R[\%]$ vs N_{act} and $R[\%]$ vs δ_z^+. $Re_\tau = 200$, $N_{act} = 0$ stands for the continuous case with no interruptions. Right diagram is lower bounded at $R = -50$. Error bars at 95% Confidence level.

The same identical simulations of table 4.5 have been performed, as some computational resources were left over, with an increase magnitude of the body forces and the same spacing. The constant multiplier K_{A3} is multiplied by 2.5 in order to obtain roughly a double induced spanwise velocity, $K_{A3} = 0.0036 \cdot 2.5$. This set of simulations were not completely finished, as the amount of time and resources was not enough, but the output can be very insightful if related with the "less intense" case. First of all, increasing the amplitude of the body forces

leads to an increased spanwise velocity, while the extent of the induced velocity is roughly unchanged w.r.t. to the "less intense" case. The results of this last set of simulations exhibit a strong drag increase in the whole package of simulations, except for the continuous $N_{act} = 0$ that show a better DR performance; the trend is anyway confirmed with $N_{act} = 10$ as the worst case and $N_{act} = 30$ as the discrete simulation with the smallest DI. This result can be explained with the presence of non negligible body forces in wall-normal direction that are increased in intensity; in addition, the induced field is far less smooth with the increased body forces.

4.6 Statistical profiles comparison of the three cases

This last section of the results is dedicated to the graphical comparison of the statistical profiles of the previous simulations. The following charts report, for each case, the profiles related to:

- the continuous simulation $N_{act} = 0$
- a discrete simulation, not connoted by a specific performance, namely $N_{act} = 2$
- the simulation with the highest drag increase
- the simulation with the highest drag reduction

Looking at the mean velocity profiles in Fig. 4.25, the continuous simulations (a) are all able to achieve a positive drag reduction, the log-layer shift upwards because of the thickening of the viscous sublayer, as it is analytically explained by Eq. 4.9. The best performing discrete simulations (d) are characterized by the same phenomenon, but on a smaller scale; it is not completely clear why two profiles are somehow lower w.r.t. to the reference simulation approximately in the buffer layer $5 < y^+ < 30$. The opposite mechanism emerges in the drag increase cases (c).

The rms velocity profiles regarding the continuous simulation, Fig. 4.26, are quite similar to the reference profiles. It is possible to recognize a strong difference in the w_{rms} chart because of the forcing: the blue line stands for the wall boundary condition, as it is not null at the wall, while the other two lines are related to the body forces. In addition, each simulation produces a lowering of the peak in the $-u'v'$ chart and the new peak is shifted to the higher y^+. As this particular set features averaged body forces (for case 2 and 3) in the spanwise direction, the vertical component of the body forces field is reasonably much lower with respect to the discrete sets, so it is v_{rms}.

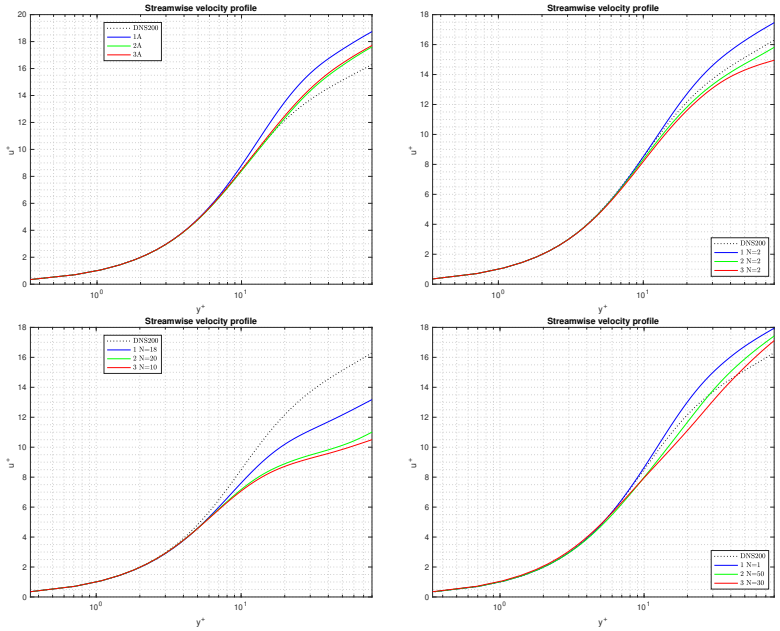

Figure 4.25: Respectively the mean streamwise velocity profiles of the continuous simulations (a), $N_{act} = 2$ (b), worst performing simulations (c) and best performing simulations (d).

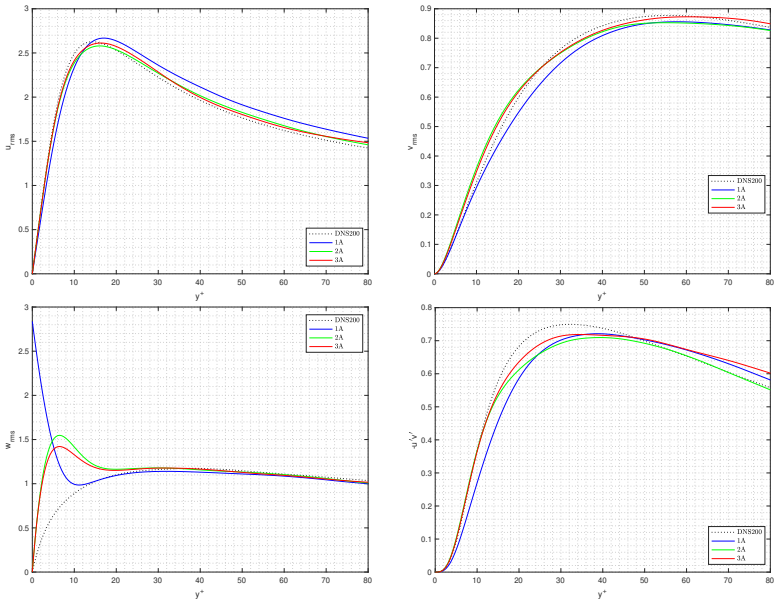

Figure 4.26: Respectively the three rms velocity profiles (a,b,c) and the most relevant component of the Reynolds stresses(d) of the continuous simulation for each case.

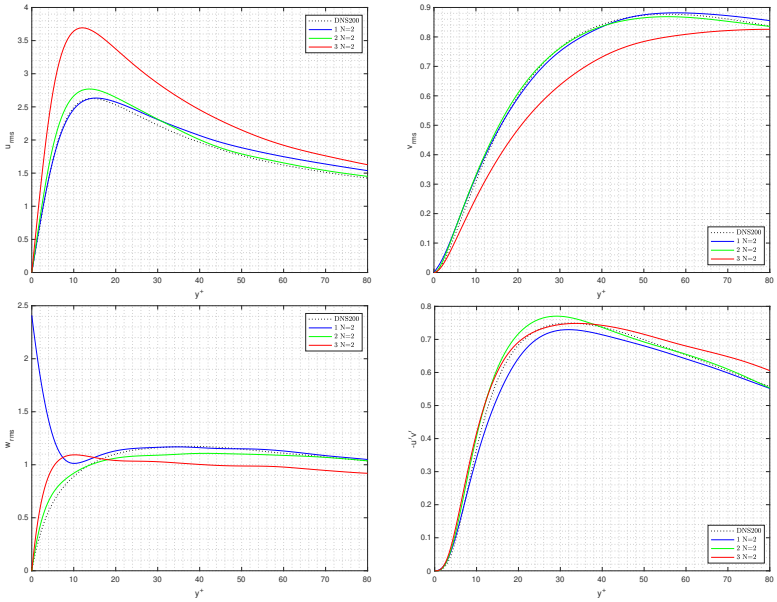

Figure 4.27: Respectively the three rms velocity profiles (a,b,c) and the most relevant component of the Reynolds stresses(d) of the $N_{act} = 2$ simulation for each case.

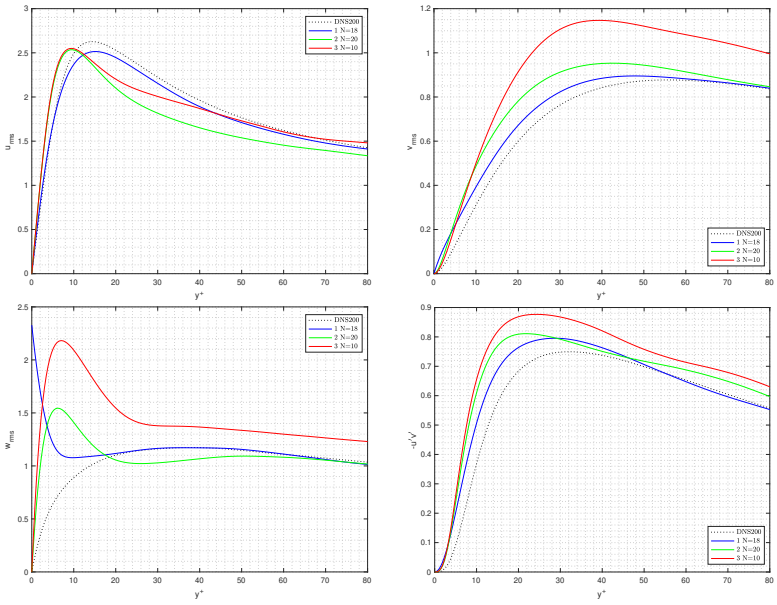

Figure 4.28: Respectively the three rms velocity profiles (a,b,c) and the most relevant component of the Reynolds stresses(d) of the worst performing simulation for each case.

Fig. 4.28 display the rms velocity for the simulations that are responsible of the greatest drag increase; the most relevant differences with the continuous

set are present in the vertical velocity component, that is far more important in this case, and in the $-u'v'$ component of the Reynolds stress. On the opposite is Fig. 4.29. It is indeed true that v_{rms} profiles are quite similar to the previous ones, but case 2 (green) and case 3 (red) also show a lower peak in u_{rms}. Finally, $-u'v'$ profiles have a similar behaviour to the continuous simulations, but the profile is flattened with the peak anticipated in third case. All the four charts clearly tell that some mechanism is acting in the region $5 < y^+ < 30$, approximately the buffer layer and where the actuators produces their body forces (recall $\Delta_H^+ = 20$).

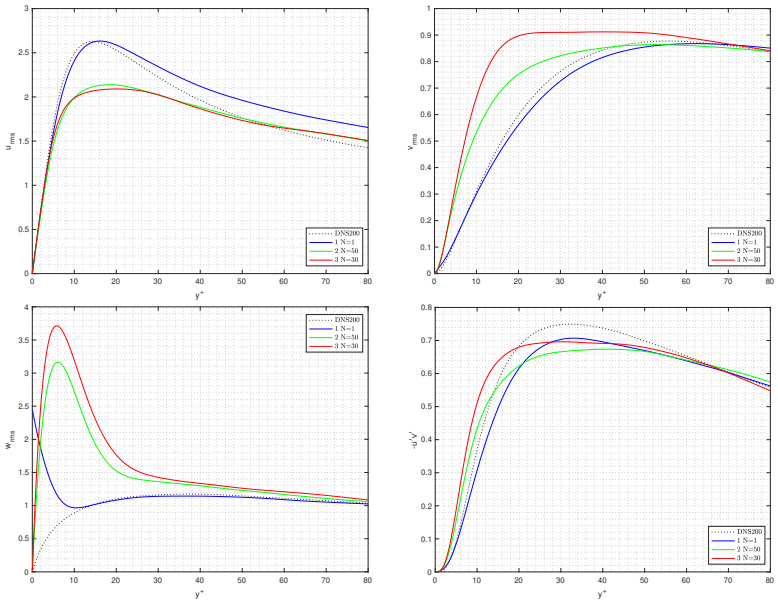

Figure 4.29: Respectively the three rms velocity profiles (a,b,c) and the most relevant component of the Reynolds stresses(d) of the best performing simulation for each case.

Production profiles in Fig. 4.30 show constantly increased peaks for the worst performing set; the peaks are also anticipated of about 5 viscous unite. On the other hand, the continuous simulations are characterized by lower and later peaks; similar to what happen in the best performing discretized set, with some viscous turbulent phenomena that are responsible of a strong increase in dissipation in the buffer layer, that probably decrease the effectiveness of the technique.

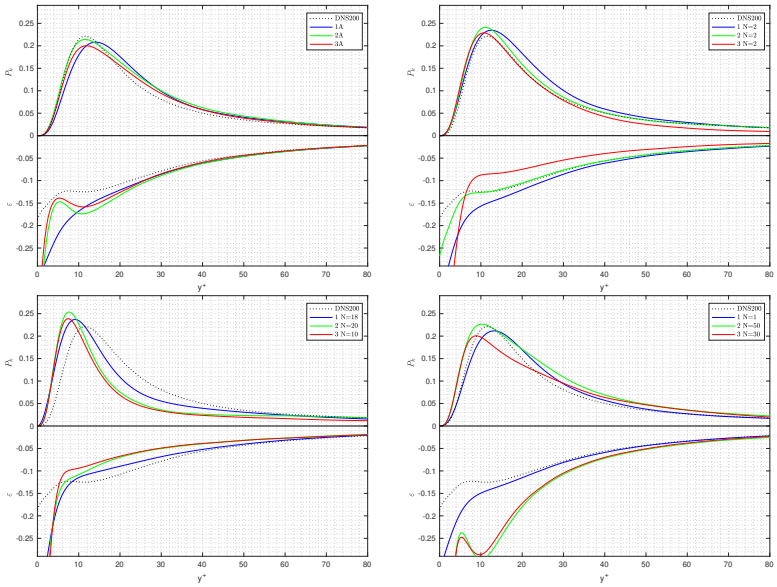

Figure 4.30: Respectively production P_k and dissipation ε profiles of the continuous simulations (a), $N_{act} = 2$ (b), worst performing simulations (c) and best performing simulations (d).

5. Conclusions

Is it possible to achieve turbulent skin-friction drag reduction using DBD plasma actuators? The answer is: yes, it is possible.

The present study has considered different configurations and different DBD models; they have been investigated with thirty-five direct numerical simulations (DNS) of a fully turbulent channel flow at $Re_\tau = 200$. The work started with a set of preliminary no-flow simulations to assess the spanwise velocity induced by the actuators; once this was set, three different cases were used to model the drag reduction technique, with increasing complexity in the modelling of the force field. Jointly, the simulations constitute an effort to understand the detrimental effects of moving from an idealized, spanwise-continuous setting to the spanwise-discrete distribution of actuators that is unavoidable in an experiment of practical application.

The various models all presented various issues that become less severe with the increasing complexity of the model:

- The first case directly introduced the spanwise-discrete forcing by still introducing the spanwise velocity as a boundary condition, but intermittently in space; this is the simplest attempt, which resulted in an incorrect trend. The indication is that, the larger the number of actuators, the poorer is the DR performance.

- The second case has modeled the DBD actuators, according to the Suzen-Huang model; the model can not be as accurate as the measured or computed data, but the predicted trend becomes reasonable. Still, increasing the number of actuators badly affect DR, but only so until their total number becomes large enough to produce a smooth field of induced velocity. It is possible to identify $\delta z^+ = 15$ as the maximum distance between two actuators, using the present parameters. The problem was the massive wall-normal component of the body forces field, that reduces the effectiveness of the technique.

- The third case used a spatial distribution of body forces after the EHD simulation provided by Professor Hiroyuki Nishida. In this case, data showed a strongly decreased wall-normal component and a negligible streamwise component; the trend was the same obtained in the second case, with slightly different numerical results. However, a large forcing amplitude was found to decrease the performance. A problem that was necessary to face consisted in the correct positioning of the actuators, because of the extremely small spatial domain that was considered in the plasma simulations, along with the fixed 3D geometry that must be fitted in the streamwise direction.

The best discrete simulation has obtained $\approx 13\%$ of drag reduction, and other two discrete simulations yielded $\approx 6.5\%$, suggesting that in a real DBD experiment values of at least 10% can be achieved. The best results are obtained with well packed actuators; as a general rule, the closer they are the more the skin friction is reduced, but a spacing of about $\delta z^+ \approx 5 - 15$ yields the best performances. The current study thus confirms that spanwise forcing can be used in a real experiments with DBD actuators, but it also highlights the need of further optimization in both the positioning of the actuators and the force produced by the actuators.

A continuation of the present work should further investigate an optimal positioning of the actuators on the channel wall; it would be necessary to understand if there is a possibility to choose different distances between each actuator or to place the following actuator slightly ahead or behind in a favourable manner. The third case studied in the current work revealed also a link between the number of actuators and the amplitude of the forcing produced, this relationship should be better investigated with a larger number of simulations. In addition, once the previous works are completed, it would be interesting to simulate the same channel flow with the measured body forces distribution, obtained by an ongoing PIV experiment from Professor Nicolas Benard, on the most promising cases.

A. Technical aspects of the DNS code

The main script is `channel.cpl` and, after calling the necessary libraries and accessory scripts, having defined the input parameters, it loops in time by calling the functions contained in the accessory scripts. The functions are contained in three `.cpl` scripts: `dnsdata.cpl`, `dnsdirect.cpl` and `rbmatmod.cpl`.

This last script is basically a library that contains functions related to the LU matrix decomposition used to compute derivatives by compact schemes. `dnsdirect.cpl` is a module that contains all the low-level functions that constitute the loop in time, so it is responsible to build the right hand side of discretized $v - \eta$ equations, to define the convolution function, to define the timescheme, to transform (v, η) to (u, w, w) and others. `dnsdata.cpl` is used for high level interactions, so it responsible of reading the input file with the user parameters, to define functions to write output files, define initial conditions and coordinates of the grid, read the file to restart a simulation and others.

The code is written in order to be compiled once for all, input parameters are changed by modifying the input file `dns.in`.

A.1 Input file

The `dns.in` file, that the code reads before starting the simulation, is set by the user and contains the following parameters:

- **nx, nz, ny**: number of modes in the streamwise and spanwise directions, number of discretization points in wall-normal direction
- **alpha_0, beta_0**: fundamental wavenumber in streamwise and spanwise directions
- **y_min, y_max, a**: the vertical position of the boundaries and the vertical parameter to choose vertical spacing between discretization points; typically $y_{min} = 0$, $y_{max} = 1$, $a = 1.2 - 1.6$
- **ni**: the Reynolds number, the code takes $ni = 1/ni$
- **meanflowx** or **meanpx**: according to the simulation, it is possible to set the mean flow rate or the mean pressure gradient in streamwise direction
- **meanflowz** or **meanpz**: as described above, but in spanwise direction
- **cfl_max** or **delta_t**: imposes the maximum CFL in the whole field or the advancement in time

- **t_max**: set the time at which the simulation will be interrupted
- **restart_file**: string to write the name of the `Dati.cart.out` file to start from; if null the simulation starts from specified velocity profile imposed in the code
- **time_from_restart**: Boolean variable that set the starting time equal to the restart_file time or not
- **dt_field**: determine the temporal spacing between the writing of two subsequent `Field*.fld` files
- **dt_save**: determine the temporal spacing between the overwriting of the `Dati.cart.out` file

A.1.1 Automatization

The process of compiling the code and run in the correct sequence all the executables, is achieved by the combinations of `shell` scripts and `source` programs. In details, the `source` code is the main code and contains few `shell` scripts and instructions to run the whole program.

The first instruction in the **main** is to run a `.sh` that clean the folder from `.fld`, `.dat`, `.txt` and executables that where produced in the previous simulations and are no longer useful. As a second step, the preprocessing `.cpl` file is compiled, the preprocessing file must be compiled every time a parameter has been changed since the process is immediate and safer; then, it is automatically run to produce the `.dat` file containing the body forces. The user can change the **main** source in order to choose to compile or not the main DNS code, as a default it is set to no. The procedure now start the DNS simulation and it run until it reach **t_max** or it is manually stopped. As a final step, the user can choose the `.fld` files to be transformed in `.vtk`, and to run the post-processing statistic analysis. Similar small `source` programs have been developed to automatically run one or more of the previous processes.

A.2 Body forces introduction

A.2.1 SH model

The body forces field coming from the Suzen-Huang model is computed using a dedicated `MATLAB` code that exploit the `PDE toolbox` and follow this scheme:

- Set the parameters **Voltage_ground**, **Voltage_diff**, **rho_b**, **lambda_d**, **epsilon_r** and the number of points to query along each dimension.
- Define the dimension and the shape of the domain and the sub-domains contained in the main domain.
- Create the unstructured grid on the sub-domains.
- Impose the boundary condition on the boundary of the domain, the problem deals with both Neumann and Dirichlet conditions.

- Define the value of each coefficient of the Transport-Diffusion PDEs on each sub-domain.
- Separately solve the two PDEs:
  - Electric Potential ϕ
  - Net Charge Density ρ_c
- Compute the gradient of ϕ on the domain
- Multiply $\nabla\phi$ and ρ_c to obtain $\mathbf{b}$
- Interpolate the solution on the whole domain
- Write coordinates and $\mathbf{b}$ to `.dat` file

Finally the code is used to compute the integral values for each component of the body forces and the ratios.

A.2.2 Pre-processing

The code for interpolation is also written in `CPL`. Since input data forces are of various natures (2D or 3D, dimensional or non-dimensional) and stored in different data structures, slightly different scripts have been developed for different purposes.

The structure of the code suggest to create an independent program that output a `body_forces.dat` file that contains three 3D arrays, one for each component of $\mathbf{b}$, that are ready to be directly inserted as body forces. This approach is the safest in this situation; indeed, the original DNS code in not heavily modified and contains few additional lines to read the `body_forces.dat` file and assign values to the 3D vector of complex real numbers.

The first step of the simulations, that require to modify the spanwise velocity at the wall, does not require any input force; indeed, the imposition of the boundary conditions is directly operated on the original code by adding few lines of code.

The second step of the work includes modeled body forces computed from Suzen-Huang (SH) model; this step requires to run, once for all, an independent code to compute b_y and b_z on a 2D non-dimensional domain and create the 2D input Body Forces file. The domain is then smoothed along the $z-$direction with the chosen shape (Gaussian, Sharp, Cauchy, ...) and dimension of the filter; the field is spatially scaled to obtain the right value of ΔP^+.

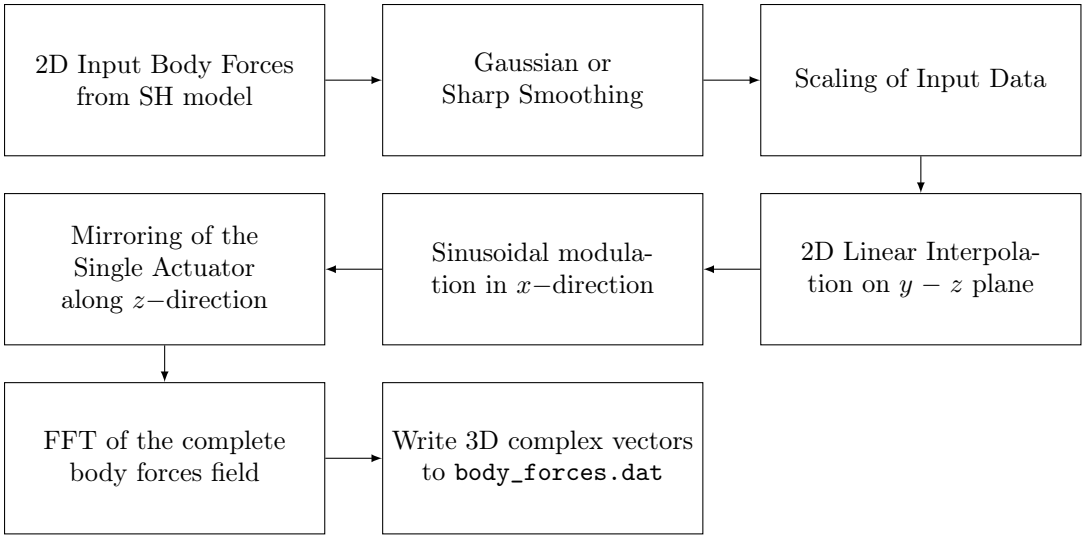

Figure A.1: Schematic workflow for typical 2D input body forces.

The modified body forces field needs to fit on the computational grid of the discretized $v-\eta$ equations, so it is interpolated in the vertical $y-z$ plane[1]; the result of the interpolation process is multiplied by a sinusoidal function $A_f^+ \cdot \sin \kappa_x x$ to obtain the third dimension. To complete the procedure, the field in now three dimensional, but contains a single actuator; once the parameters of the actuators are set (N_{act}, width and spacing), the single actuators is "copied" and placed in the spanwise direction (Mirroring of the actuator). Finally the complete body forces field is FFT transformed in both the spanwise and streamwise direction, left untouched in the wall-normal, then written to `body_forces.dat`.

The third step of the work is quite similar to the second one, the input file is now very large (close to one Gigabyte) but there are no big differences in the procedure. Data are usually dimensional, so they need to be non-dimensionalized before the scaling, in order to obtain the chosen value of ΔP^+. The linear interpolation is performed along all the three spatial dimensions; multiple actuators are obtained by "copy and paste" of a single actuator, in both the streamwise and spanwise directions.

[1] If the particular simulation requires to average in the spanwise direction, the averaging process is performed here by setting a Boolean variable. The interpolation is performed only in $y-$direction.

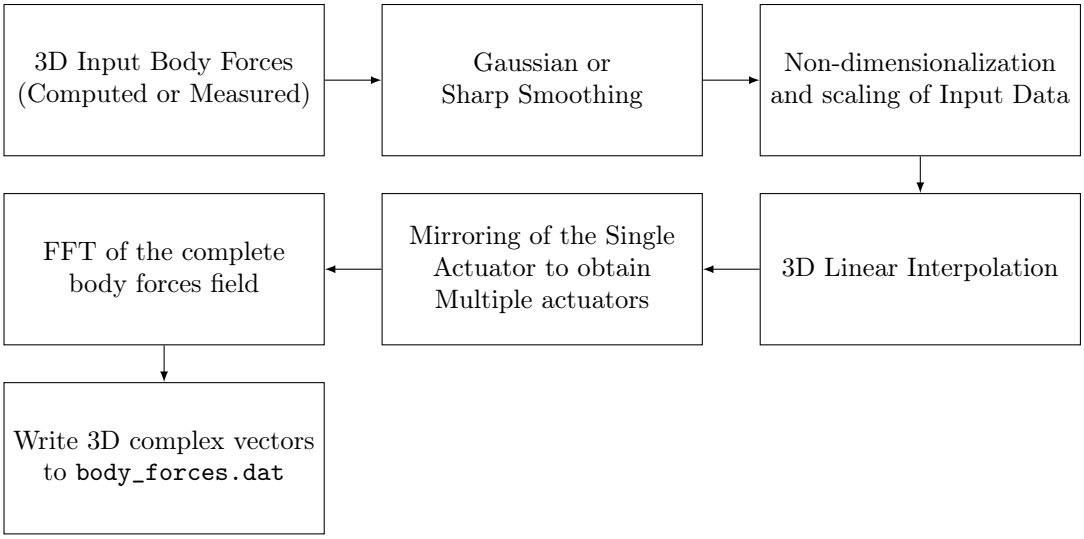

Figure A.2: Schematic workflow for typical 3D input body forces.

A.2.3 Gaussian Smoother

The need for a filter is strictly related to the choice of using a pseudo-spectral DNS code. Indeed, it is necessary to smooth the input field in the Fourier-transformed directions, namely x and z. The function created for the purpose can be used with various list of different filters, that can be found on [24] at page 563, in the example displayed here, the Gaussian filter is:

$$G(r) = \left(\frac{6}{\pi\Delta^2}\right)^{\frac{1}{2}} \exp\left\{\frac{-6r^2}{\Delta^2}\right\} \tag{A.1}$$

where r is the distance between the point considered and the other points in the filter neighborhood, while Δ is representative of the width of the filter. The filtering is performed by convolution on lines along $x-$direction and then on the $z-$direction. It is worth a consideration regarding this process; if the number of discretization point on the output is very close to the number of point of the input, a smaller window provides more accuracy without paying the cost of big oscillation. On the contrary, if one needs to pass from a very accurate dataset to a very coarse grid, it is better to wide the window in order to obtain a smoother result.

The following figure A.3 shows the enhancement due to a Gaussian filter.

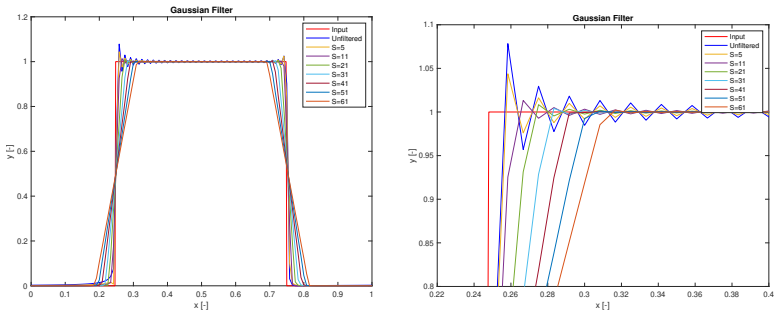

Figure A.3: Gaussian filter applied on a square input and a zoom (right) on the sharp edge. S is a parameter that accounts for the width of the filter.

A.2.4 Trilinear Interpolation

The linear interpolation is performed in both 2D and 3D cases. Since the mesh is structured and equally spaced in $x-$ and $z-$directions, it is possible to take some adjustment in order to make the process faster. Linear interpolation schemes use polynomials of order 1 and require 2^D adjacent values near the interpolation point.

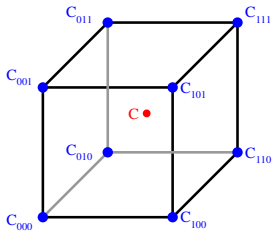

Figure A.4: 8 adjacent points to the interpolation point. [2]

The interpolation algorithm needs to identify the surrounding points; in order to make the process faster, it is possible to avoid using three nested loops by finding the $x-$ and $z-$indexes using a integer division. Once the values and coordinates of the adjacent points have been found:

$$\begin{cases} x_d = \dfrac{x - x_0}{x_1 - x_0} & \text{(A.2a)} \\ y_d = \dfrac{y - y_0}{y_1 - y_0} & \text{(A.2b)} \\ z_d = \dfrac{z - z_0}{z_1 - z_0} & \text{(A.2c)} \end{cases}$$

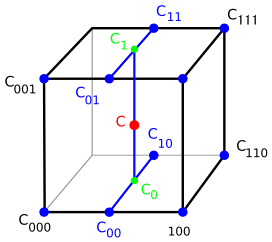

Figure A.5: Sequence of intermediate points to calculate the interpolation point. [3]

Then, the four intermediate points in x are found:

$$\begin{cases} c_{00} = c_{000}\,(1 - x_d) + c_{100} x_d & \text{(A.3a)} \\ c_{01} = c_{001}\,(1 - x_d) + c_{101} x_d & \text{(A.3b)} \\ c_{10} = c_{010}\,(1 - x_d) + c_{110} x_d & \text{(A.3c)} \\ c_{11} = c_{011}\,(1 - x_d) + c_{111} x_d & \text{(A.3d)} \end{cases}$$

Same procedure for y:

$$\begin{cases} c_0 = c_{00}\,(1 - y_d) + c_{10} y_d & \text{(A.4a)} \\ c_1 = c_{01}\,(1 - y_d) + c_{11} y_d & \text{(A.4b)} \end{cases}$$

Finally in z:

$$c = c_0\,(1 - z_d) + c_1 z_d \qquad \text{(A.5)}$$

A.3 Post-processing

The treatment of the data can be divided in two distinct processes: the need to visualize the resulting flow field and the need to obtain statistical results from the simulations. But first, it is worth describing what the code gives as output.

A.3.1 Output

The code outputs the results in different manners:

- Directly on the terminal
- Write to `Runtimedata`
- Write a new `Field*.fld` according to **dt_field**
- Overwrite the flow field and force field on `Dati.cart.out` according to **dt_save**

The first two outputs are exactly the same, but one is directly written on the terminal to have an immediate feedback about the simulation, while the second stores all the variables listed here at each time step, to calculate statistics:

Table A.1: An example of the `Runtimedata` file. All numbers have been truncated or omitted for reasons of spacing.

Time	$\tau_{w,b}$	C_f	$\tau_{w,u}$	$\frac{\partial w}{\partial y}\big\vert_b$	$\frac{\partial w}{\partial y}\big\vert_u$	u_x	p_x	u_z	p_z	cfl	δ_t	en.	dis.
0.0004	202.4	0.0082	6e-13	0.59	-5e-16	15.8	1	0.016	0	1	-	1.8	659
0.0008	202.4	0.0082	-5e-14	0.59	-9e-16	15.8	1	0.016	0	1	-	1.8	659
0.0012	202.4	0.0082	-3e-13	0.59	4e-16	15.8	1	0.016	0	1	-	1.8	659
0.0016	202.4	0.0082	1e-13	0.59	3e-16	15.8	1	0.016	0	1	-	1.8	659

The third output, `Field*.fld`, is basically used to visualize the flow field on `ParaView` and to obtain mean velocity profiles, correlations, power spectral density plots, rms velocity profiles and others.

The fourth and last output is of fundamental importance to save time in performing the simulations. Indeed, it allows the user to write the current state of a particular simulation (to `Dati.cart.out`) and to start others simulations from the state. This function can be used to stop the simulation for a certain amount of time, to change the machine it is performed on or, mainly, to produce a simulation with no forcing and then to start each particular simulation from this same state, with no need to start back from the Poiseuille laminar profile.

A.3.2 How to visualize the resulting flow field

The DNS code regularly write to an output file the flow field every Δt_{save}, as described in A.1. The original code has been modified to deal with the semi-channel instead of the complete channel and to write the body forces vector $\mathbf{b}$ to `Field*.fld` after it is transformed back to the physical space.

Once the main code has written field file, the independent code `fld2vtk.cpl` reads the `.fld` files in order to produce the respective `.vtk` files that can be visualized using `ParaView`. The original `fld2vtk.cpl` code is able to produce an output file containing only coordinates, the velocity field and the lambda2, for the complete channel. The new script add the body forces field and a quantity related to vortex, different from lambda2, that is $q = sgn(u)\sqrt{\overline{u^2} + \overline{w^2}}$, and can deal with the semi-channel. This process is used as an additional check to ensure the correct inclusion of the body forces in the main code.

A.3.3 How to compute the statistics

The statistics are obtained by analysing both the `Runtimedata` and averaging multiple `Field*.fld` files.

By averaging the field files, it is possible to compute the average velocity profiles, rms velocity profiles, Reynolds stresses, linear PSD, planar PSD, linear correlations, planar correlations and planar dissipation. The code used for the purpose is the `post.cpl` script, that has been modified for the semi-channel.

The friction coefficient, averaged bulk velocity, averaged friction velocity, exact Reynolds number and error bars related to each variable are computed by the code `meanandvar.cpl` that reads and processes the `Runtimedata` file that contains the full story of the simulations. The initial transitory is avoided by

skipping a certain amount of lines and keeping only the rest. This last script is left untouched and did not required any modification.

A.3.4 Error bars for DR values

Each one of the DNS simulations in the present work aim to determine the DR value of a certain flow condition. Since most of them are based on Re_τ, it is convenient to determine the friction coefficient C_f as displayed in section 2.2.4, dependent on U_b and u_τ:

$$C_f = \frac{\tau_w}{\frac{1}{2}\rho U_b^2} = 2\left(\frac{u_\tau}{U_b}\right)^2 \tag{A.6}$$

U_b and u_τ are computed as the spatial average in the computational domain; the final value of C_f is obtained as the temporal average of the spatially averaged values computed at each time-step. The dimension of the domain and the time interval of the simulation could introduce some fluctuations over averaged statistics.

The error estimation strategy proposed allows to give the result with his confidence interval. If one suppose to deal with a continuous ergodic random signal $x(t)$, it is possible to define the autocorrelation function $\rho(\tau)$ can be defined as:

$$\rho(\tau) = \frac{C}{\sigma_x^2} \tag{A.7}$$

where C is the autocorrelation over a finite period of sampling time T and σ_x^2 is the variance of the signal.

The variance of the sample mean $\overline{x}$ of the signal is then computed, as reported in [36], as:

$$\sigma_{\overline{x}}^2 = \frac{2\sigma_x^2}{T}\mathcal{T} \tag{A.8}$$

with $\mathcal{T} = \int_0^T \rho(\tau)d\tau$.

The central limit theorem states that $\overline{x}$ is described by a Gaussian PDF; as a consequence, it is possible to determine an interval where the mean of the signal μ lies with a certain confidence level:

$$\overline{x} - \gamma\sigma_{\overline{x}} \leq \mu \leq \overline{x} + \gamma\sigma_{\overline{x}} \tag{A.9}$$

where γ is confidence interval of a normalized Gaussian PDF.

A.3.4.1 Error propagation by RSS

The uncertainty on DR value comes straightforward using the RSS; recalling the definition of DR from section 2.2.4:

$$R = \frac{C_{f,0} - C_f}{C_{f,0}} = 1 - \frac{C_f}{C_{f,0}} \tag{A.10}$$

then, it is required to obtain σ_R^2 by applying RSS definition:

$$\sigma_R^2 = \left(\frac{\partial R}{\partial C_{f,0}}\right)^2 \sigma_{C_{f,0}}^2 + \left(\frac{\partial R}{\partial C_f}\right)^2 \sigma_{C_f}^2 \tag{A.11}$$

Exploiting the partial derivatives:

$$\frac{\partial R}{\partial C_{f,0}} = \frac{C_f}{{C_{f,0}}^2} \qquad \frac{\partial R}{\partial C_f} = -\frac{1}{C_{f,0}} \tag{A.12}$$

As stated before for the signal $x(t)$, the central limit theorem allows to estimate a confidence interval for DR, the expected value of R lies in:

$$R - \gamma\sigma_R \leq \overline{R} \leq R + \gamma\sigma_R \tag{A.13}$$

References

Bibliography

[4] N. Benard, M. Caron, and E. Moreau. "Evaluation of the time-resolved EHD force produced by a plasma actuator by particle image velocimetry - a parametric study". In: *Journal of Physics Conference Series* 646 (2015).

[5] T. Brauner, S. Laizet, et al. "Modelling of Dielectric Barrier Discharge Plasma Actuators for Direct Numerical Simulations". In: *American Institute of Aeronautics and Astronautics 8th AIAA Flow Control Conference - Washington, D.C.* ().

[6] H. Choi, P. Moin, and J. Kim. "Active turbulence control for drag reduction in wall-bounded flows". In: *Journal of Fluid Mechanics* 262 (1994).

[7] K.-S. Choi, T. Jukes, and R. Whalley. "Turbulent boundary-layer control with plasma actuators". In: *Philosophical Transactions Mathematical Physical & Engineering Sciences* 369 (2011).

[8] P. A. Davidson. *Turbulence : an introduction for scientists and engineers*. 2. Aufl. Oxford University Press, 2015.

[9] R. Erfani, H. Zare-Behtash, et al. "Development of DBD plasma actuators: The double encapsulated electrode". In: *Acta Astronautica* 109 (2015).

[10] H. E. Fiedler. "Coherent structures in turbulent flows". In: *Progress in Aerospace Sciences* 25 (1988).

[11] D. Gatti and M. Quadrio. "Reynolds-number dependence of turbulent skin-friction drag reduction induced by spanwise forcing". In: *Journal of Fluid Mechanics* 802 (2016).

[12] J. Jeong and F. Hussain. "On the identification of a vortex". In: *Journal of Fluid Mechanics* 285 (1995).

[13] J. Jimenez and A. Pinelli. "The autonomous cycle of near-wall turbulence". In: *Journal of Fluid Mechanics* 389 (1999).

[14] N. Kasagi, Y. Hasegawa, and K. Fukagata. "Toward cost-effective Control of Wall Turbulence for Skin Friction Drag Reduction". In: (2009). Ed. by B. Eckhardt.

[15] J. Kim, P. Moin, and R. Moser. "Turbulence statistics in fully developed channel flow at low Reynolds number". In: *Journal of Fluid Mechanics* 177 (1987).

[16] A. N. Kolmogorov. "The Local Structure of Turbulence in Incompressible Viscous Fluid for Very Large Reynolds Numbers". In: *Proceedings Mathematical Physical & Engineering Sciences* ().

[17] C. Lai, H. Fu, et al. “Aerodynamic Drag Reduction and Optimization of MIRA Model Based on Plasma Actuator”. In: 9 (2020).

[18] M. Lee and R. D. Moser. “Direct numerical simulation of turbulent channel flow up to $Re_\tau \approx 5200$”. In: *Journal of Fluid Mechanics* 774 (2015).

[19] M. Lee, R. Ulerich, et al. “Experiences from Leadership Computing in Simulations of Turbulent Fluid Flows”. In: *Computing in Science & Engineering* 16 (2014).

[20] P. Luchini, F. Manzo, and A. Pozzi. “Resistance of a grooved surface to parallel flow and cross-flow”. In: *Journal of Fluid Mechanics Digital Archive* 228 (1991).

[21] P. Luchini and M. Quadrio. “A low-cost parallel implementation of direct numerical simulation of wall turbulence”. In: *Journal of Computational Physics* 211 (2005).

[22] J. L. Lumley. “Drag reduction in turbulent flow by polymer additives”. In: *Journal of Polymer Science: Macromolecular Reviews* 7 (1973).

[23] O. Mahfoze and S. Laizet. “Skin-friction drag reduction in a channel flow with streamwise-aligned plasma actuators”. In: *International Journal of Heat and Fluid Flow* 66 (2017).

[24] S. B. Pope. *Turbulent flows*. 1st ed. Cambridge University Press, 2000.

[25] M. Quadrio and P. Luchini. “Integral space–time scales in turbulent wall flows”. In: *Physics of Fluids* 15 (2003).

[26] M. Quadrio and P. Luchini. “The numerical solution of the incompressible Navier–Stokes equations on a low-cost, dedicated parallel computer.” In: *Rapp. tecn. DIA-SR 04-16* (2004).

[27] M. Quadrio and P. Ricco. “Critical assessment of turbulent drag reduction through spanwise wall oscillations”. In: *Journal of Fluid Mechanics* 521 (2004).

[28] M. Quadrio, P. Ricco, and C. Viotti. “Streamwise-travelling waves of spanwise wall velocity for turbulent drag reduction”. In: *Journal of Fluid Mechanics* 627 (2009).

[29] O. Reynolds. “An Experimental Investigation of the Circumstances Which Determine Whether the Motion of Water Shall Be Direct or Sinuous, and of the Law of Resistance in Parallel Channels.” In: *Proceedings of the Royal Society of London* 35 (1883).

[30] L. F. Richardson. *Weather prediction by numerical process*. Cambridge University Press, 1922.

[31] S. K. Robinson. “Coherent Motions in the Turbulent Boundary Layer”. In: *Annual Review of Fluid Mechanics* 23 (1991).

[32] W. Schoppa and F. Hussain. “Coherent structure generation in near-wall turbulence”. In: *Journal of Fluid Mechanics* 453 (2002).

[33] G. Schrauf. *KATnet: Key Aerodynamic Technologies for Aircraft Performance Improvement*. 2006.

[34] W. Shyy, B. Jayaraman, and A. Andersson. “Modeling of glow discharge-induced fluid dynamics”. In: *Journal of Applied Physics* 92 (2002).

[35] Y. Suzen, G. Huang, and D. Ashpis. "Numerical Simulations of Flow Separation Control in Low-Pressure Turbines Using Plasma Actuators". In: *American Institute of Aeronautics and Astronautics 45th AIAA Aerospace Sciences Meeting and Exhibit - Reno, Nevada - 45th AIAA Aerospace Sciences Meeting and Exhibit* (2007).

[36] C. Tropea, A. Yarin, and J. Foss. *Springer Handbook of Experimental Fluid Mechanics*. 2007.

[37] M. Van Dyke. *An Album of Fluid Motion*. An Album of Fluid Motion. Parabolic Press, 1982.

[38] C. Viotti, M. Quadrio, and P. Luchini. "Streamwise oscillation of spanwise velocity at the wall of a channel for turbulent drag reduction". In: *Physics of Fluids* 21 (2009).

Sitography

[1] URL: `www.top500.org`.

[2] URL: `https://commons.wikimedia.org/w/index.php?curid=343210`.

[3] URL: `https://commons.wikimedia.org/w/index.php?curid=4355112`.